CHARACTERIZATION OF MULTI-PHYSICS AGING EFFECTS ON THE THERMOMECHANICAL VISCOELASTIC RESPONSE OF ULTRA HIGH MOLECULAR WEIGHT POLYETHYLENE FIBER REINFORCED COMPOSITES

by

Jonmichael Andrew Weaver

A dissertation submitted in partial fulfillment
of the requirements for the degree

of

Doctor of Philosophy

in

Mechanical Engineering

MONTANA STATE UNIVERSITY
Bozeman, Montana

May 2024

DEDICATION

In 2014, I suffered a traumatic brain injury (TBI) after a series of sports-related concussions. This TBI left me with loss of vision, memory, and precision of language. Every moment felt like I was stuck in a thick fog. I was disoriented, lost all motivation, and no longer knew who I was. As time went on, I began to grow accustomed to the fog, and dare I say, even began to like the fog. It was somehow easier; I could shift all blame and responsibility. My diagnosis seemed to remove all hope and dreams for the future. But my story does not end here; the way of the fog is through it. Through numerous surgeries and challenging diagnoses, I have learned to find purpose in my pain. This TBI drove me to overcome it. I will not be defined by the limitations and challenges it gave me. Yes, it takes me more effort to learn than it did before, but this adversity has instilled in me a relentless work ethic. This injury has taught me accountability, steering me away from blaming my circumstances. Moreover, my experiences have profoundly shaped my identity. Without these trials, I would not be who I am today. My journey underscores that there is a path forward through the cloudy mist of suffering. The way out is through the fog of pain and loss.

As I reflect on my path out of the fog of physical injuries, my life has shifted from:

1. Ease to difficulty.
2. Comparison to celebration of others' blessings.
3. Momentary to eternal.
4. Control to deference.
5. Being the main character to being a part of the bigger story.

But here I am, a decade later. Broken? Yes, but it is through these cracks and imperfections where the mystery and beauty of God is revealed. Like the gold inlay in a piece of pottery mended through kintsugi, there is more beauty and strength because of the flaws. No pain that is given to Him is wasted. I am walking proof that God can still heal miraculously and redeem the pain you may be in.

The mere fact that I am writing my story here, in this doctoral dissertation, is a testament to the miraculous healing and redemption that God brought into my life. Therefore, I dedicate this dissertation to all those who have had TBI's, may my story inspire you to be resilient through your pain and find the way through the fog of despair and loss.

ACKNOWLEDGEMENTS

I want to acknowledge my advisor, Dr. David Miller for guiding me through this project and taking me on as a graduate student. Thank you to my committee: Dr. Bob Harder for his support in both my academic and life pursuits and for the incredible homegrown food, Dr. Ryan for her assistance in polymers and Dr. Bajwa for his guidance in composites.

Thank you to Dan Samborsky for imparting engineering wisdom and for teaching me how to be better at pretty much everything. Tom Jungst has my unwavering gratitude for his contributions to this project and for his support professionally and personally. Thanks to: Casey Spawn for his personal, professional, and academic support, and for his vision and financial support on this project, Steve Ellis for his mentorship, encouragement, and technical support. Thank you to Dr. Frank Gac and Dr. Rich Mah for imparting their decades of knowledge and expertise from the Armor/Anti-Armor Project. Thank you: Jon Ventura, Stace Lindsay, Dana Gleason, Al Deibert, Jacob DeNeui, Crooked Yard Hops, Map Brewing, Revival Church, the Wiens family, Ryan Phillips, the students in Roberts 421, Graduate Student Ambassadors, and Graduate Leadership Council. Orlando Lopez, Steve Honig, Gil Garduno, and the IAT-2/3 groups. Thank you to Darryl Gardner, Tamra Heberling, Ryan Gilbert, and Debbie Baca for providing a home away from home. Thank you Dr. Mike Foster, Todd Curtis and so many others at GFU who have shaped my worldview and showed me new ways to problem solve. Last, but certainly not least, a huge thanks to my family for the support that words cannot describe.

TABLE OF CONTENTS

TABLE OF CONTENTS – CONTINUED

TABLE OF CONTENTS – CONTINUED

LIST OF TABLES

LIST OF FIGURES

LIST OF FIGURES – CONTINUED

Figure Page

LIST OF FIGURES – CONTINUED

Figure Page

LIST OF FIGURES – CONTINUED

LIST OF FIGURES – CONTINUED

Figure Page

LIST OF FIGURES – CONTINUED

Figure Page

NOMENCLATURE

$\mathbf{A}$	Cross-sectional area
$\mathbf{AD}$	System areal density
$\mathbf{A_p}$	Projectile presented area at impact
$\mathbf{cN}$	centi-newton (1 cN = 1/100 of a newton)
$\mathbf{den}$	(denier) linear density (g/9000m)
$\mathbf{DR}$	Drawing Ratio
$\mathbf{dtex}$	(decitex) linear density (g/10km)
$\mathbf{E}$	Young's modulus (N/m^2)
$\mathbf{E'}$	Storage modulus (N/m^2)
$\mathbf{E''}$	Loss modulus (N/m^2)
$\mathbf{f}$	Function of fiber and projectile type
$\mathbf{F_b}$	Force required to break a fiber
$\mathbf{g}$	grams
γ	Shear strain (dimensionless)
$\gamma_\mathbf{0}$	Maximum shear strain amplitude (dimensionless)
$\mathbf{km}$	kilometer
$\mathbf{m_p}$	Projectile mass
$\mathbf{MW}$	Molecular Weight
$\mathbf{\Omega}$	Dimensionless performance parameter for ballistic protection (m^3/s^3)
ρ	Density (kg/m^3)
σ	Ultimate axial tensile strength (N/m^2)
$\sigma_\mathbf{0}$	Maximum stress amplitude (N/m^2)
$\mathbf{tex}$	Unit of linear density g/km
$\mathbf{t}$	Time (s)
δ	Phase angle (rad)
$[\mathbf{0/90}]_\mathbf{n}$	Cross ply with alternating layers of 0° and 90°, number of layers = n
$\mathbf{U}^*$	The product of fiber specific toughness and strain wave velocity
$\mathbf{V_{50}}$	Velocity at which there is a 50% probability of target penetration (m/s)
$\mathbf{V_f}$	Fiber volume fraction
ε	Fiber elongation at break (dimensionless)
ω	Angular frequency (rad/s)
$\mathbf{W}$	Watts $(kg \cdot m^2)/s^3$

ABSTRACT

Ultra High Molecular Weight Polyethylene (UHMWPE) fiber reinforced composites have a high strength-to-weight ratio and are gaining attention as a material of choice for specialized applications subjected to extreme environmental conditions. Users value the water-repellent, lightweight, and flexible nature of the material for applications where weight is crucial. Marine, aerospace, and alternative energy sectors are exploring UHMWPE fiber reinforced composites for specialized applications in demanding environments where strength, flexibility, and weight efficiency are important design criteria. The viscoelastic and hydrophobic nature of UHMWPE makes it an attractive replacement for Kevlar® in ballistics protection shields and other industrial applications, providing similar performance while achieving upwards of 40% reduction in weight. However, the durability of UHMWPE composites under real-world aging conditions remains insufficiently examined.

This research investigates how the viscoelastic properties of UHMWPE fiber reinforced composites, created through various manufacturing techniques, are altered after exposure to harsh conditions including immersion in water, temperature variations, humidity, and UV exposure. Additionally, the composites were irradiated with: X-rays, γ-rays, and neutrons. After exposure to adverse environments, the thermomechanical viscoelastic response was characterized through Dynamic Mechanical Analysis (DMA). Surface morphology was evaluated using a field emission scanning electron microscope. DMA revealed an increase in the storage modulus with aging; however, elevated temperature creep tests showed that UV and hygrothermal aging had a higher creep compliance and decreased the ability of the composite to recover strain after unloading. Both single layer and pressed UHMWPE panels showed an increase in weight after submersion in water. Distilled water resulted in a faster rate of hydrolysis in the matrix than did salt water. The UV, γ-ray, and neutron environments caused the composites to become brittle and yellow through chain scission and crosslinking, whereas the X-ray radiation exposure did not cause a measurable effect. Analysis on the surface of these composites after aging suggested the matrix protects these fibers from damage in harsh environments. Synthetic rubber matrix materials aged at a faster rate than the polyurethane rubber matrix materials. Increasing the strain rate showed an increase in moduli response during tensile DMA. These results quantify the limitations and strengths of this material for future models to accurately predict the lifespan and expand the application of this performance material in extreme environments to ensure safety for applications ranging from extreme sports to aerospace.

1

INTRODUCTION

This work attempts to bridge the gap between mechanical properties and ballistic protection performance through the characterization of ultra high molecular weight polyethylene (UHMWPE) fiber reinforced composites after multi-physics aging in simulated extreme environments.The data presented herein will contribute to the understanding of how UHMWPE fiber reinforced composites respond viscoelastically to thermomechanical loading and how various environments alter that response.

Chapter 2 provides insights into the polymer science and aging mechanisms these composites experience, as well as a brief narrative on the history of production and the dynamic manufacturing industry. Some common applications and manufactures of this UHMWPE fiber reinforced composites are described in Chapter 2 as well. Chapter 3 details the experimental methods used to age and characterize the UHMWPE composites after aging, with additional learning opportunities for sample preparation. Chapter 4 reports the strength of unaged single layer UHMWPE fiber reinforced composites through tensile testing. Chapter 5 shows how UHMWPE fiber reinforced composites respond to water submersion. Chapter 6 details how the UV aging, hygrothermal, and dry temperature cycling alters the mechanical response of UHMWPE composites. Chapter 7 shows the viscoelastic response of UHMWPE fiber reinforced composites after aging in ionizing radiation environments. Chapter 8 reports a brief summary and highlights a few key takeaways of this study. Chapter 9 details the areas for more scientific exploration. Finally, Appendix A is the MIL-STD-810H fungal test results conducted by an outside testing service NTS.

2

BACKGROUND

Polymer Science

Polyethylene is formed from the base hydrocarbon monomer, ethylene, and has an asymptotic molecular weight melting point near 145°C [4]. The chemical monomer structure for the repeating unit of polyethylene is $(-CH_2-CH_2-)_n$.

The durable nature of polyethylene stems from the ability of this polymer to form long symmetric and densely packed molecular chains. These chains are capable of connecting multiple sections of the polymer within a lamellar crystalline site via chain folding [4]. A lamellae is an area where chains are folded together into an ordered higher density region, which can be unfolded into a longer continuous chain through a drawing process.

This shift from the shorter polymer chains, such as in a wax, to the longer chains in the polyethylene also changes the primary bonding between chains from the weaker van der Waals forces to the stronger covalent bonding as shown in Figure 2.1 [4, 5]. Polyethylene is dual phase at room temperature, crystalline and amorphous. The crystalline phase gives it structure and rigidity, where the amorphous phase which makes it pliable. Polyethylene's pliability or compliance increases with temperature [4].

Polyethylene is classified as a semi-crystalline polymer at room temperature, and has a directionality in mechanical strength corresponding to how the polymer chains are formed and orientated [4]. Figure 2.1 contrasts the morphology of paraffin wax and polyethylene, depicting the chain folding, amorphous entanglements, and ordered crystalline lamellae.

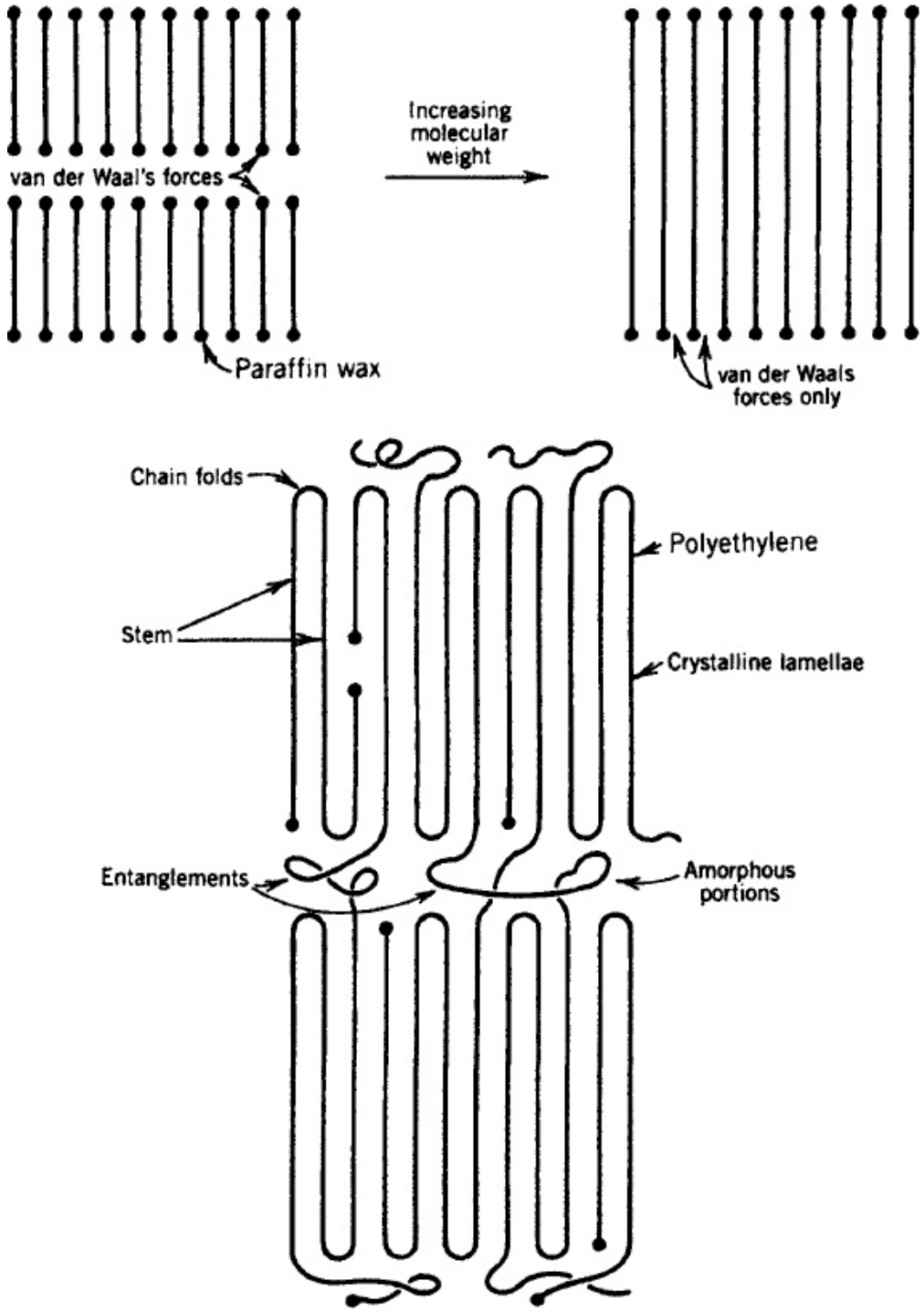

Figure 2.1: Chain structure of paraffin wax compared to polyethylene [4].

As polyethylene chains lengthen, the molecular weight (MW) increases resulting in a higher modulus and tensile strength [4]. Lengthening the polymer chains is commonly done through stretching the polymer along sets of rollers in a process called drawing. The stretching of the polymer can be inhibited by entanglements between the individual chains; the more entanglements, the more knots preventing them from stretching out to the normal length as shown in Figure 2.2.

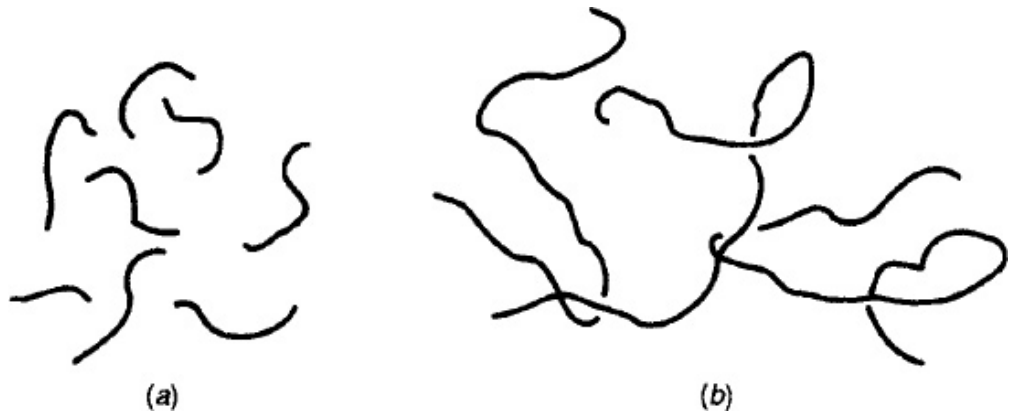

Figure 2.2: Polymer chain with (a) no entanglements (b) random coiling of amorphous chains causing entanglements [4].

Solvents are used in the gel-spinning process to increase the viscosity of chains during polymerization which decreases the number of entanglements to allow for a higher drawing ratio (DR). The natural DR of polyethylene is 5:1 due to the natural entanglements, preventing the chains from further orientation [5]. Just like Christmas lights need to be untangled before stretching it out, the polymer has the potential to be lubricated using a solvent such as decalin or a paraffin oil/wax, to increase the ability for those entanglements to untangle in conjunction with drawing. By the addition of the solvent with the stretching process, the drawing ratio can increase up to 240:1 [5, 12]. This high drawing ratio can increase the longitudinal modulus of polyethylene from 1 GPa to 172 GPa. This increase in strength and modulus causes a corresponding decrease in ductility and creates weaker

transverse properties. The strain at failure for UHMWPE decreases as shown in Table 2.1. Tensile strength and modulus increase with drawing ratio, however there appears to be an asymptotic material limit around a $DR \geq 200$ [12, 13].

Table 2.1: Longitudinal Tensile Properties of Various Polymers. Adapted from [1].

Polymer	**Modulus (GPa)**	**Strength (GPa)**	**Strain (%)**	**T_f (°C)**
Polystyrene	4	0.08	2	100, T_g
Polyethylene (PE)	1	0.05	50	140
Drawn PE	172	3.5	5	149
Rayon	3	0.3	20	180 decomp.
Polyamide	3.8	0.8	25	250
Poly(1,4-benzamide) (Kevlar®)	100	3.0	6	500 decomp.

Molecular weights are distributed throughout the polymer, with the lower molecular weight chains acting as a plasticizer along with the amorphous regions, which give the polymer compliance. The higher molecular weights, together with the crystalline phases contribute to the strength and modulus of the polymer [4]. The polyethylene has a distribution of properties throughout a given sample which can be a source of variability in mechanical testing. During this research, this error is mitigated by using a large number of samples during testing involving a random sampling of areas from the unidirectional composite fabric rolls.

Due to the dense packing of the long molecular chains, the structure of the polyethylene

fibers are ideal for high strength-to-weight ratios and for dissipating strain energy at high strain rates. The fibers also have a high toughness, as defined by the area under the tensile stress-strain curve. Figure 2.3 compares the tensile stress-strain curves for several common fibers used in composites, depicting a higher toughness for an UHMWPE fiber compared to aramids, which have be the gold standard for ballistic protection, due to their higher strength and higher elongations to failure.

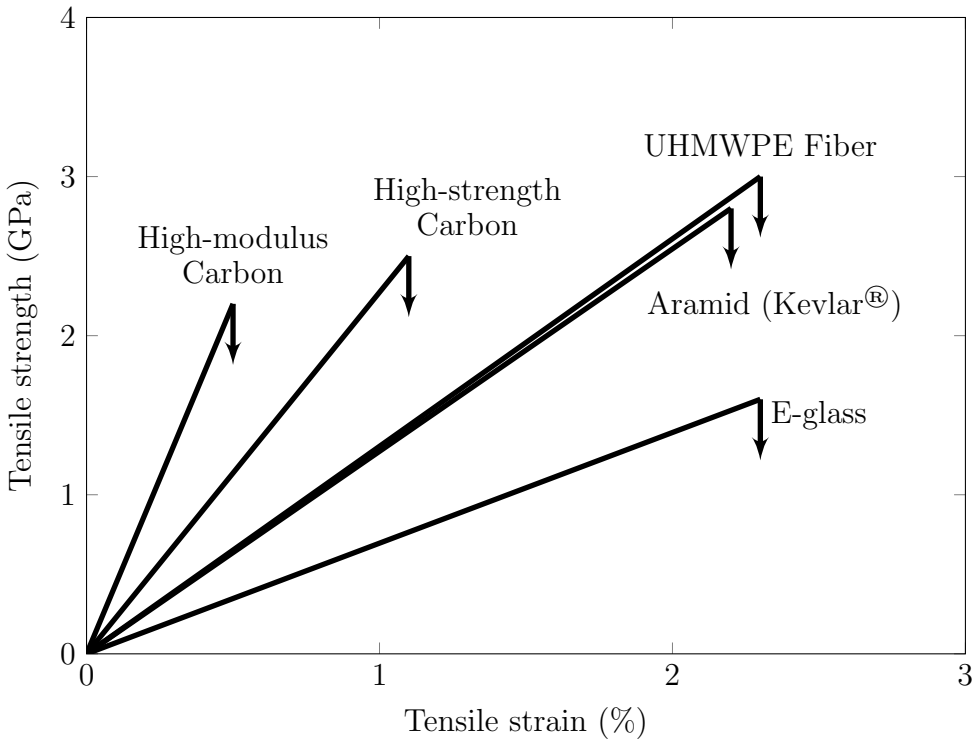

Figure 2.3: Relationship between tensile strain and tensile strength for various fiber materials. Adapted from [5].

Manufacturing and Synthesis

Ultra High Molecular Weight Polyethylene (UHMWPE) fibers were invented by Dutch State Mines (DSM) in the 1960's [6, 14]. The fibers became commercially available in the 1970's and were renowned for their high strength to weight ratio [6, 14]. Due to the dense

packing of the long molecular chains, this form of polyethylene is designated Ultra High Molecular Weight Polyethylene, as it has a molecular weight greater than 10^6 g/mole [5].

UHMWPE is synthesized in powder form before molding into a final shape or billet for machining. This dissertation only covers how UHMWPE fibers and films are made through two different processes: gel-spinning and powder compaction [7, 12, 13, 15]. These fibers are then combined with a thermoplastic or thermoset matrix to make a layer of composite material. This advancement in the composite form of UHMWPE has spurred the development of stronger UHMWPE fibers through refinements in the gel-spinning process.

Gel-Spinning

The process is broken up into four steps: (1) dissolution using a solvent and elevated temperatures to reduce chain entanglements (2) extrusion and spinning into a cooling bath to crystallize the disentangled polymer chains (3) solvent removal using an extractant and/or drying to stabilize the polymer (4) drawing/stretching to align the chains [6, 13]. This process is summarized in Figure 2.4.

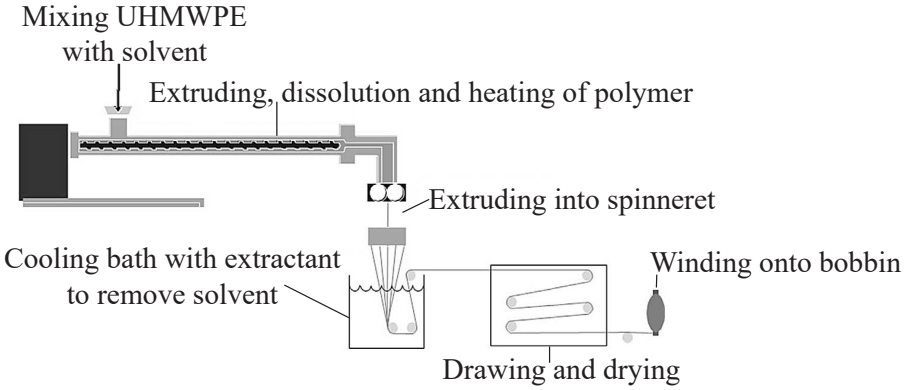

Figure 2.4: Gel-spinning process. Adapted from [6].

To achieve gel-spinning, 5%-10% polyethylene is dissolved into a solvent with an antioxidant. This mixture is held near the melting temperature of polyethylene around 145°C allowing the polymer chains to relax and untangle [5, 13]. After annealing in an

inert environment, the mixture is slightly cooled just under the melting temperature (135°C), where it forms a gel as it is extruded onto the spinneret [13]. At this stage, the gel-spun fibers are submerged in a cooling bath (120°C) of either an alkaline or fluorocarbon to crystallize the polymer and remove the remaining solvent and antioxidant [5, 13]. The polyethylene fibers are then drawn and dried to align the polymer chains before being wound onto a bobbin. These diameter of these UHMWPE fibers have a range throughout manufacturing, but the average is approximately 12 μm [3].

The fiber-matrix interface can be improved through cold plasma etching of the surface [5]. The gel-spinning process produces highly anisotropic fibers, with the majority of the strength in the axial direction [16]. These fibers are often used in composites for ballistic protection applications.

Powder Compaction

A more economical and environmentally friendly method of manufacturing high strength UHMWPE compared to gel-spinning is by the process of filming. This continuous filming process goes by many names: powder compaction, ultra-drawn compression molding, or solid state processing (SSP) [17]. This manufacturing method does not require harsh solvents for production, which eliminates a great deal of hazardous waste. The SSP method encompasses these three primary steps: (1) compressing the initially highly dispersed loose (UHMWPE) nascent Reactor Powder (RP) to create a compacted material puck with adequate density; (2) using heat to transform the compacted material into a monolithic form with sufficient strength for further processing; (3) performing additional chain orientation through stretching the monolithic material to produce high tensile strength polyethylene [17].

This manufacturing concept was developed by Professor T. Kanamoto at Tokyo University in 1987. Nippon Oil (Japan) patented this process in 1989, followed by patents

from Integrated Textile Systems (USA) in 1999, and Teijin Aramid (Netherlands) in 2010 leading to commercialization and large scale production [7].

This powder compaction/SSP method is used to create high tensile strength UHMWPE films/tapes which can replace the gel-spun fibers in many applications. The SSP films or tapes can be slit into thinner strips and then wound or braided into ropes, slings, nets etc [3, 18].

This form of UHMWPE has all the advantages of the high strength-to-weight gel-spun fiber products without the weak fiber-matrix interface or issues with fiber kinking or breaking [19].

The SSP process, similar to gel-spinning, requires a certain amount of tradecraft and science to produce a quality product, which are explored further in [7, 17, 19–26]. This method is used to produce material which has been used in a variety of industries such as aquaculture nets, tethers, stratospheric air ships, radomes, and ballistic shields.

Development and improvements of UHMWPE manufacturing processes has led to increasing the strength and modulus over the decades as shown in Figure 2.5.

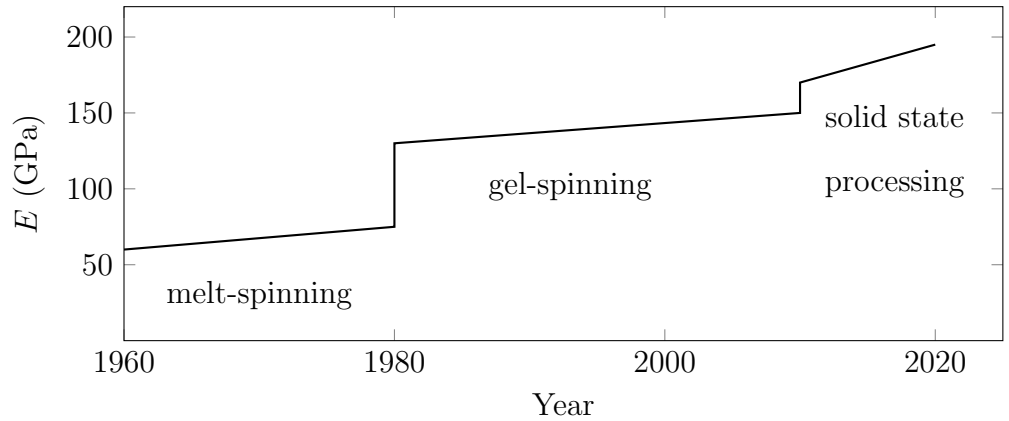

Figure 2.5: Longitudinal Young's Modulus (E) increasing over the decades due to manufacturing improvements. Reproduced from [7].

Main UHMWPE Manufactures

UHMWPE manufacturing has shifted over the decades. The most recent acquisition of technology brought two of the larger manufactures of UHMWPE from the Netherlands, DSM and Teijin's products to the USA.

DSM

The UHMWPE fibers produced by DSM are trademarked Dyneema®, which comes from the Greek words "dyne" meaning strong or powerful and "ína" for fiber, translating to "Strong Fiber" [27]. The tensile strength of these Dyneema® fibers can reach 4.1 GPa, with a tensile modulus of 155 GPa, according to DSM datasheets [28]. Additionally, the UHMWPE fibers are known to not absorb water, exhibit low friction, be visually opaque, and act as an electrical insulator [28]. These UHMWPE fibers are reported to have a sonic velocity that can reach up to 12000 m/s in the axial direction [28].

In more recent years, these fibers have been combined with a matrix to form a lightweight and waterproof fabric adopted by endurance athletes for jackets, tents, and other applications in which lightweight and watertight are desirable traits. The Dyneema® Project highlights a few of these collaborations with other brands to showcase the advantages of using UHMWPE fabrics [29], especially in extreme sports. Another large market segment for Dyneema® is their protective materials applications, in which the unidirectional (UD) armor arrived on shelves in 1993, and has been dominating a large market segment since [30].

Avient Corporation

In April of 2022, Avient Corporation announced that they bought the protective materials division from DSM for $1.45 billion [31]. Avient Corporation is a US based materials conglomerate. This includes the technology for the Dyneema® UHMWPE fibers.

The author conducted interviews with representatives of Avient Corporation at trade shows and conferences in the fall of 2022 and early 2023. They had no information about when Avient would begin producing and selling Dyneema® in the USA again. On January 16, 2024, Avient launched the new Dyneema website, claiming the manufacturing plants are still located in Arizona, North Carolina, and the Netherlands just as they were under DSM ownership [27, 32].

Teijin

In 2010, Teijin Aramid in the Netherlands filed a patent for continuous processing of UHMWPE tapes from a powder [7]. During a phone interview, the author conducted with an engineer at Teijin Aramid, the engineer stated that Teijin had discontinued Endumax® production in late 2022 [3]. The reason given was that Teijin was trying to increase their Environmental, Society, and Governance (ESG) Score by moving their manufacturing portfolio to completely recyclable materials over the next decade. Endumax® was one of the earlier products to be discontinued because of a downturn in demand from two market areas. In the aquaculture, or oceanic fish farming industry, where the nets are made from UHMWPE, Teijin was being undercut by production of lower quality material made in China. Manufactures in Asia were able to make a cheaper, albeit inferior version of the nets, but at an attractive cost point to the fishing industry, removing this large market segment from Teijin [3]. The other large market of protective materials was unsteady due to the supply chain crisis from the COVID-19 lockdowns, which led Teijin to cease production at that time [3]. Endumax® has a few smaller markets as a material in automotive manufacturing, radomes, speak cone materials [33], and air shipping containers [3]. However, in July 2023, Barrday announced the purchase of Endumax® and plans to start production in 2025 [34].

Other Overseas Manufacturing

The gel-spinning technology was replicated by Yimin Wang at Donghua University, which was formerly known as China Textile University [15]. In a collaboration with Guo Zixian, Wang and a fiber equipment manufacturer Jiangsu Shenshe Technology Development Company copied the gel-spinning process created by Honeywell using paraffin oil as a solvent for the UHMWPE. The fiber rests in this paraffin oil after spinning for 1-2 days in a porous container for the solvent to 'sweat out' before drawing the fiber [15, 35]. As of writing this, the UHMWPE fibers produced in China have a tensile strength and modulus that are inferior compared to USA-based manufacturing, most likely due to the impure UHMWPE feed stock used. However, Sinopec, another fiber manufacturer in China, uses the same solvent as Dyneema®, decalin, but dry-spin rather than gel-spin the fibers in a factory located in Yizheng [15, 36], suggesting that they might reach or exceed material properties manufactured in the West.

Recently, the powder compaction/(SSP) has also been replicated and is in production throughout China. The material quality may increase in the coming years as the UHMWPE industry in China has been organizing symposiums and annual meetings as early as September of 2022. They report focused attention on improving the UHMWPE supply chain to meet both military and civilian needs [35]. The "Ultra High Molecular Weight Polyethylene Fiber Branch of China Chemical Fiber Industry Association" and "High-Quality Development Seminar" annual meetings are attended by the president of the Materials Science and Engineering School at Donghua University, the president of the China Chemical Fiber Association, Vice Mayor of the Yancheng City, and other entrepreneurs, experts, scholars in the UHMWPE industry [35]. Companies like Shenhe Technology Development Co/Holy Crane sell UHMWPE processing and manufacturing lines, and approximately 40 other Chinese companies have or are currently producing material, driving the commodity price of UHMWPE down to $10 USD/kg [15, 37].

Barrday

The headquarters of Barrday is located in Ontario, Canada and has another office and warehouses in the Netherlands. But, the manufacturing and R&D facilities are located in the USA. They focus on creating composite materials to support the aerospace and defense industry. Barrday is an industry leader in research and development (R&D) into protective materials. Barrday claims to create their own composite layups with UHMWPE fibers and new matrix combinations involving thermoplastics, thermosets like phenolics and neoprenes, and UD tapes. In late 2023, Barrday acquired the Endumax® brand from Teijin [34]. They plan to move the manufacturing line to North Carolina and predict that production will occur in 2025.

Honeywell

Honeywell and Allied Signal merged in 1999, and trademark their UHMWPE fiber Spectra® [38]. This UHMWPE fiber is made from the gel-spinning process but uses a paraffin oil as the solvent. They continue to be one of the leaders for defense contracts. Despite multiple attempts to acquire information on their fiber strength and matrix properties/constituent parts, they will not disclose any information as most of their material distribution is defense related.

DuPont

DuPont manufactures a UHMWPE tape from powder compaction called Tensylon®. This technology was started by Integrated Textile Systems in the 1990's which sold to BAE Systems in 2000, and then merged with Armor Holdings in 2007 [7, 39]. In 2012, DuPont purchased BAE Systems/Armor Holdings and has been producing Tensylon® exclusively for defense customers [40].

Table 2.2: Advertised Axial Material Properties of UHMWPE Composites and Tapes [2, 3].

Material Type	**Modulus (GPa)**	**Strength (GPa)**	**Areal Density (g/m^2)**	**Ply Thickness (µm)**	**Strain (%)**	**Matrix**
Dyneema® HB-210	60	14*	136	133	2.82	PUR
Dyneema® HB-212	60	14*	136	120	3.03	Kraton® Rubber
Honeywell Spectra Shield® 5241	124	2-3	167	∼180	3-4	PUR
Teijin Endumax® XF23	182	2.1†	198	60	1.7	PE

*converted to a stress based on 80mm wide strip. †converted to a stress based on 2mm wide strip.

UHMWPE Uses

UHMWPE fibers and tapes are used in a variety of industries looking to elevate performance. A common commercial use is creating cut resistant gloves for the meat packing industry [41]. It has also found many uses in marine applications such as lightweight creep resistant sails for racing boats, tethers and mooring lines for commercial shipping, and as ropes for hoisting the large offshore wind energy turbine blades. Due to UHMWPE's resistance to salt water corrosion and high tensile strength, this material is desirable for fishing and aquaculture applications. It has also proven useful in nuclear power plants as a mesh filter to keep the intake for cooling water clean [10].

Recreation

Due to the lightweight, high strength, and waterproof nature of UHMWPE, this material has found a niche within performance recreation. Many ultralight gear companies have made use of UHMWPE for tents, shoes, outer layer apparel, and climbing slings [27, 29, 42]. A notable extreme use case was in 2016 when the world record was set for the highest skydive without a parachute into a net made from UHMWPE [43]. This safety net made use of the strength and dampening ability in UHMWPE to withstand the impact of a man jumping from 25,000 ft and safely catch him.

Radomes

For critical applications, such as defense, these antennas and communication electronics require protection from kinetic attacks. UHMWPE is a choice performance material for allowing the signal in/out, while providing ballistic protection for the electronics inside [44]. The material UHMWPE has a low dielectric constant and loss tangent properties, allowing microwave, Ku, and Ka band transmission at high efficiencies compared to other ballistic protection materials [3, 5, 44, 45].

Neutron Moderator

Bulk UHMWPE material is commonly used in implantable medical devices due to the material's bio-compatibility and low friction properties [46]. As medical implants need to be sterilized prior to being used in an operation, gamma radiation is the preferred method over an autoclave, due to the low melting point of UHMWPE. This has led to some studies being performed on the aging effects that gamma radiation has on UHMWPE. Open source studies focus on gamma radiation aging as the implant needs to be sterilized before the operation.

Current methods of radiation shielding are heavy and inflexible. Materials that can absorb high energy particles typically need to be high-Z elements, or have large masses such as concrete walls or oil filled vessels. Some methods have potential health risks such as lead-lined curtains. Interest has increased over UHMWPE as a potential lightweight flexible barrier for ionizing radiation. In theory, neutron shielding/moderating is most effective when using elements with a lower atomic number. For example, boron carbide (B_4C) control rods in nuclear reactor cores are used to absorb neutrons. Materials rich in hydrogen atoms are also used to moderate or thermalize neutrons [47]. Through the addition of other materials with a high neutron absorption cross-section, these hydrogen-rich materials can remain lightweight while increasing moderation and absorption. Bulk UHMWPE with 5 mass% molybdenum trioxide particles (MoO_3) has shown the ability to absorb up to 25% of a 241Am/Be fast neutron source doses [48]. Other studies have shown that doping UHMWPE with samarium oxide (Sm_2O_3), boron oxide (B_2O_3), and boron nitride (BN) can also be effective in absorbing both neutron and gamma radiation [47]. These additives can be included into future developments to increase the moderation ability of the composite.

Since 2019, international interest has grown around the use of UHMWPE for dual purpose radiation and ballistic shielding. Particularly, one university in Algeria has published and presented on this topic multiple times. Two individuals are at the center of this research, Mehdi Derradji, and Oussama Mehelli, who are affiliated with both the Ecole Militaire

Polytechnique University and the Polytechnic School of Algiers. Their research began by looking at the radiation shielding properties of carbon glass and basalt fibers, before moving onto Kevlar® and UHMWPE fiber reinforced composites [49–52]. However, why is Algeria interested in this material for defense applications now? The first is because of the rising tensions on their border with Morocco. Year over year, Morocco and Algeria spend the most on arms compared to the rest of the continent, and have been locked into an arms race for the better part of the past decade [53, 54].

In July of 2023, China announced a $36 billion USD investment into Algeria for manufacturing, increased security and sovereignty, further 'Belt and Road' construction, and mining/energy exports. President Xi said in a press statement that both sides will cooperate in "aerospace, infrastructure, nuclear energy, and petrochemicals" [55, 56]. As Algeria is interested in join BRICS group (Brazil, Russia, India, China, and South Africa), the scientific and knowledge economy between the two countries is also increasing. As of August 2023, Algeria was not admitted.

High Altitude Wind Energy

Basic fluid mechanics principles say that the further away from the boundary layer, the higher the velocity of a fluid. The same holds true for the earth's atmosphere [57]. Airborne Wind Energy (AWE) is the generation of power by devices either tethered to the ground or freely flying compared to traditional turbines which are set on top of a tower either on land or offshore. This prototype technology seeks to increase the consistency and decrease the cost of wind power by accessing the jet streams at higher altitudes where the potential wind energy is greater and more reliable. Two categories of AWE exist: ground-based and airborne power generation. The first is where mechanical energy is transferred from the air to the ground where it is then converted into electricity. The second is where generators in the air produce the electricity and transmit the power to the ground through a tether [58].

The mechanical energy transmission concept is prototyped by companies such as KiteGen where the concept arose from looking at increasing the efficiency of wind turbines, where the outer third of the blades generates more than half the power [59]. KiteGen's design takes that same principle and harnesses the high velocity at the tip by replacing the blades with a kite or sail made from UHMWPE. This reduction in weight eliminates the need for a large tower to support the weight of long blades which are now in excess of 80 m. The KiteGen design takes two kites tethered to a drum where both kites travel in a figure eight shaped path. These two kites work in concert with each other; one is in drag mode while the other is in lift mode, creating continuous movement and winding the drum in one direction before reversing and winding the drum in the opposite direction, generating power through the movement of the drum. This two-kite design is modular and can be combined into a carousel-type system that can generate 100 MW in an area of approximately 0.8 km^2 [60]. Another design by a German company, X-Wind, could place these tethers onto a linear track and pull vehicles which have onboard alternators [61]. Creating these kites from UHMWPE fiber reinforced composites is advantageous to the designer because of the material's lack of moisture absorption, performance in low temperature experienced in upper altitudes, and great abrasion resistance from particulate traveling through the atmosphere. The current aramid-based tethers will benefit by upgrading to UHMWPE tethers, increasing the lifespan and durability of the cords through strength improvements in wet environments and reduction in the creep under prolonged tensions [62].

This same process can be applied to create airborne power generation. UHMWPE inflatables are a proven technology that can transport AWE turbines to the operating altitude, making it more lightweight and durable than typical 'weather balloons'. Additionally, the UHMWPE tethers can be used without risk of creep or shrinkage in cold temperatures as polyethylene has a negative Coefficient of Thermal Expansion (CTE), meaning it expands as the temperature decreases. AWE potentially has a lower cost per unit of usable power

compared to traditional renewable energy sources, making this a candidate for large-scale deployment as an energy source with a lower capital barrier to entry [59]. A potential niche market for AWE is in areas recently affected by natural disasters, where other power generation sources have become damaged. AWE may be deployed to quickly restore power due to the lightweight and small-scale nature of these systems.

Advancement in the understanding of how UHMWPE ages in harsh environmental conditions will benefit the renewable energy sector through the implementation of UHMWPE for lightweight and durable kites, tethers, and balloons to help meet the growing energy demands.

Tethers

Additionally, high-altitude kites also have the potential to realize the concept of space tethers and elevators, and provide a way to get objects such as satellites into space while reducing the use of fossil fuels. UHMWPE fiber reinforced composites have been shown to function as tethers in space. An article by Michel van Pelt claims that the tether expanded once it got exposed to sunlight and caused a disruption in the orientation due to a slackening in the line. This does not seem logical as UHMWPE fibers have a negative CTE, meaning they would shrink in the sunlight and not expand and slacken as the study claimed [63, 64]. This study needs to be investigated and repeated to understand what phenomena was being observed. Bulk UHMWPE can also be used as a performance material in space flight systems [46]. In addition to high-strength tethers, UHMWPE composites can be used as high-altitude sails to keep the tether system aloft during operation. Characterizing how this material responds to radiation and the extreme environments experienced at high altitudes will be a crucial step in determining material lifespan and viability in the upper regions of the atmosphere and space. Other projects have used UHMWPE composites to make high altitude balloons as seen in the Stratos Project by Red Bull that took Felix Baumgartner on his

famous skydiving jump from space in 2012 [65].

Stratospheric Balloons and Airships

Polyethylene films have been used for stratospheric balloons for several decades, mostly in the national security industry [66]. In recent years, there has been a renewed focus on high altitude balloons in the commercial sphere, beginning with Project Loon, by Google X. The goal of this Google X venture, was to provide internet to the globe through constellations of stratospheric balloons. Project Loon was discontinued in 2021 [67]. Shortly after this project ended, much of the technology was made available in open source. There was a race in industry to secure the talent and technology developed through Project Loon. These high altitude balloons are made from thin polyethylene films and filled with helium or hydrogen gas and launched into the stratosphere. Due to the negative CTE and high UV and radiation tolerance, these balloons can maintain a uniform altitude for months at a time. As in the skies over the USA and in the news during March 2023, China used UHMWPE balloons to provide surveillance and reconnaissance over long distances [68].

Aerostar, a USA based defense contractor has several patents involving the construction of of these airships using UHMWPE [69–71]. Aerostar was acquired by a defense conglomerate, TCOM holdings, in 2022 [72]. TCOM manufactures airships in more complex blimp shapes and uses UHMWPE as tethers and as reinforcements.

Battery Membrane

A recent development in the safety of batteries is using UHMWPE films as a membrane in rechargeable batteries [73, 74]. This material has an advantage over polypropylene, as UHMWPE has a higher toughness, lower shutdown temperature, and lower glass transition temperature, all of which improve the low temperature performance of batteries [74].

Ballistic Shields

Woven UHMWPE is not often used for ballistic protection due to the lower performance in stopping power. This decrease in ballistic protection performance is potentially attributed to the low coefficient of friction between fibers, allowing the fibers to move laterally and not engage the projectile to absorb and dissipate the energy as the UHMWPE fibers do when confined in a matrix [6, 75–77].

UHMWPE fiber reinforced composites are divided into two main classes by manufactures: soft and hard ballistics. Soft ballistics are manufactured by taking a unidirectional crossply, [0/90], and coating both sides with a thin flexible polymer film such as polyurethane, creating a semi-preg UD fabric [6]. Hard ballistics use a layup of $[0/90]_2$, without the extra laminate every other layer, resulting in these sheets being less flexible than the soft ballistics. Both composite plys are referred to as unidirectional (UD) sheets throughout the ballistics protection industry, despite being bi-directional, and have a fiber volume fraction around $V_f = 80\%$ [6]. Figure 2.6 depicts the layup structure for a unidirectional sheet of (a) soft ballistics fabric and (b) hard ballistics fabric.

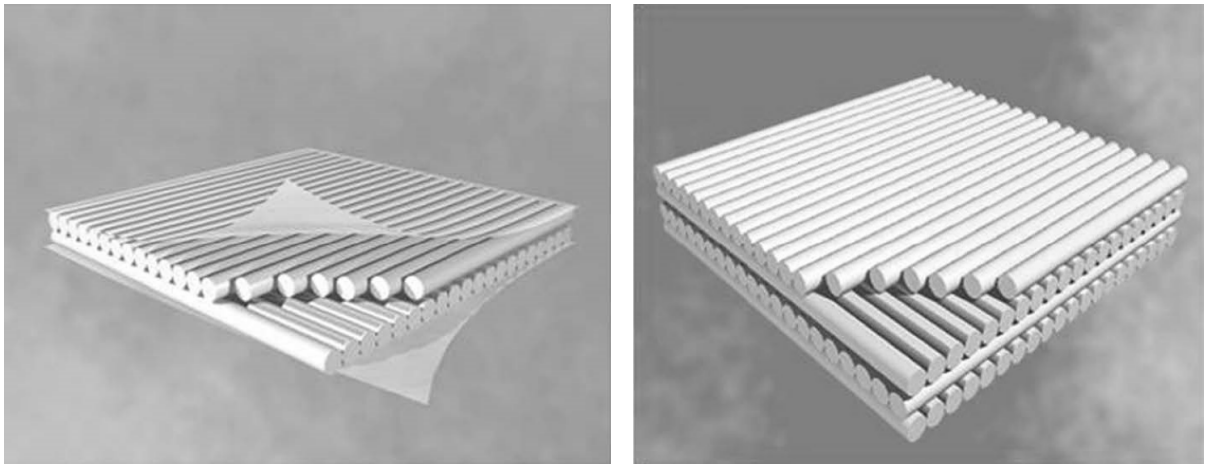

Figure 2.6: Comparison of pre-preg sheets layup for (a) soft ballistics [0/90] and (b) hard ballistics $[0/90]_2$ layups [6].

These UD sheets are then layered up to a given thickness to handle the required threat level and then hot pressed to form panels. These panels can be cut out to form personal protective equipment like helmets, vests, or vehicle armor. However, for larger threats or armor piercing rounds, multi-layer armor is required. UHMWPE is currently used in the outer layer of space suits and is undergoing studies as a hyper-velocity impact shield for space craft called a Whipple Shield [78, 79].

Figure 2.7 depicts a simplified multi-layer polymeric based armor. The first layer designed to break up the projectile, the second layer is the polymer to absorb and dissipate energy from the impact, and the third layer is to catch any spall or fragmentation that may have penetrated the first two layers. Each layer is engineered to exhibit a significant impedance mismatch, reducing the transfer of momentum between the layers.

The first layer (Strike Face) is typically made from hard ceramic like alumina oxide or boron carbide. The primary function of this layer is to deform the incoming projectile and to eliminate any sabots. In scenarios requiring protection against multiple hits, modular

tiles are employed to halt the propagation of cracks caused by the impact. These modular tiles also facilitate repair work, thereby prolonging the durability of the armor package. The second layer is designed to absorb and dissipate energy. Aramids, like Kevlar® and polymers such as UHMWPE are used in this layer for their ability decelerate and halt a penetrator.

The last layer (Fragment Catch Plate) is designed to catch any fragmentation or penetrator that has made it through the first two layers and reduce back face deformation. Typical materials for this fragment catch plate are alloyed toughened metals.

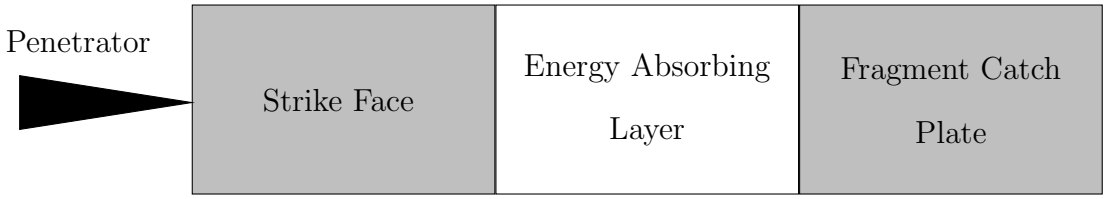

Figure 2.7: Diagram showing the different layers of ballistic armor.

Viscoelasticity

Polymers are viscoelastic, meaning the material simultaneously exhibits a combination of elastic and viscous behavior. The mechanical response is dependent on both time and temperature [4]. Figure 2.8 depicts the five general regions of viscoelastic behavior for amorphous, semi-crystalline and cross-linked polymers.

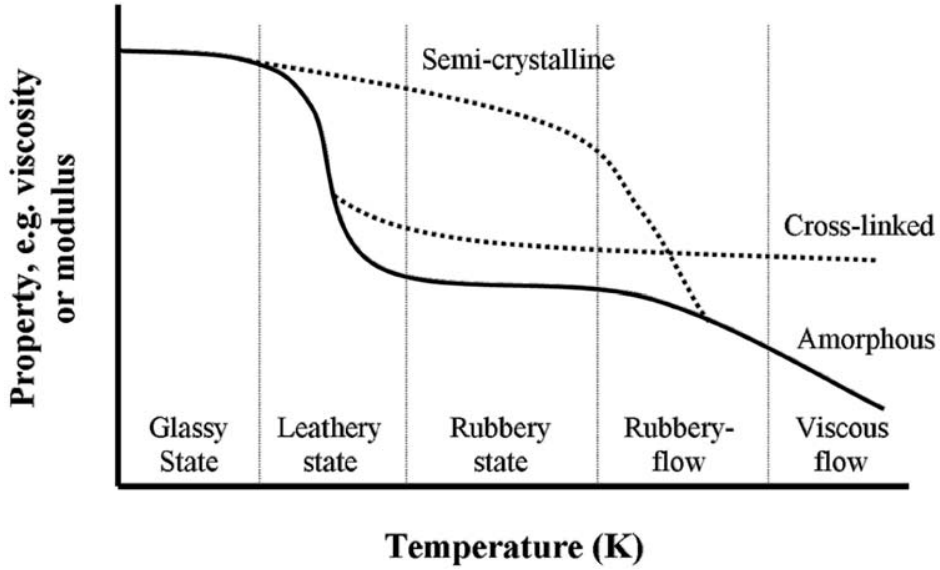

Figure 2.8: Five general regions of viscoelastic behavior with respect to temperature for polymers [8].

In its glassy state, the material exhibits its maximum bulk modulus and demonstrates the most elastic behavior. As the temperature rises, the modulus correspondingly decreases. The glass transition region is characterized by a drastic drop in the modulus, approximately by a factor of 1000, within a temperature range of 20°C to 30°C. In this region, the polymer exhibits characteristics similar to that of leather [4]. The rubbery plateau region inhabits the temperature range where the polymer can be stretched several hundred percent and still return back to the original position, assuming it is an amorphous polymer. The higher the molecular weight, the longer this plateau region extends [4]. If the polymer is semi-crystalline, the height and length of the plateau in the rubbery region changes with degree of crystallization until the melting temperature. As the temperature increases beyond the rubbery state, the physical chain entanglements relax and the polymer behaves similar to high viscosity fluids like SillyPutty® [4]. The final phase before melting is the viscous flow region where the material behaves like molasses [4]. All throughout the temperature ranges, polyethylene exhibits rate dependent properties.

Dynamic Mechanical Analysis (DMA) utilizes small cyclical deformations to characterize the viscoelasticity of materials. This process is also known as dynamic mechanical spectroscopy (DMS) [4]. DMA measures stiffness and dampening of a material by inducing a sinusoidal displacement and measuring the resulting stress as shown in Figure 2.9.

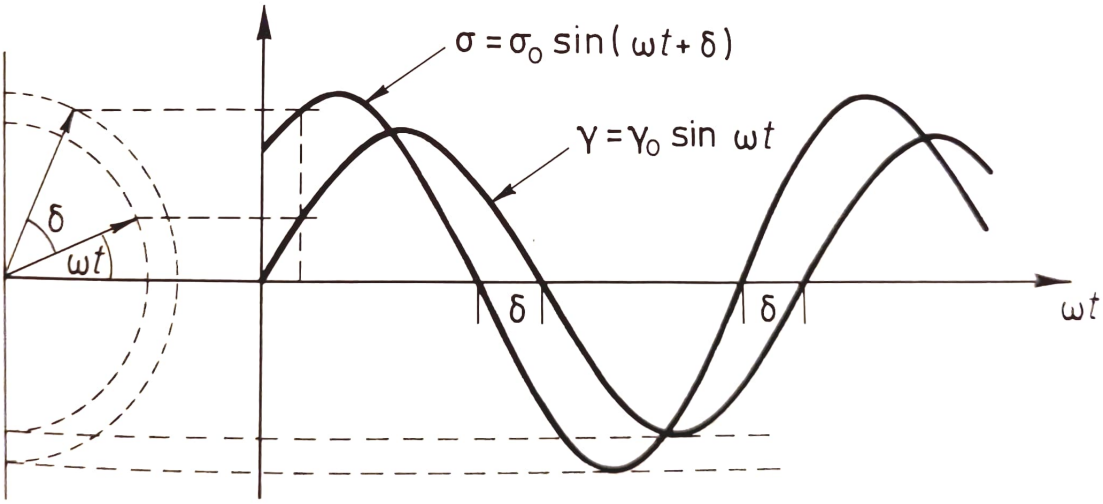

Figure 2.9: Dynamic Mechanical Analysis of the applied strain (represented as shear strain γ) and lagging stress ω [9].

The following derivation is adapted from [9].

Driving a sinusoidal shear strain of ϵ and an angular frequency of ω into a sample:

$$\epsilon = \epsilon_0 \sin(\omega t) \tag{2.1}$$

A linear viscoelastic material will have a sinusoidal stress response with a phase shift of δ as the stress will lag behind the strain.

$$\sigma = \sigma_0 \sin(\omega t + \delta) \tag{2.2}$$

The resulting stress vector from expanding Equation 2.2

$$\sigma = (\sigma_0 \cos\delta)\sin\omega t + (\sigma_0 \sin\delta)\cos\omega t \tag{2.3}$$

Therefore, the strain and stress can be related to each other with the strain in phase represented as $\sigma_0 \cos\delta$ and the 90° out of phase represented by $\sigma_0 \sin\delta$:

$$\sigma = \epsilon_0[E' \sin(\omega t) + E'' \cos(\omega t)] \tag{2.4}$$

Where the storage modulus (E') in Equation 2.4 is shown in Equation 2.5

$$E' = \frac{\sigma_0}{\epsilon_0}\cos\delta \tag{2.5}$$

and the loss modulus (E'') in Equation 2.4 is shown in Equation 2.6

$$E'' = \frac{\sigma_0}{\epsilon_0}\sin\delta \tag{2.6}$$

The $E'\epsilon$ is the stress component which is in phase with the sinusoidal strain, and $E''\epsilon$ is the out of phase stress component.

The complex modulus is expressed as, which is the sum of the in and out of phase components.

$$E^* = \frac{\sigma^*}{\epsilon^*} = \frac{\sigma_0}{\epsilon_0} exp\ i\delta = \frac{\sigma_0}{\epsilon_0}(\cos\delta + i\sin\delta) = E' + iE'' \tag{2.7}$$

The tangent of the phase angle is:

$$\tan\delta = \frac{E''}{E'} \tag{2.8}$$

Purely elastic solids have a $\tan\delta = 0$, where the response has no viscous component. But polymers can have a high dampening ratio in specific temperature ranges. The loss modulus,

E'' is the ability of a material to dampen and dissipate energy, typically as heat, which can be modeled as a dash-pot. The storage modulus, E' is the elastic portion of the response and can be modeled as a spring [9].

Polymer Aging

Despite polyethylene's high durability, the performance will decrease with exposure to harsh environments. As the polymer ages on the shelf it will oxidize and generate free radicals, decreasing the mechanical performance [80]. While bulk UHMWPE is known to have a high wear resistance and bio-compatibility, the material ages over time, which can cause cytotoxity from leaching. This reduces the overall lifespan of an implant, such as in an artificial hip [80]. The medical industry utilizes γ-ray's to increase the wear resistance of bulk UHMWPE implants. Exposing UHMWPE to γ-ray's creates crosslinks in the polymer, which reduces the chain mobility and slows the formations of fibrils on the surface [81]. The following are different mechanisms that age UHMWPE fiber reinforced composites depending on the environment faced.

Hydrolysis

Voids in the composite can trap water, which leads to increased weight, matrix dissolution and eventually cracking of the material. The hydrolysis reaction results in two products: one product with an extra hydrogen atom with a negative charge and the other product with a hydroxyl group. If the reaction is ionized, the first molecule will have a positive charge with two extra hydrogen atoms and the second product will be an oxygen atom containing a negative charge [82]. For a deeper understanding of hydrolysis, refer to [83].

The addition of salt or sea water can catalyze the oxidation and hydrolysis, accelerating the rate at which the polymer degrades [10].

The presence of both UV and water can promote cracking and cause pores to form in both the matrix and fibers as shown in Figure 2.10 [10]. Hydrolysis will embrittle the composite and cause the matrix and potentially the sizing on the surface of the fibers to erode.

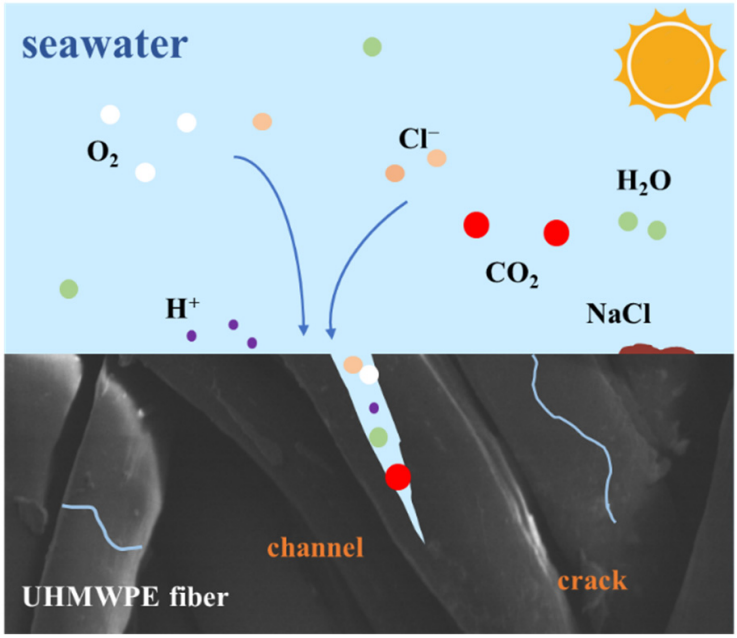

Figure 2.10: Sea water aging of UHMWPE creates channels and cracks where hydrolysis can occur within the composite [10].

Chain Scission

Chain scission is a process where the polymer chain breaks, lowering the average molecular weight [84]. This can occur from radiation such as high energy photons colliding with the polymer backbone which breaks the bond between the carbon-hydrogen or carbon-carbon in the polyethylene chain. Figure 2.11 depicts this scission process. Oxidation and hydrolysis can speed up the chain breakage. These new chains can recombine, or react with another molecular group like oxygen, water, free radicals, etc [84]. After scission the polymer can also form crosslinks with other polyethylene chains. However, it is likely that most of

the free radicals formed from the chain scission end up trapped and accelerate the oxidation process [81]. As the polyethylene is irradiated with X-rays, γ-rays, or electrons, the hydrogen can be released as a gas, along with any other paraffin's that remained in the matrix or in the fibers from manufacturing. Additionally, as UHMWPE ages with radiation, the crystallinity decreases and the polymer becomes more amorphous with new crosslinking [85]. At first, the polymer becomes a bit more flexible and transparent, potentially due to the heating effects from the radiation, but then shifts to become more brittle as the crosslinking density increases [85]. Eventually the aging turns this normally white UHMWPE to a yellow or brown colored material from the crosslinking.

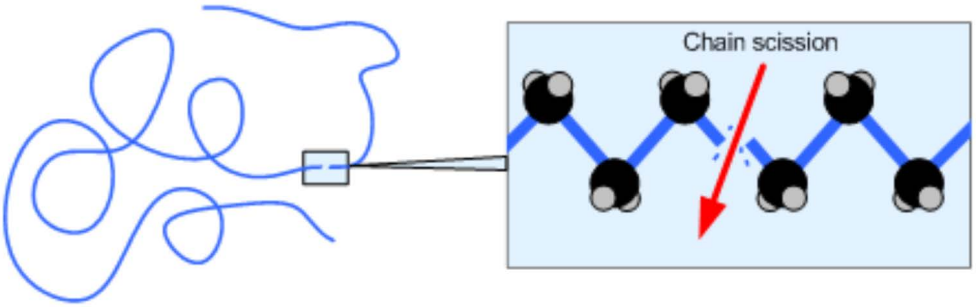

Figure 2.11: Polymer chain scission [11].

Crosslinking

Crosslinking forms networks between chains which increases the stiffness of the UHMWPE while decreasing the strain to failure. Figure 2.12 depicts this scission process via UV exposure. In bulk form UHMWPE, the crosslinking from radiation appears to saturate around 100 kGy [81]. Radiation also induces energy which can be absorbed as localized heating. This heat can turn a crystalline location into an amorphous state even after re-cooling [81].

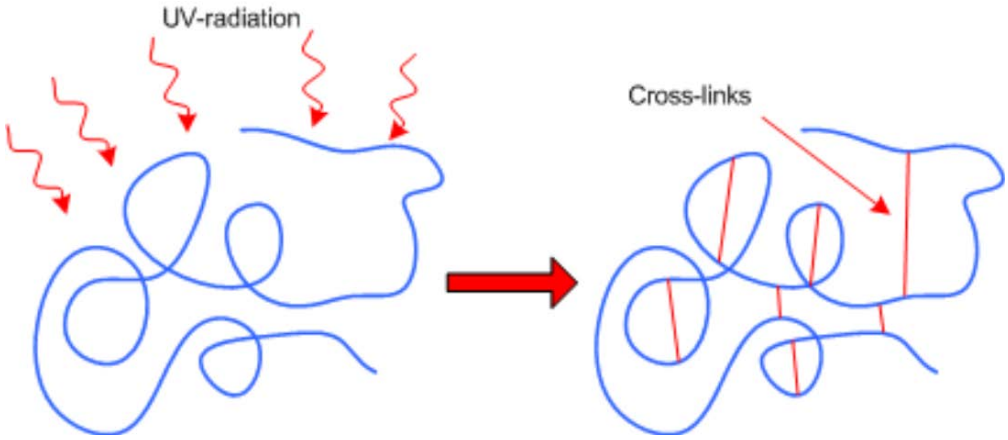

Figure 2.12: Polymer crosslinking [11].

Theoretically pure UHMWPE should not be affected by UV because polyethylene does not absorb radiation wavelengths longer than 190 nm. The shortest wavelength of UV is 290 nm. Studies of UHMWPE fibers after UV exposure prove otherwise [86]. UV testing on UHMWPE fibers has shown embrittlement, with a slight increase in modulus and hardening, marked by a sharp drop in toughness and tenacity [86]. This will lead to a decrease in $\tan\delta$ with UV as chain scission and crosslinking occurs. After UV exposure the fibers lose crystallinity [86]. Finally, UV damage occurs on the outside first and moves inward as observed by the transition of ductile failure to brittle failures in [86].

In summary, UV degradation triggers the movement of electrons to elevated energy levels, leading to the disruption of bonding mechanisms within the material. This process activates impurities, hastening other forms of aging like oxidation and hydrolysis. Consequently, these alterations in the material's physical structure affect its micro-structure and possibly its chemical composition, thereby influencing its mechanical properties.

All of these multi-physics aging mechanisms influence the mechanical properties of polymers, corresponding to a change in performance. For ballistics protection applications, aging has a large impact on the performance and reliability. The current method of determining the acceptable lifespan of body armor packages is typically done through

surveillance. Where several units are taken out of service and tested, if the armor stops a bullet, this age passes and wait another year to retest. This is contrast to a science-based approach of predicting the strength of materials and determining an acceptable lifespan. Much of the ballistics protection industry relies on empirical data for critical design parameters such as age or thickness.

Ballistic Standards

There are two leading governing bodies that draft industry standards when it comes to ballistics protection systems classifications. The National Institutes for Justice (NIJ) from the USA, and Home Office in the UK. Both are similar, but for brevity, only the NIJ standards will be covered in this document. The NIJ adopted a new standard for Ballistic Resistance of Body Armor Standard 0101.07, in October 2023, which changed how armors are rated from II-IV+ with other designations like (A), simplified into two categories based on threat: Rifle (RF) 1-3 and Handgun (HG) 1-2.

These ratings serve as indicators of the armor's protection levels, taking into consideration the potential for spall penetration and the maximum deformation at the rear of the armor. The V_{50} is defined as the velocity at which 50% of the impacts of the specified threat penetrate the armor. The nomenclature extends to V_0, which represents the maximum velocity where 0% of the shots will penetrate the target. These velocity values combined with the back face deformation (BFD) are used to determine the protection level. BFD is the material deformation out of plane from the impact. According to NIJ 0101.07, BFD must not exceed 44 mm, or statistically prove that there is a "95% confidence that 80% of all BFD depths will be 44 mm or less" [87]. This new standard includes guidance for submerging the armor in various substances for a period before removing to shoot. These substances are simulated environments that may be experienced in the field which new to this version of NIJ standards. Designers and end users are beginning to show interest in how the environment

alters the performance of the armor.

Ballistic Modeling

Determining the cross-sectional area of UHMWPE fibers and films to calculate the strength and modulus is experimentally challenging. Assuming a constant fiber volume fraction and material density, the form of specific strength and modulus are advantageous, as the mass per length of the composite or fiber can be found by a ruler and scale much easier than the microscopy needed to determine the cross-sectional area of a fiber.

Specific Strength and Modulus

Typically, the tensile strength of a fiber is measured in Newtons per square meter (N/m^2) and is calculated as the breaking force F_b (N) divided by the fiber cross-sectional area, A (m^2) as seen in Equation 2.9 [6].

$$\text{Tensile Strength} = \frac{F_b}{A} \tag{2.9}$$

Specific tensile strength incorporates the density of the fiber in the tensile strength as seen in Equation 2.10.

$$\text{Specific Tensile Strength} = \frac{\text{Tensile Strength}}{Density} = \frac{F_b}{A \cdot \rho} \tag{2.10}$$

Assuming that the gel-spun fibers are cylinders with the length L(m) and ρ (kg/m^3),

then the density of the cylinder is calculated in Equation 2.11.

$$\text{Density} = \rho = \frac{Mass}{Volume} = \frac{m}{V} = \frac{m}{A \cdot L} \tag{2.11}$$

By rearranging Equation 2.11 into Equation 2.12 and combining with Equation 2.10, results in Equation 2.13. Where the force, mass and length of the coupon are all easily determined experimentally to determine the specific tensile strength of the fiber [6].

$$\rho \cdot A = \frac{m}{L} \tag{2.12}$$

$$\text{Specific Tensile Strength} = \frac{F_b}{A \cdot \rho} = \frac{F_b \cdot L}{m} \tag{2.13}$$

Units for mass per length are commonly referred as $tex = 1\ g/km$, or a $dtex = 1\ g/10\ km$ [6, 88]. Since a Pascal (Pa) has the units of N/m^2, the conversion from conventional to fabric units is straightforward. For example, given an UHMWPE fiber with a density of 970 kg/m^3, and a tensile strength of 3.5 GPa, a modulus of 172 GPa would have a specific tensile strength of 36 cN/dtex with a specific modulus of 1800 cN/dtex using the values of Ultra-drawn UHMWPE from Table 2.1 and [5, 6]. Specific strength is a common way to measure and compare the strength to weight ratio pf materials as seen in Figure 2.13.

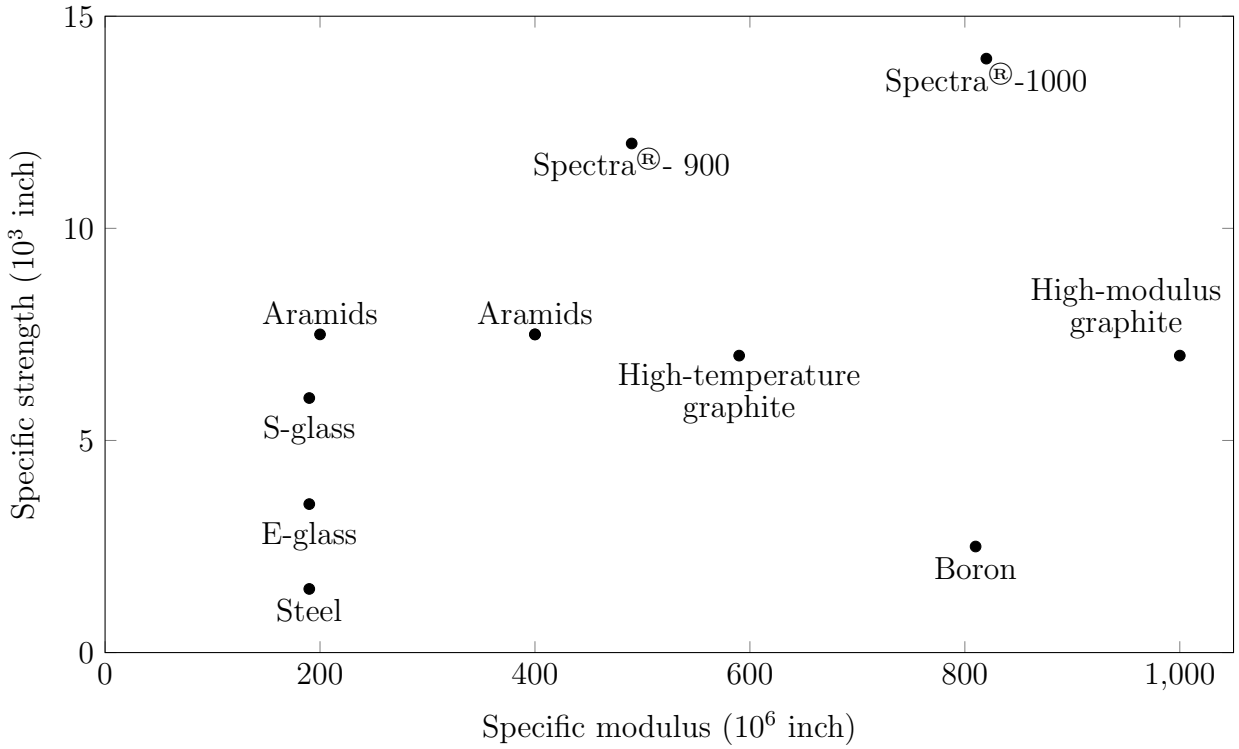

Figure 2.13: Comparison of specific strength vs specific modulus, where Spectra® is the UHMWPE fiber. Reproduced from [5].

Another important material property for understanding how UHMWPE responds to ballistic threats is the speed at which a strain wave travels through the fiber.

Speed of Sound

The speed of sound, C, in a material governs the strain wave propagation after an impact

$$C = \sqrt{\frac{E}{\rho}} \tag{2.14}$$

The material is moving behind this wave front at speed U, which causes an additional strain of $\epsilon_d = \frac{U}{C}$ [89]. Wave theory is still being developed for viscoelastic materials, and much of the science behind determining the appropriate thickness of materials for ballistics protection is empirical.

Engineering Models

Critical velocity is the relation of mechanical properties to ballistic performance, which theorizes that the strain generated in the system from the projectile impact at or above the critical velocity will break the fiber. Therefore, the critical velocity is defined in Equation 2.15 [89].

$$V = \sqrt{\frac{E}{\rho} \cdot \left(\varepsilon_i - \sqrt{2\varepsilon_c \cdot (1+\varepsilon) - \varepsilon^2}\right)} \tag{2.15}$$

However, for Dyneema® SK-76 fibers, this equation over predicts the velocity at which the fibers break by almost double. with Equation 2.15 $V = 1033\ m/s$, where ballistic studies have found the UHMWPE fibers fail at $V = 518\ m/s$ [89]. Part of this error is by assuming there is only axial stress [89, 90]. The other gap in prediction could be filled from using a viscoelastic model.

In 1999, a dimensionless parameter, Ω in Equation 2.17, was developed to compare various fiber reinforced composites for ballistics protection as seen in Equation 2.17 [91].

This parameter incorporates mechanical properties of the ballistics protection material and projectile. Assuming the fibers are linearly elastic, this parameter takes the specific toughness and velocity of the strain wave in the fiber along with the projectile's mass and area to compare the effectiveness of various armors [91].

With the assumption of a linear stress-strain curve, this model is designed with the function, f, which is for all combinations of fiber and projectile types, and AD is the areal density [89].

$$\frac{V_{50}}{\sqrt[3]{\Omega}} = f\left(\frac{AD_{\text{target}}}{AD_{\text{projectile}}}\right) \tag{2.16}$$

Where Ω (m^3/s^3) is calculated from Equation 2.17, where stress is represented by σ, ε is the strain, ρ is the density, and E is the modulus [89].

$$\Omega = \frac{\sigma \cdot \varepsilon}{2 \cdot \rho}\sqrt{\frac{E}{\rho}} \tag{2.17}$$

While these models are great for back of the envelope calculations, they have limitations, mainly that they assume the fibers behave linear elastically and do not account for multi-axial strain.

Analytical Models

Finite Element Analysis (FEA) models and hydrocodes have been developed to predict the ballistic performance of UHMWPE composites with higher fidelity than the engineering models. Many of these FEA models use an energy absorption approach and some have even incorporated viscoelastic effects with three element models [92]. Often times these models only account for the fiber strength and stiffness and ignore the matrix material properties [93, 94]. Other models have looked at orthogonal layers or lumped filament bundles to predict the mechanisms of failure [95].

More accurate models come from hydrocodes. These account for impacts where the

energy exceeds the materials' strength by an order of magnitude and as such assumes the material is in hydrodynamic behavior. See [96] for more explanation on the development and distinction of hydrocodes from FEA.

UHMWPE in both fiber and bulk form have been studied relatively well. However, the composite form of UHMWPE is relied on for safety in many applications. The science of how these composites behaves is underdeveloped and not fully understood. Unfortunately, the assessed values of the UHMWPE fibers in lab often greatly over perform the units found in the field [6]. Understanding the response of these materials after aging is essential to designing safe systems for the future. The work presented here seeks to aid and assist those developing both analytical and engineering models by providing them with viscoelastic and thermo-mechanical properties after multi-physics aging of these UHMWPE fiber reinforced composites.

EXPERIMENTAL METHODS

This chapter details the plans, procedures, and methodologies for the experiments herein.

Specimen Manufacturing and Preparation

When UHMWPE fibers are integrated with a matrix, typically a soft thermoplastic, the resulting structure exhibits low interlaminar shear strength. This characteristic tends to skew the outcomes of tensile testing conducted on multiple plies [2, 89, 97]. With a thicker sample, the fibers on the inner plys are loaded less from this phenomenon. As the coupon thickness increases, the reported tensile strength decreases with traditionally gripped tensile coupons. To accurately characterize the composites, a different testing approach was developed and is recorded in this chapter. These composites are distributed as a consolidated sheet of $[0/90]_2$ in a roll 162 cm wide. For clarity sake, one layer is defined as $[0/90]_2$, rather than describing it as one ply.

Material Selection

Rolls of 162 cm wide single layer Dyneema® HB-210, HB-212, and Honeywell Spectra Shield® 5241 (SR-5241) were acquired through material distributors. A 95 layer consolidated HB-212 panel was purchased from ITEN Defense in Ohio. HB-210 is made with SK-99 Dyneema® fibers, and a polyurethane rubber matrix (PUR). HB-212 is also made with the same SK-99 fibers and consolidated with a synthetic rubber matrix made by Kraton® [98].

Sample Preparation

Several methods for preparing test coupons were evaluated to identify the most effective technique for producing samples for subsequent testing. Considering the material is

engineered to halt bullets and guard against stab wounds, it is not surprising that cutting it into testable sample sizes presents a significant challenge.

Cutting A laser cutter, waterjet, hot knife, die punches, rotary cutter, scissors, serrated scissors, band saws, miter saws, tile saws, razor blade, and medical grade scalpels were all explored as methods to cut the UHMWPE, each with varying degrees of success.

The laser cutter successfully made it through all single layer materials, but struggled with multiple plys. The thermoplastic polyethylene and matrix would melt and flow down into the cut. The quality of the single ply cuts varied. Optimization of power, travel speed, and the number of passes was conducted to minimize the effects of melted edges. Scanning Electron Microscope (SEM) imaging revealed a heat-affected zone measuring approximately 350 μm, as shown by the SEM image in Figure 3.1.

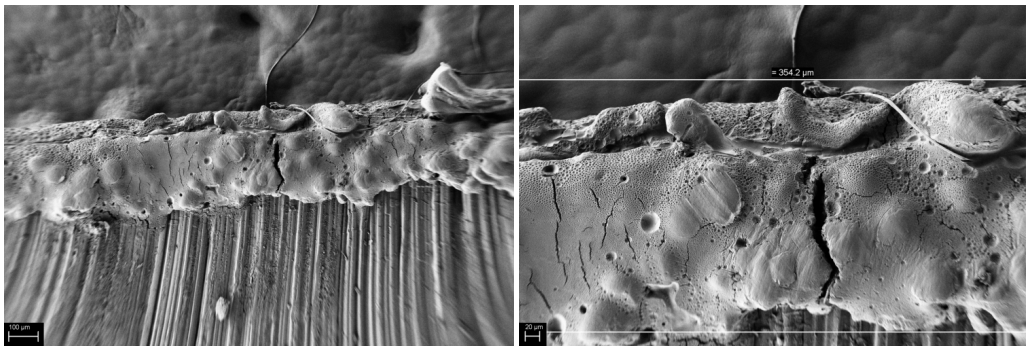

Figure 3.1: Heat affected zone of laser cut HB-210 (a) enlarged section (b) melted edge of HB-210 layer.

Additionally, the quality control of the coupon size was not reliable when using the laser cutter in batched cuts. An even grid of rectangles 25 mm by 10 mm with 5 mm spacing was loaded into the laser cutter program to cut out multiple coupons at a time. Issues arose as a fan inside the laser cutter would cause the composite to move during cutting. To solve this, a frame was built, and the fabric was stretched over the frame, similar to a canvas for

painting. However, since this material is unidirectional, it did not stretch evenly and fibers became misaligned. Laser cutting multiple coupons for dynamic mechanical analysis proved less than optimal. Laser cutting was ultimately discontinued as the edge effects of the melted region dominated the DMA tests.

The waterjet at Montana State University was not large enough to cut the HB-212 95 layer plate; therefore, the waterjet at Slabworks of Montana was utilized to cut 2.54 cm by 26.6 cm rectangles from the plate, and 2.54 cm by 162 cm strips from the single layer roll. This waterjet is traditionally used to cut: granite, quartz and other stones for commercial and residential use. The abrasive solution was not changed or cleaned before cutting. For pressed panels of multiple plys, waterjetting has an advantage for cutting over other methods, but the abrasive may result in interlaminar deposits between the plys, contaminating the test samples. Others have had success in cutting with a femptosecond laser or a small waterjet [95, 99].

A hot knife was used to cut larger strips off the rolls of single ply material, but this required the edges to be cleaned up before testing. The hot knife method did not successfully cut the thinner (<25 layers) pressed panels. Die punches and leather punches were tested to make DMA shaped coupons. This required a large amount of force to cut through even a single ply. G10, rubber mats, and wood sheets were used as backing material to allow the punch to shear the UHMWPE sheet. This method is not recommended based on the ergonomic strain and lack of consistency.

Rotary cutters, scissors, serrated scissors, and paper/fabric shear all failed to cut the UHMWPE composites. The use of the fine-toothed blade band saw and miter saw caused fiber pullout and fraying, rendering the samples unusable. Using a diamond blade ceramic tile saw is not recommended for cutting due to fraying and edge effects from localized heating.

The most effective method for cutting coupons was by using a medical scalpel with disposable blades. Aluminum templates and fixtures were designed and manufactured to

ensure coupon uniformity between testing series.

Pressing Plates (Ply Consolidation) Single semi-preg $[0/90]_2$, sheets were cut using both a hot knife and scalpel into 30 cm squares and placed between two pieces of Teflon film. These sheets were stacked with 15 and 25 layers and pressed at 500 kPa (the maximum this machine could produce) and held at 130°C for 1.5 hours. Figure 3.2 shows the preparation to make a smooth finish planar consolidated plate in the heat press.

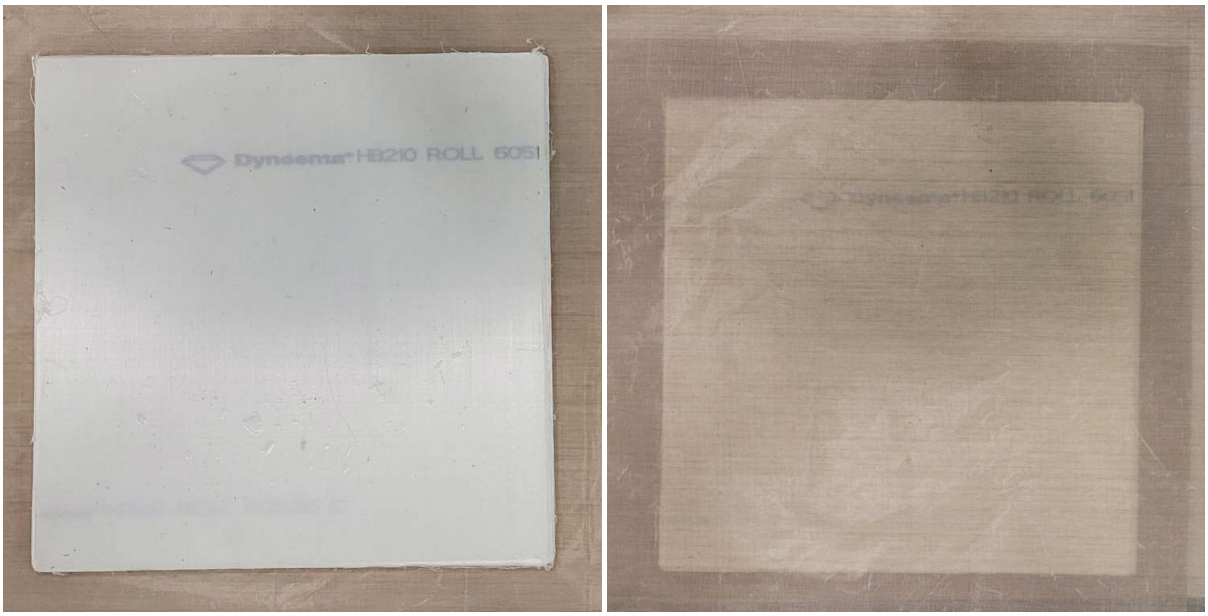

Figure 3.2: Square HB-210 (a) without Teflon paper cover (b) with Teflon paper ready to hot press.

Round plates were also produced as seen in Figure 3.3.

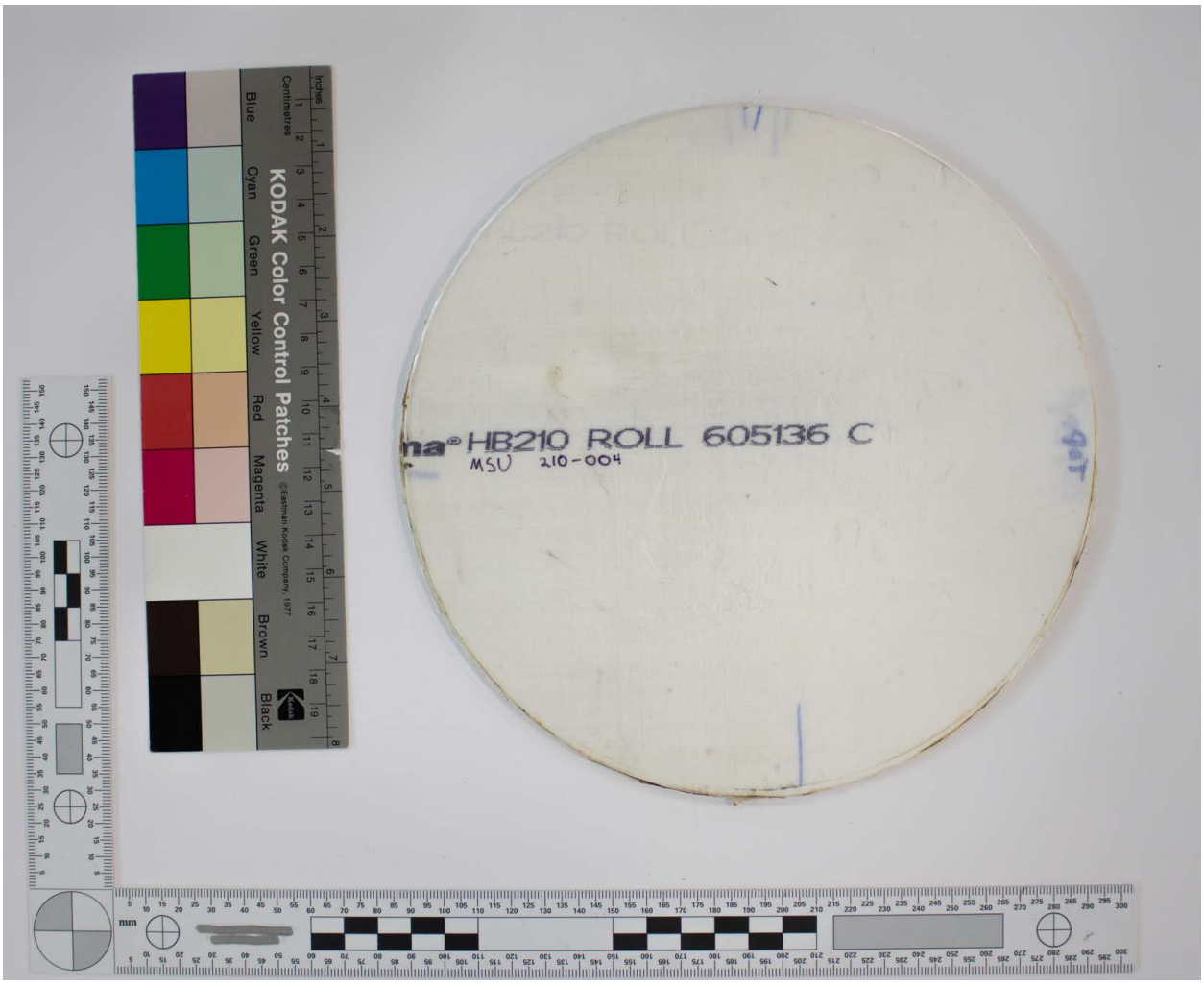

Figure 3.3: Round HB-210 plate of 25 layers.

These pressed sheets were cut into 2.54 cm wide strips to test in three point bending. Additionally, these coupons were tabbed for tensile testing. Since these are continuous fiber composites, the tensile coupons are not dog-bone shaped, but rectangular.

Another method attempted for consolidation of the plys was using a vacuum bag on an aluminum plate in an oven at 130°C for 12 hours under a 10 kPa vacuum. This method was not utilized as the top surface had imperfections and wrinkles from the vacuum bag. A comparison of the surface produced by each consolidation method is illustrated in Figure 3.4. The left side of the image depicts the top face within the vacuum bag, while the right

side displays the top face of the heat-pressed HB-210 panel.

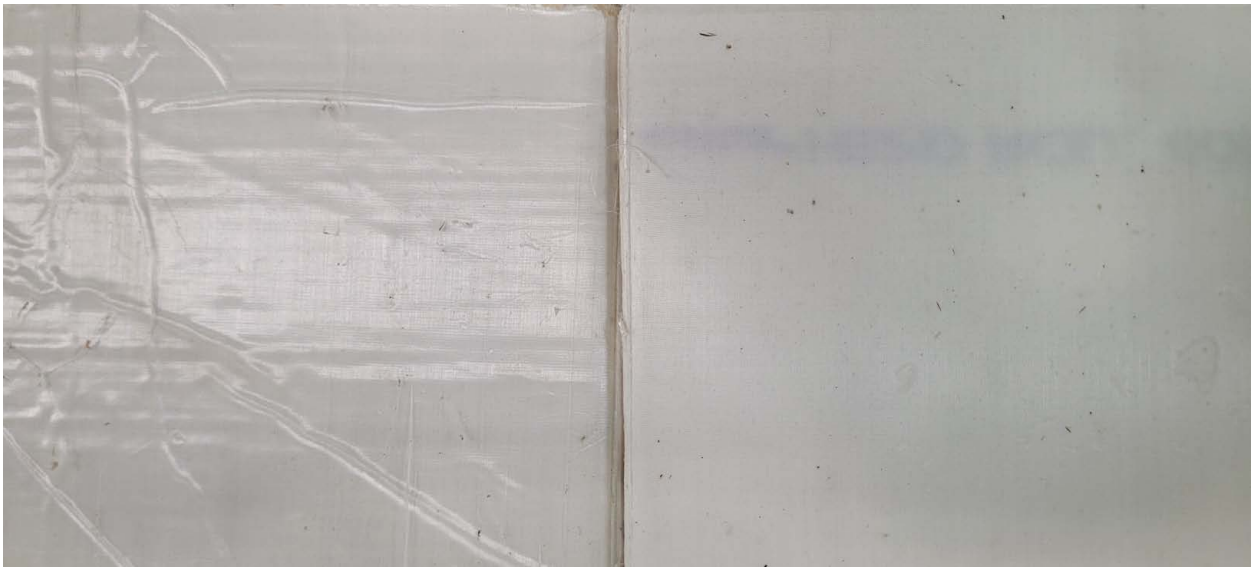

Figure 3.4: Surface finish comparison of plate consolidation manufacturing methods.

Benchmark Testing

Attempts at three point bending tests of the 95 layer 2.54 cm by 26.6 cm pressed panels at a quasi-static rate were conducted. These tests failed from ply delamination at 225 N or 50 lb-f, which is much lower than the strength of the material. Additional tensile tests were attempted in tension on the 95 ply samples but failed at the grips. Figure 3.5 from top to bottom shows an untested 95 layer HB-212 coupon, failure from delamination at 175 N during a three-point bending test, another three-point bending test delamination at 225 N, and the bottom picture is a grip slip failure in tension.

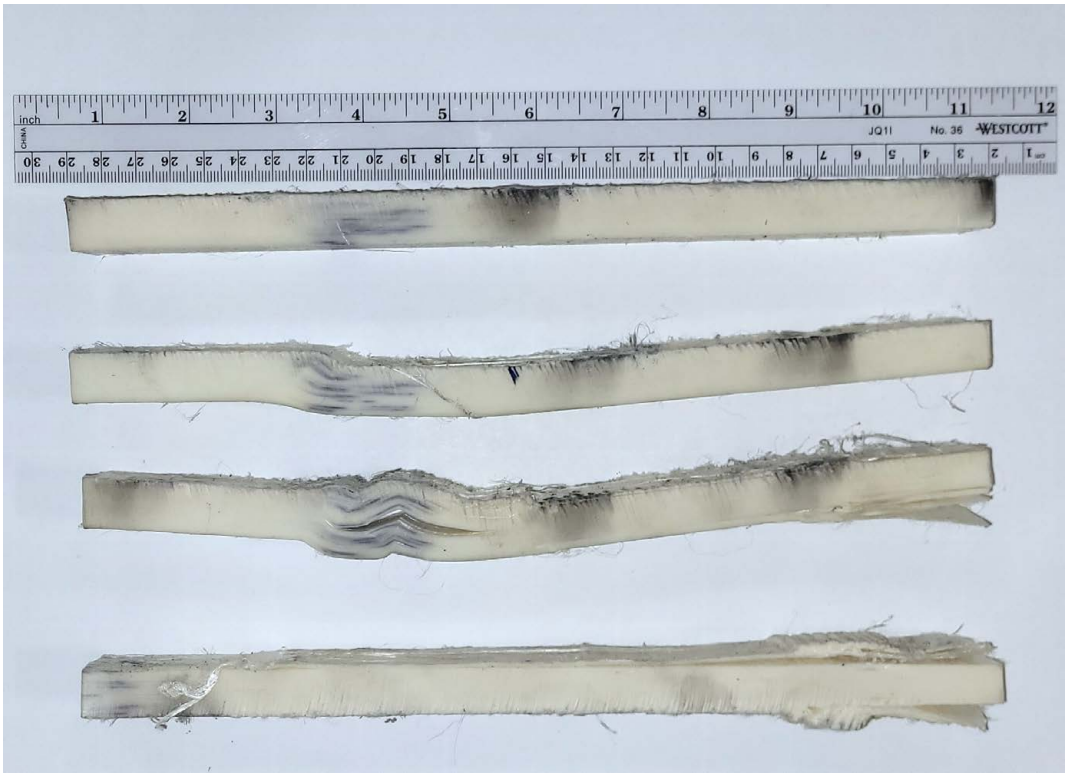

Figure 3.5: Initial testing methodology of UHMWPE composites.

In order to conduct accurate quasi-static tests a new griping procedure was developed. With the assistance of Dan Samborsky, Tom Jungst, and several undergraduate students, custom capstan grips were manufactured for tensile testing.

Figure 3.6 shows the relative size and layout of the grips. The bottom of grips, has an offset tab, the tangent of the roller is co-linear with the load cell, making the coupon also co-linear with the load cell, so that there is no bending during testing.

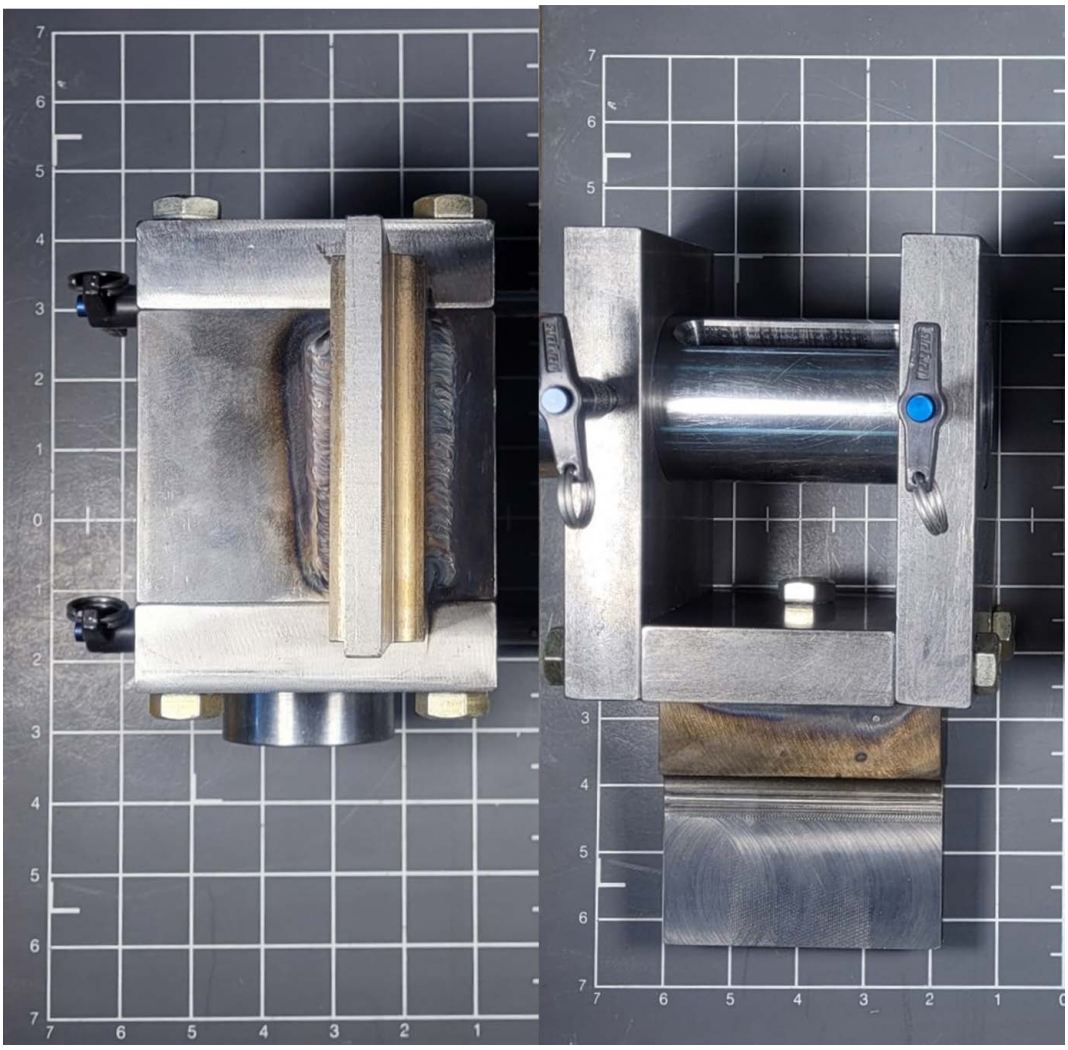

Figure 3.6: Bottom and side view of custom capstan grips manufactured for tensile testing of UHMWPE composites.

5 cm wide strips of single layer UHMWPE composites were cut using a scalpel on a jig. Each end of the strip was wound once in the other direction around a piece of G10 used as an anchor in the slit inside the roller on the capstan to best prevent the composite from slipping on the clamp. After inserting the G10 end into the roller, these coupons were wound twice around the capstan. A series of tests were conducted with a single wind around the rollers in the grips, these experiments showed that two windings were necessary to prevent grip slippage.

The rate of displacement for these tests was: 25.4 mm per minute with a preload of 45 N. Optical strain and crosshead travel were recorded in lieu of an extensometer and strain gauge as both failed adhesion to the composite. The gauge section for all tests was 30.48 cm. To prevent delamination of the 90° plys, the coupons were mounted with the 0° fibers along the roller. The temperature in the room was 20°C to 21°C with a relative humidity between 20% and 36% during the tests.

Tabbing

Due to the low coefficient of friction of UHMWPE composites, grip slippage occurs during tensile tests. To mitigate this issue, single layer, five-layer, and ten-layer UHMWPE fiber reinforced composites were tabbed with G10 and two-part epoxy for tensile testing.

Differential Scanning Calorimetry

Differential Scanning Calorimetry (DSC) was used to characterize the UHMWPE fiber reinforced composite's response to temperature shifts. The goal of this experiment was to determine the glass transition temperature, melting temperature, and relaxation temperatures to characterize the UHMWPE thermoanalytical response.

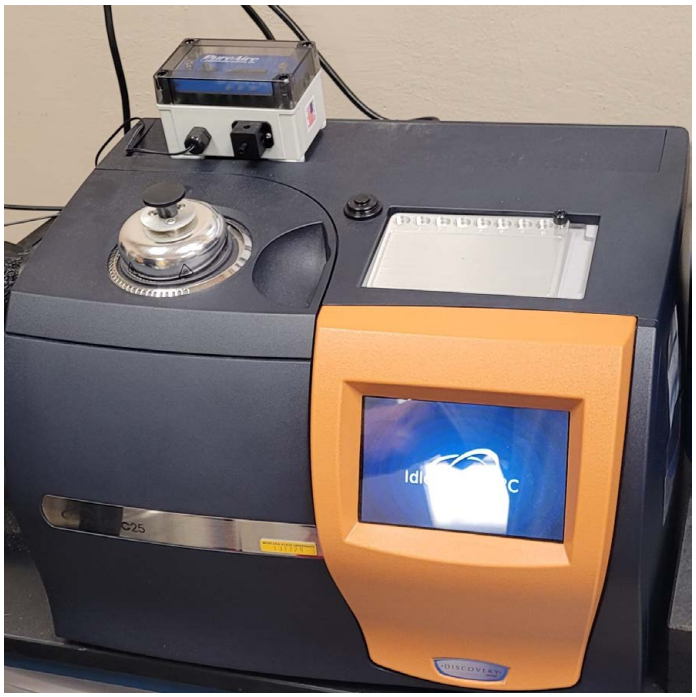

Figure 3.7: TA Differential Scanning Calorimetry Machine (DSC 25).

Figure 3.8 shows the sample size of UHMWPE fiber reinforced composites cut to fit inside a DSC cup. From left to right is a piece of UHMWPE composites, the DSC cup lid, the DSC cup, and a sealed DSC cup after loading with 25 mg of UHMWPE composite.

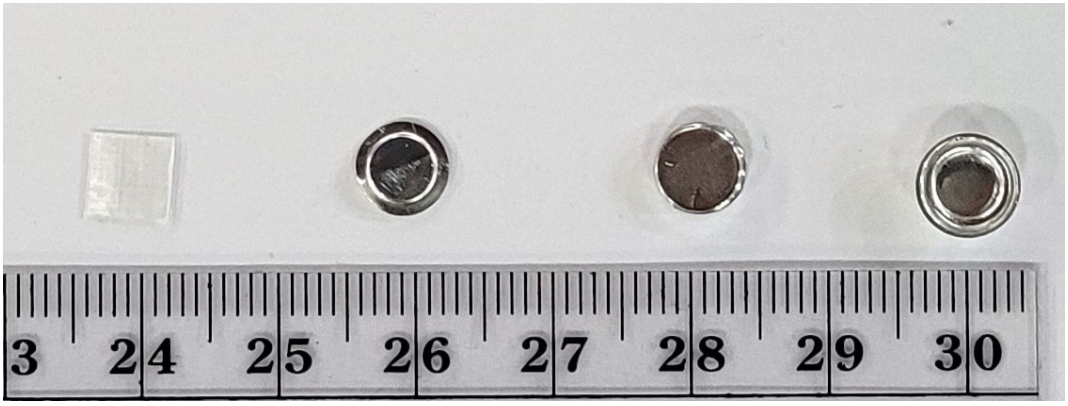

Figure 3.8: DSC sample preparation.

Multiple experimental series of five tests on each type of UHMWPE fiber reinforced composites were conducted varying the temperature range and rate. The temperature was increase at rates of 5°C/min, 10°C/min, and 20°C/min with a temperature range was from -150°C to 200°C. Since this is a composite, there were no discernible transitions through DSC compared to single material testing. The non-conclusive results are not included in this body of work. If the constituent parts of this composite were able to be obtained, DSC would yield useful insights into how this composite responds to thermal aging.

Dynamic Mechanical Analysis

A TA Instruments Q-800 Dynamic Mechanical Analyzer was used to characterize the viscoelastic response of the composites. The single layer coupons were loaded in the same orientation for all test, as this composite is not symmetric. The 0° face was placed towards the back of the clamp and the 90° was towards the front of the clamp to prevent delamination, with the exception of the $[\pm 45]_2$. Partway through this research the DMA tensile clamp was changed.

After the original equipment manufacturer tensile clamp was deemed defective, a secondary clamp was designed and fabricated. This new clamp improved on the previous

design by allowing the clamping force to be applied in compression through a screw rather than through the screw and a hinge. Two different sizes of samples were used to accommodate the two different tensile clamps, ensuring that all the fibers were loaded in tension during the test. The width of the second clamp was slightly smaller than the original, resulting in a change in sample dimensions from 25 mm by 10 mm to 25 mm by 7.5 mm. The width changed to ensure that the mass was balanced over the dovetail and centered on the axis. All tested coupons were made of single layer UHMWPE fiber reinforced composites.

Figure 3.9: TA Q800 Dynamic Mechanical Analysis machine.

Temperature Ramp

During dynamic mechanical analysis, the temperature of the UHMWPE fiber reinforced composites was varied to characterize the viscoelastic response across the working temperature range. The coupons were cooled using liquid nitrogen-cooled nitrogen gas purge. A preload of 0.1 N was applied before subjecting the samples to a sinusoidal frequency of 1 Hz at 5 MPa stress. The temperature was then increased from -50°C to 100°C at a rate of

3°C/min, all within a nitrogen gas environment.

Creep

Creep tests were conducted to characterize the strain response and susceptibility to creep after aging. The procedure involved initially holding the temperature at 35°C for 10 minutes without applying a load, ensuring uniform temperature throughout the thickness of the single layer $[0/90]_2$ UHMWPE composite. A preload of 0.1 N was then applied before maintaining a 5 MPa stress for 10 minutes, followed by unloading the stress and recording the strain for 20 minutes. Five samples of single layer HB-210 for each aging group were tested. To ensure precision, DMA tests were carried out at a constant temperature of 35°C, maintained for five minutes before and throughout the test duration, ensuring uniform temperature distribution within the composite for accurate polymer analysis.

Strain Rate Ramp

To characterize the complex modulus across various strain rates, samples of UHMWPE fiber reinforced composites were held at a constant temperature of 30°C for five minutes to achieve thermal equilibrium. A preload of 0.1 N was applied before subjecting the samples to a sinusoidal strain rate, gradually increased up to the maximum parameters of the DMA machine. Due to machine limitations, a strain of 0.03% was applied to each sample across a frequency range of 1 Hz to 200 Hz, which fell within the linear portion of the elastic region of all UHMWPE fiber reinforced composites tested. A minimum of five DMA tests were conducted for each aging condition to characterize the behavior, with the mean average material property reported along with the error bars representing the 95% confidence interval.

Soaking

Both single layer and pressed panel UHMWPE composites were aged in simulated sea water and distilled water for nearly two years at room temperature, ranging between 18 °C and 23 °C.

Two types of environments were prepared according to ASTM D-1141-52 Formula A, as outlined in Table 1, Section 4. Each clean container was filled with 3 liters of distilled water, and 125.85 g of "Sea Salt", as specified in the ASTM standard was added. The mixture was vigorously shaken with a lid until the salt dissolved. The pH of the solution was not monitored; therefore, no sodium hydroxide or hydrochloric acid was introduced, nor were heavy metals. Separate containers were utilized for each type of matrix. The waterjet cut 95 layer HB-212 pressed panels were placed in separate containers, each filled with 3 liters of distilled water and the simulated sea water mixture, for aging.

The 2.54 cm by 26.6 cm waterjet cut consolidated HB-212 95 layer pressed panel coupons were placed in both the salt water and distilled water to age. The pressed panel coupons are buoyant, therefore, stainless steel mesh with an extra piece of stainless steel was used to weigh it down. The mesh was placed around the coupons to allow the water to contact all sides of the coupon for diffusion and hydrolysis to occur.

Both single ply HB-210 and HB-212 samples were precisely cut using a scalpel and positioned inside the stainless steel mesh and submerged in the water filled containers. Three smaller DMA shaped coupons were left floating in a separate glass jars to observe when buoyancy was lost.

The weight of each coupon was measured and recorded before soaking. Periodic measurements of the weight of each sample were taken throughout the 669 day aging process. In order to measure water uptake, the 95 layer coupons were removed from soaking and left to air dry for 1 hour in order for the excess surface water to evaporate before measuring

the weight. The single layer samples were left out for 30 minutes to let the excess surface water evaporate before measuring the weight and replacing inside the jars. After 49 days, the stainless steel mesh began to show signs of corrosion in the single layer containers. A second round of jars with distilled water and salt water were created using the same ASTM standard and the samples of HB-210 and HB-212 were soaked without the stainless steel mesh. A separate container with just the stainless mesh was placed in a container without any UHMWPE to monitor corrosion and precipitate in the water.

Hygrothermal

The hygrothermal aging combined temperature and humidity cycling following ASTM G154, cycle 4, without the UV irradiance to isolate the effects of UV from hygrothermal aging, which are summarized in Table 3.1.

Table 3.1: Hygrothermal Aging Exposure Cycle

Condition	**Duration**	**Temperature**
Evaporation	8 hours	70 (±3)°C
Condensation	4 hours	50 (±3)°C

Single ply Dyneema® HB-210 and HB-212 samples were held for 8 hours at 70°C before turning off the UV bulbs and reducing the temperature to 50°C for 4 hours and then repeating the cycle for the specified time with the humidity and water being present in the test chamber.

Oven Aging

Single ply Dyneema® HB-210 and HB-212 samples were placed into an oven and held at 70°C for 8 hours before reducing to 50°C for 4 hours and cycling between the two temperatures in an oven without added humidity. Table 3.2 summarizes the aging conditions. The relative humidity inside the building was on average 20% for the duration of the aging.

Table 3.2: Oven Aging (Dry) Exposure Cycle

Duration	**Temperature**
8 hours	70 (±3)°C
4 hours	50 (±3)°C

Isothermal aging of single layer HB-210 was done at 70°C and at 50°C in these same ovens for 25, 50 and 100 hours.

Radiation Sources

Ultra-Violet (UV), X-ray, γ-ray, and neutron sources were used to age the UHMWPE fiber reinforced composites.

UV Source

Single ply samples of HB-210 were cut into 75 mm by 150 mm rectangles and mounted inside the Q-Labs QUV Accelerated Weathering Tester, which simultaneously simulated dew, temperature fluctuations, and exposed the samples to UV radiation. One side of the ply was exposed to UV and the humidity/dew simulator, while the other side was held up against the aluminum fixture.

Table 3.3: ASTM G154 UV Exposure Cycle 4 (modified)

Lamp	**Typical Irradiance**	**Approximate Wavelength**	**Exposure Cycle**
UVA-340	1.2 W/(m^2· nm)	340 nm	8 hours UV at 70 (±3)°C 4 hours Condensation at 50 (±3)°C

This accelerated aging was based on ASTM G154 and ASTM G151, the standard practice for exposing nonmetallic materials in accelerated test devices that use laboratory light sources. The UVA-340 nm bulbs were set to an irradiance of 1.2 W/(mm^2 · nm) for 8 hours and held at a temperature of 70°C before turning off the UV bulbs and reducing the temperature to 50°C for 4 hours.

This cycle repeated until samples were removed after 100 hours, 200 hours, 400 hours, and 800 hours of UV exposure, and evaluated by Dynamic Mechanical Analysis (DMA) and a Scanning Electron Microscope (SEM). 100 hours is approximately one year of average irradiance in the Northern New Mexico. The samples were repositioned according to ASTM G151 during testing to ensure uniform UV exposure.

X-Ray Source

An X-RAD320 cabinet was used to irradiate single layer HB-210, HB-212 and SR-5241. Samples were placed within viewing window of the collimator and irradiated one at a time. Table 3.4 shows the total measured dose, time exposed, and calculated average dose rate for the X-ray aging.

Table 3.4: X-ray Exposure for HB-210, HB-212, and SR-5241

Measured Dose (Gy)	**Exposure Time (s)**	**Average Dose Rate (Gy/min)**
1	122±0	0.49
5	621±3	0.48
10	1272±8	0.47
20	2595±11	0.46

Gamma-Ray Source

A Gammacell 220 at Oregon State University used a ^{60}Co to irradiate single layer HB-210, HB-212, and SR-5241 UHMWPE composites.

These samples were cut using a scalpel into 12.7 cm squares, and placed in separate zippered top plastic bags and loaded together in the Gammacell 220 for each dose. Table 3.5 contains the total dose detected, time exposed and calculated average dose rate for the γ-ray aging.

Table 3.5: γ-ray Exposure for HB-210, HB-212, and SR-5241, Dose Rate = 42 Gy/min

Measured Dose (kGy)	**Exposure Time (min)**
0.1	2.3
1	23.7
10	237
100	2370

Neutron Source

The thermal column in the research reactor at the Oregon State University Radiation Center was used to irradiate single layers of HB-210, HB-212, and SR-5241 with neutrons. Samples were cut using a scalpel into 10 cm squares and mounted on the stringer inside plastic bags before insertion into the thermal column.

Scanning Electron Microscope

UHMWPE is not a good conductor of electricity. Polyethylene is commonly used to insulate many types of residential and commercial wires. Before using the field emission scanning electron microscope (SEM), the coupons were placed onto a conductive carbon tape on the SEM slide. The samples were coated with iridium to conduct the electrons during imaging. The iridium target was turned on for 60 seconds at 2 mA with the UHMWPE mounted on the slide. The SEM used for all imaging in this work was a Zeiss SUPRA 55VP located in the Imaging and Chemical Analysis Laboratory (ICAL) at Montana State University.

Figure 3.10 is an example of a polished resin puck with UHMWPE fiber reinforced composites cross-sections to optically determine the axial fiber area. These cast resin pucks were polished through a series of increasing sandpaper grit sizes before imaging on an optical microscope. The soft thermoplastic fiber surface smeared during polishing preventing a clear view of the fiber cross section. A high grit polish was used on a final pass of one puck. Because the composite is softer than the resin puck, the polish contaminated the sample surface. Through multiple polishing procedures and mounting techniques, the fiber cross sectional area was not able to be determined either through an optical microscope or SEM.

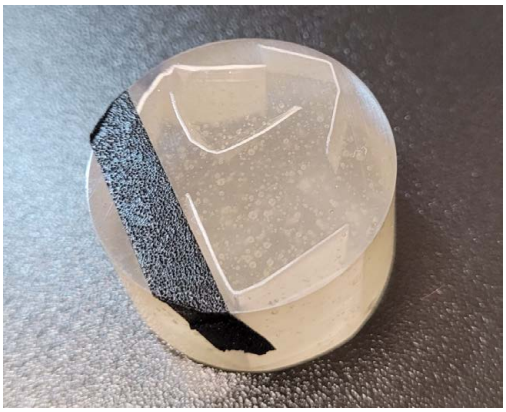

Figure 3.10: Resin puck prepped with carbon tape and coated with iridium for SEM imaging.

Figure 3.11 is an example of the surface of a $[0/90]_2$ cross sectional area of UHMWPE composites after polishing in the SEM. The 90° fiber direction in the center of the photo, where the two 0° fiber plys are on the top and bottom of the image respectively. Although, the 0° fiber layer appears as a solid section due to the localized heating and melting during the polishing process.

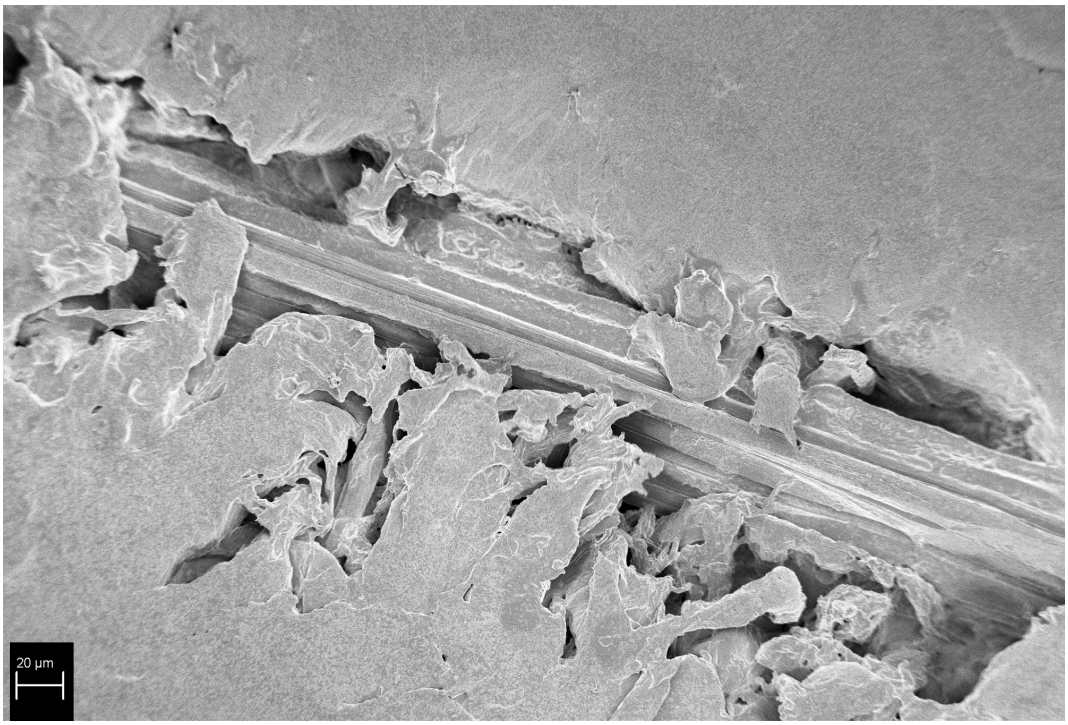

Figure 3.11: SEM image of a cross-sectional area of $[0/90]_2$ UHMWPE composite after polishing.

QUASI-STATIC TESTING

Tensile Testing

Single layer UHMWPE fiber reinforced composites were mounted into the custom capstan grips.

Figure 4.1 is an unaged coupon of UHMWPE fiber reinforced composite 5 cm wide mounted in a 8562 Instron servo-electric test machine.

Figure 4.1: Unaged tensile coupon mounted on capstan grips, 30 cm center to center length.

Figure 4.2 illustrates the failure process of a single layer of UHMWPE fiber reinforced composite captured in a time-stop photo during testing. From left to right, the images show

the initial condition, the onset of fiber failure, and the conclusion of the test. The camera angle presents the 90° face towards the viewer, while the 0° ply faces away. Notably, all samples failed at the center of the gauge section.

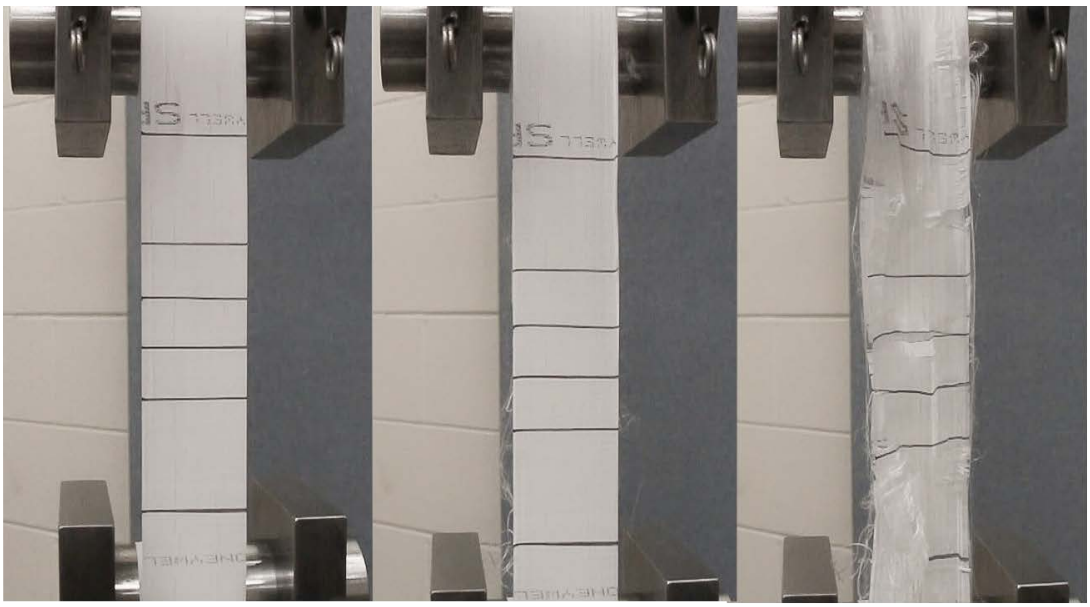

Figure 4.2: Typical tensile test failure progression in capstan grips.

The temperature and relative humidity in the room during the tensile test series recorded in Table 4.1.

Table 4.1: Ambient Conditions During Tensile Testing

Material	**Temperature (°C)**	**Relative Humidity (%)**
HB-210	20.5	22
HB-212	20.8	22
SR-5241	20.6	37

Twelve samples were tested for each type of UHMWPE fiber reinforced composites. The results are summarized in Table 4.2, where the strain is reported from the value recorded at

max load, and the tensile strength is calculated from the entire layup $[0/90]_2$ and not the fiber cross-section area in the 0° direction.

HB-210 has the highest average tensile strength and strain at maximum load from the testing series, while HB-212 and SR-5241 have a similar tensile strength and strain at maximum failure. However, the HB-212 strain at maximum load is on average a percent less and has a standard deviation three times higher than HB-210. HB-212 and HB-210 have the same fiber type, but different matrix material. The variance between the values of load and strain is most likely due to fiber misalignment in sample preparation. The synthetic rubber matrix of the HB-212 has a tacky feel and is more soft compared to the PUR matrix of HB-210 and SR-5241. Even though the same jig and sample preparation procedure was used, the softness and deformability of the single layer HB-212 prevented the alignment of the fibers during cutting compared to the SR-5241 and HB-210. The SR-5241 has a similar fiber volume fraction to HB-210 and HB-212 and has the same type of PUR matrix as the HB-210. These fibers are made from a gel-spinning process with paraffin wax rather than decalin, ultimately producing a fiber with a lower strength as observed in Table 4.2. Additionally, the relative humidity was higher during the SR-5241 series than the other series which contributes to a decrease in performance of the UHMWPE fibers.

Table 4.2: Tensile Strength of Single Layer UHMWPE

	Strength (MPa)	**Std. Dev.**	**Strain (%)**	**Std. Dev.**
HB-210	1280	145	2.7	0.3
HB-212	895	195	1.5	1.0
SR-5241	875	158	1.3	0.2

Due to the long length, and flexible nature of the composite some warpage occurred in cutting. This led to fiber misalignment in the tensile tests, where one side of the sample

would fail first and tear across as seen in Figure 4.3.

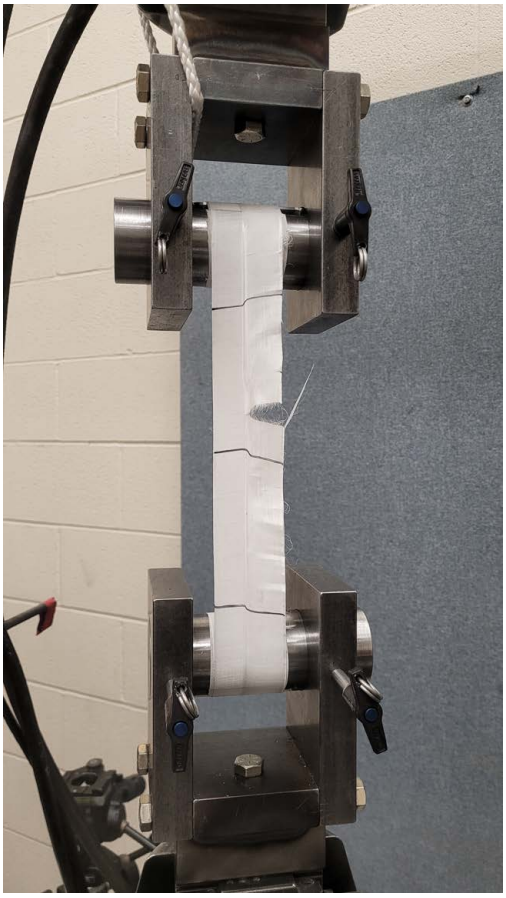

Figure 4.3: Fiber misalignment in tensile coupon evidenced by tearing in a rejected HB-212 test.

In Figure 4.4 (a), a coupon is incorrectly mounted, presenting the 90° face to the grips, which leads to ply delamination and grip slippage. To mitigate grip slippage, all samples were correctly oriented with the 0° face inward, as demonstrated in Figure 4.4 (b).

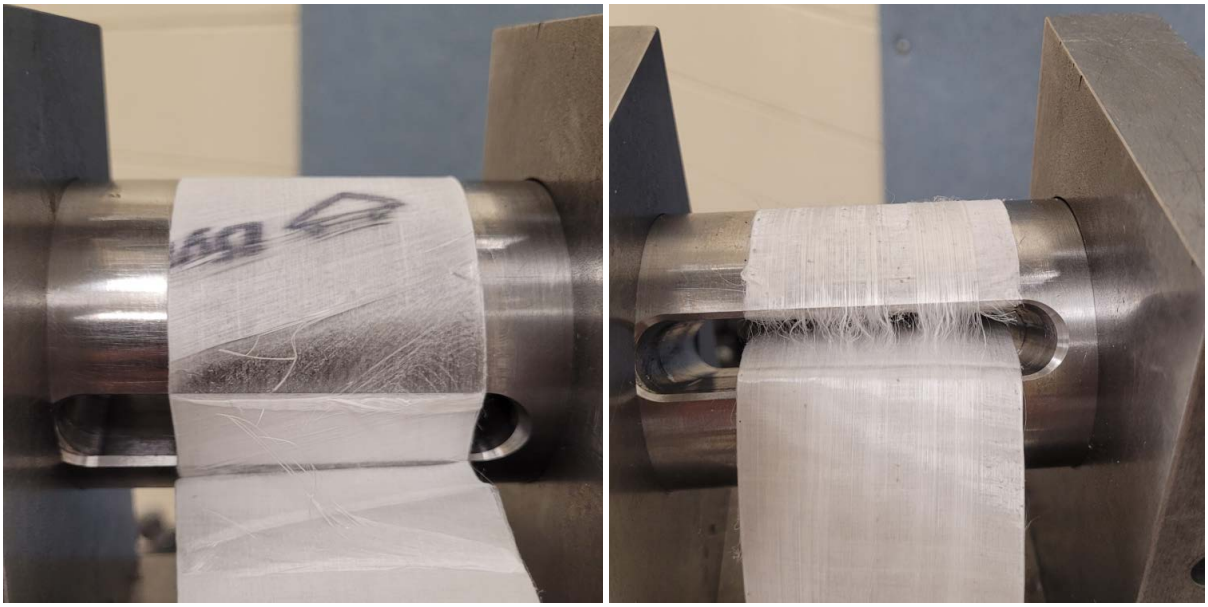

(a) (b)

Figure 4.4: Post tensile test view of mounting (a) 90° face inwards (b) 0° face inwards.

Fiber Angle Effects on Dynamic Mechanical Analysis

Since acquisition of the composite's constituent parts of matrix and fibers or single ply layups was not possible, the fiber angle of coupons was varied to characterize the tensile properties of the matrix. A tensile test with a continuous fiber layup of $[\pm 45]_2$, none of the fibers are undergoing tension and a simulated shearing test is created. This test is designed to characterize the viscoelastic response of matrix and fiber-matrix interface.

Figure 4.5 depicts the failure of a quasi-static tensile test of Spectra 5241 $[\pm 45]_2$ under a displacement rate of 0.1% strain per minute. The $[\pm 45]_2$ coupons begin to neck in the center before failing in shear of the matrix along fiber angle. Necking of the $[\pm 45]_2$ coupon occurs at 22% ±1% strain and ultimate failure through delamination occurs at 44% ±2% strain.

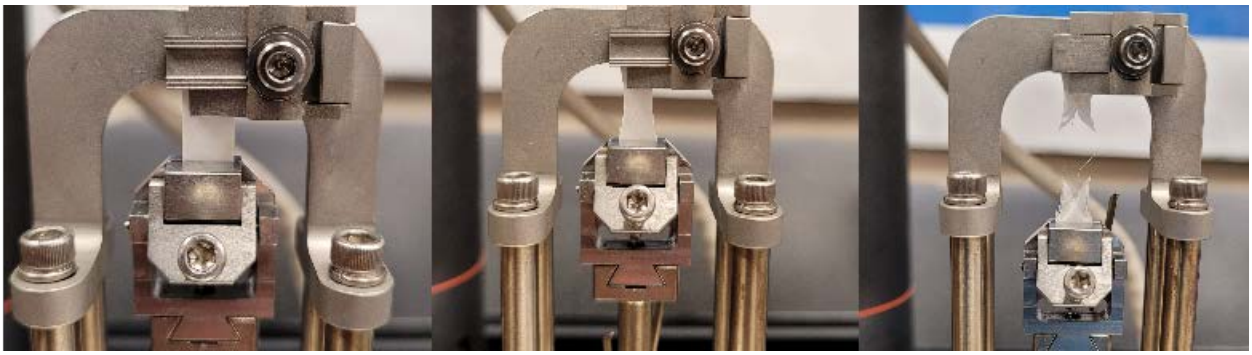

Figure 4.5: Failure progression of a single layer of SR-5241 $[\pm 45]_2$.

Figure 4.6 shows the effect of fiber angle on the storage modulus for temperatures between -50°C to 100°C. The $[0/90]_2$ configuration has a storage modulus four times higher than the $[\pm 45]_2$ at -50°C, as is expected since the fibers are axially loaded in the former layup, but not the latter. The 95% confidence interval is plotted in the shaded area around each line. The storage modulus (E') for both fiber orientations decreases as the temperature rises, which follows convention. As the polymer approaches melting temperatures, it behaves more rubbery and the storage modulus continues to decrease. There is an exception to this behavior for a small window between 18°C and 28°C where the $[0/90]_2$ storage modulus increases by 1 GPa before returning to the downward trend as temperature rises. This testing perturbation could have resulted from the polymer chains and fibers not being fully seated in temperatures below 18°C, and before uniform loading the fibers, which occurred between 18°C to 28°C. The $[\pm 45]_2$ samples demonstrated a consistent decrease in storage modulus for the entire temperature range. The shaded area around both the gold line and blue line are 95% confidence interval for the tests. The gold line represents the $[0/90]_2$ coupons, and the solid blue line represents the $[\pm 45]_2$ samples. The confidence interval of $[0/90]_2$, sample is larger than that of the $[\pm 45]_2$ likely from the variation in the fiber strengths along the composite compared to the variation in the matrix.

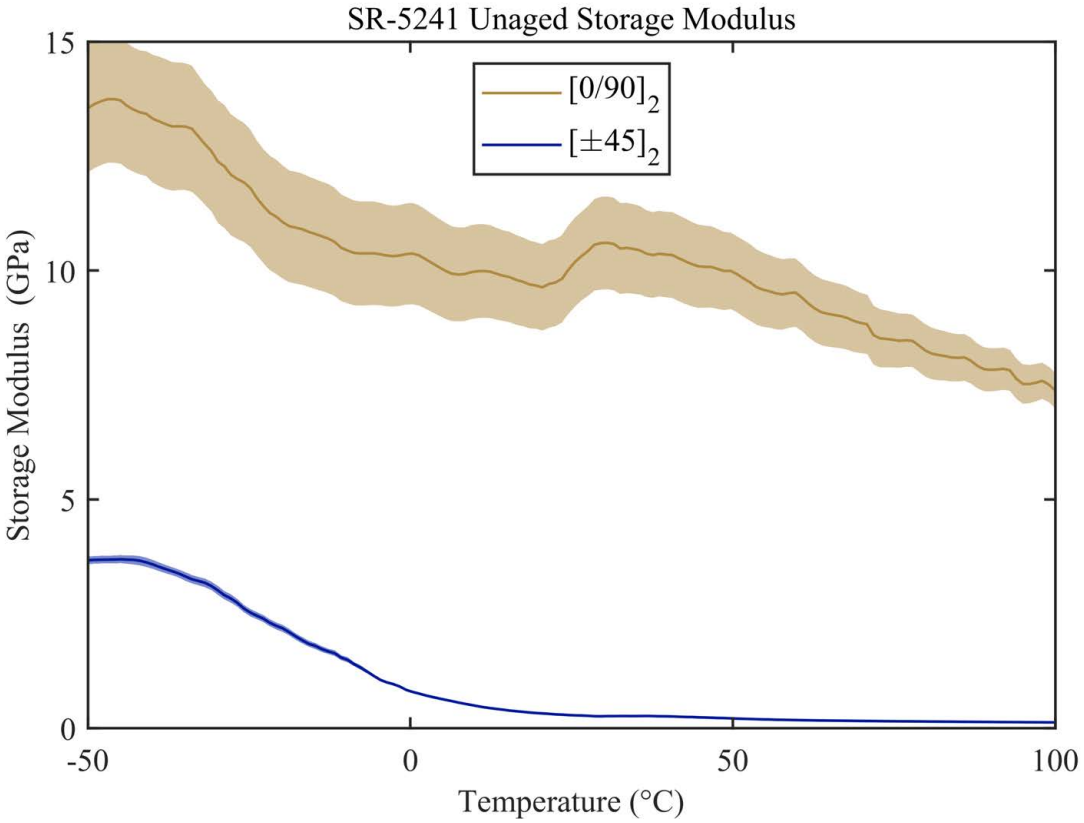

Figure 4.6: Comparison of fiber angle on SR-5241's loss modulus at strain rate of $3x10^{-1}$ (s^{-1}).

Figure 4.7 depicts the loss modulus (E'') versus temperature for both fiber angles. The $[0/90]_2$ has an inflection point at -2°C where the loss modulus increases up to 60°C, before decreasing as temperatures approach 100°C. The $[\pm 45]_2$ coupons exhibit a slight increase in loss modulus for temperatures between -50°C to -30°C, before following the decreasing trend as temperatures increase to 100°C. This suggests the optimal temperatures for dissipating energy for $[0/90]_2$ are between 35°C and 100°C. While the $[\pm 45]_2$ performs best for dissipating energy around -30°C, the magnitude of the loss modulus is lower than the $[0/90]_2$ orientation for all temperatures. There is also a slight increase in the loss modulus at -30°C for the $[0/90]_2$ layup, suggesting that this increase is due to the PUR matrix. As these UHMWPE fibers are stretched during the gel spinning process, molecular weights of chains are formed in a spectrum as well as natural flaws in the fibers which leads to a greater spread in the modulus compared to the $[\pm 45]_2$ test which is dominated by the homogeneous matrix.

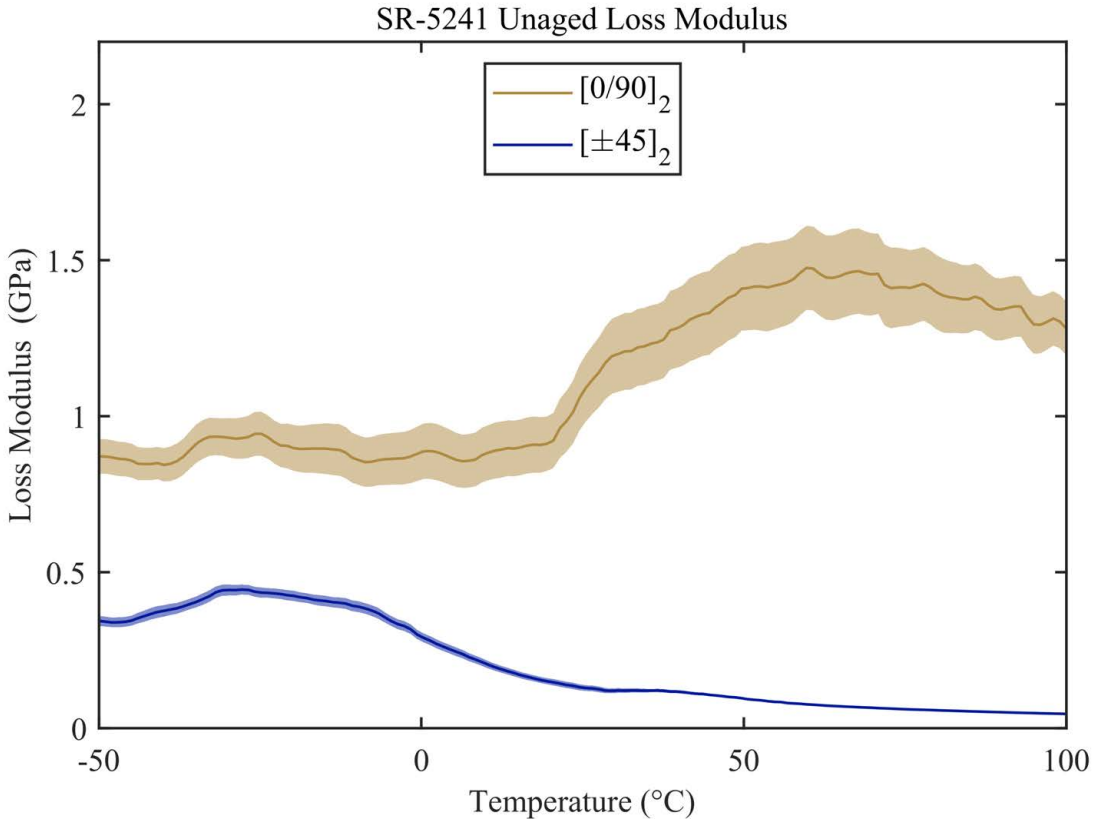

Figure 4.7: Comparison of fiber angle on SR-5241's loss modulus at strain rate of $3x10^{-1}$ (s^{-1}).

Figure 4.8 shows the tan δ for both fiber angles over temperature. While the $[\pm 45]_2$ tan δ is greater than the $[0/90]_2$ tan δ for all temperatures reported in Figure 4.8, this does not mean that the $[\pm 45]_2$ is stronger, only that the relative ability for the material to dampen energy is greater than the $[0/90]_2$ layup. The ability for both fiber orientations to dampen energy increases with temperature, except for the $[\pm 45]_2$, which peaks at 28°C before decreasing slightly as temperatures increase to 100°C.

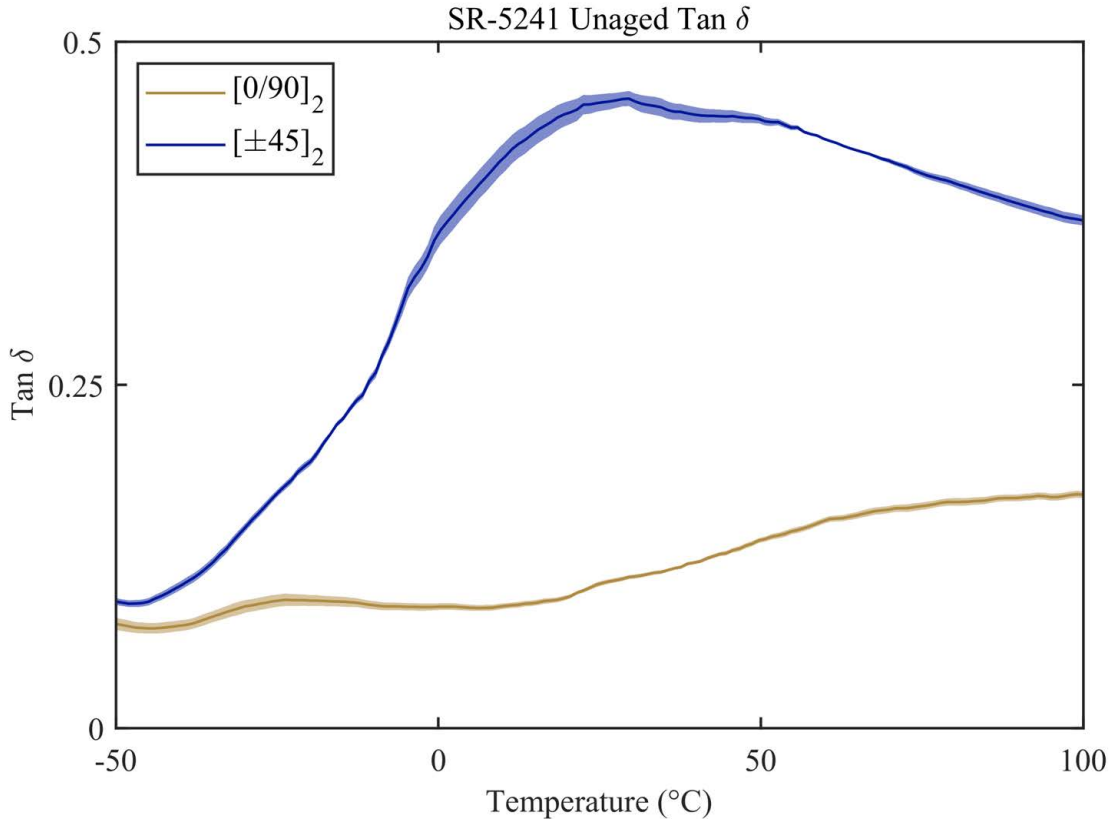

Figure 4.8: Comparison of fiber angle on the tan δ response of SR-5241.

Table 4.3 shows the effect of strain rate on the viscoelastic response of $[0/90]_2$ and $[\pm 45]_2$ layups. As strain rate increases, the storage and loss moduli also increase.

Table 4.3: SR-5241 Viscoelastic Tensile Properties at 30°C

Strain Rate (s^{-1})	Storage Modulus (GPa)		Loss Modulus (GPa)	
	$[0/90]_2$	$[\pm 45]_2$	$[0/90]_2$	$[\pm 45]_2$
$2x10^{-2}$	12	$9x10^{-2}$	2.6	$4x10^{-2}$
$4x10^{-1}$	19	$1.5x10^{-1}$	3.3	$7x10^{-2}$
$1x10^{0}$	20	$2x10^{-1}$	3.7	$8x10^{-2}$

A viscoelastic material parameter characterization of two fiber angles $[0/90]_2$ and $[\pm 45]_2$ of a single prepreg laminate of SR-5241 was conducted while remaining in the linear elastic zone of the material. This study demonstrated that the majority of the dampening and dissipation of energy comes from the UHMWPE fibers for the operational temperatures and not the matrix. However, the matrix is still crucial to functionality of the composite.

WATER AGING RESULTS AND DISCUSSION

Water has a deleterious effect on polymer composites, however the manufactures of these UHMWPE materials claim this material does not absorb water. As these composites are used in areas that experience high humidity or even total submersion it is important to understand how these composites age with water. This chapter details the results of water aging from experiments introduced in Chapter 3, and provides a commentary on how these composites responded to aging.

UHMWPE composites both as single layer and in 95 layer pressed panel form were aged at room temperature by soaking in simulated sea water, herein referred to as salt water, and distilled water according to ASTM D-1141-52. The weight increase from water absorption was measured periodically over the 669 day test. Single layer UHMWPE samples were observed under a scanning electron microscope for changes in surface morphology after water submersion. The single layer samples that survived the water aging were interrogated via dynamic mechanical analysis.

Pressed Panel Aging

95 layer pressed panel HB-212 coupons were soaked in jars filled with salt water and distilled water for 669 days. After 129 days, the pressed panels began to show biological growth in the form of black splotches between plys. Figure 5.1 shows the beginning stages of fungal growth on the consolidated coupons in the salt water aging study.

Figure 5.1: Beginning stages of fungal growth on HB-212 salt water pressed panels.

The fungal growth continued throughout the aging as shown in Figure 5.2, which warranted further investigation. A study on fungal growth was conducted by NTS labs to investigate the susceptibility of these composites to biological growth.

Figure 5.2: Interlaminar fungal growth after 669 days in salt water.

Figure 5.3 shows the distilled water aged samples had an orange tint from the stainless steel cage corroding during the 669 day submersion. This is not likely due to biological

growth.

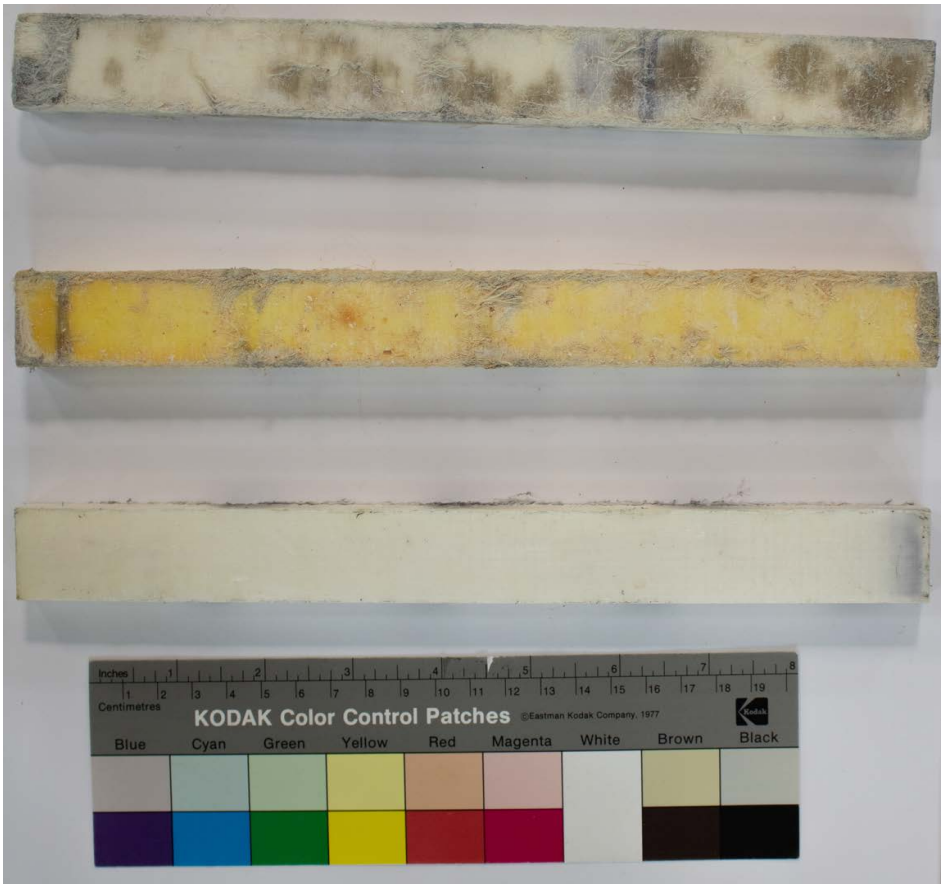

Figure 5.3: 95 layer pressed panel HB-212 samples from top to bottom: salt water, distilled water, and unaged.

This fungal growth only appeared in the pressed panels that were waterjet cut and aged in salt water. There are two main theories for the growth. One is contamination from manufacturing like oil from fingerprints during layup at ITEN defense. The second form of contamination is from the waterjetting processes where the abrasive and other contaminates can travel between plys, creating gaps, which led to fungal growth areas. This growth occurred despite manufactures claiming that this material is not susceptible to fungus.

NTS was contracted to expose the UHMWPE composites to fungal growth. These tests were conducted according to MIL-STD 810G and MIL-STD 810H, which give the fungus

the most ideal conditions to grow. There appeared to be a small amount of fungal growth on the ends of a few delaminated fibers as seen in Figure 5.4.

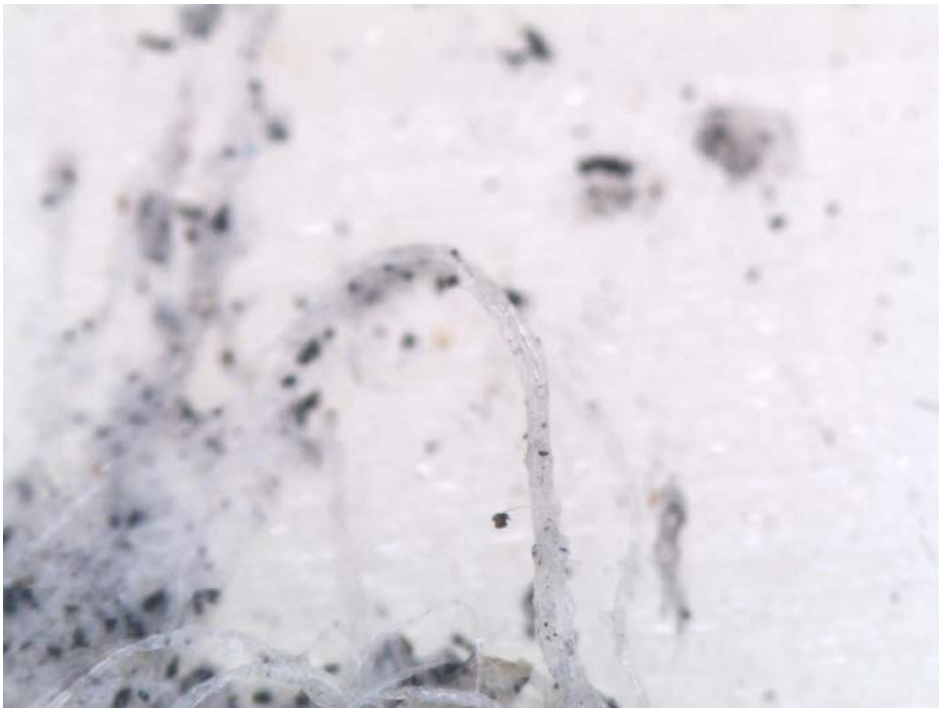

Figure 5.4: Trace growth on frayed edge likely due to contamination from cutting, 28 days after fungal inoculation.

This amount of growth is next to nothing compared to the control samples after 7 days as seen in Figure 5.5.

Figure 5.5: NTS control samples 7 days after inoculation.

Figure 5.6 depicts those same control samples after 28 days.

Figure 5.6: NTS control samples 28 days after inoculation.

According to evaluation criteria in MIL-STD-810H there is no growth on any of the UHMWPE samples after 28 days on the 95 layer pressed panel.

The weight was periodically measured to determine the diffusion of water into the samples over time. The average weight increase from water uptake for the 95 layer pressed panel samples of HB-212 is shown in Figure 5.7. Both the salt water and distilled water soaked 95 layer HB-212 pressed panel coupons remained buoyant after 669 days.

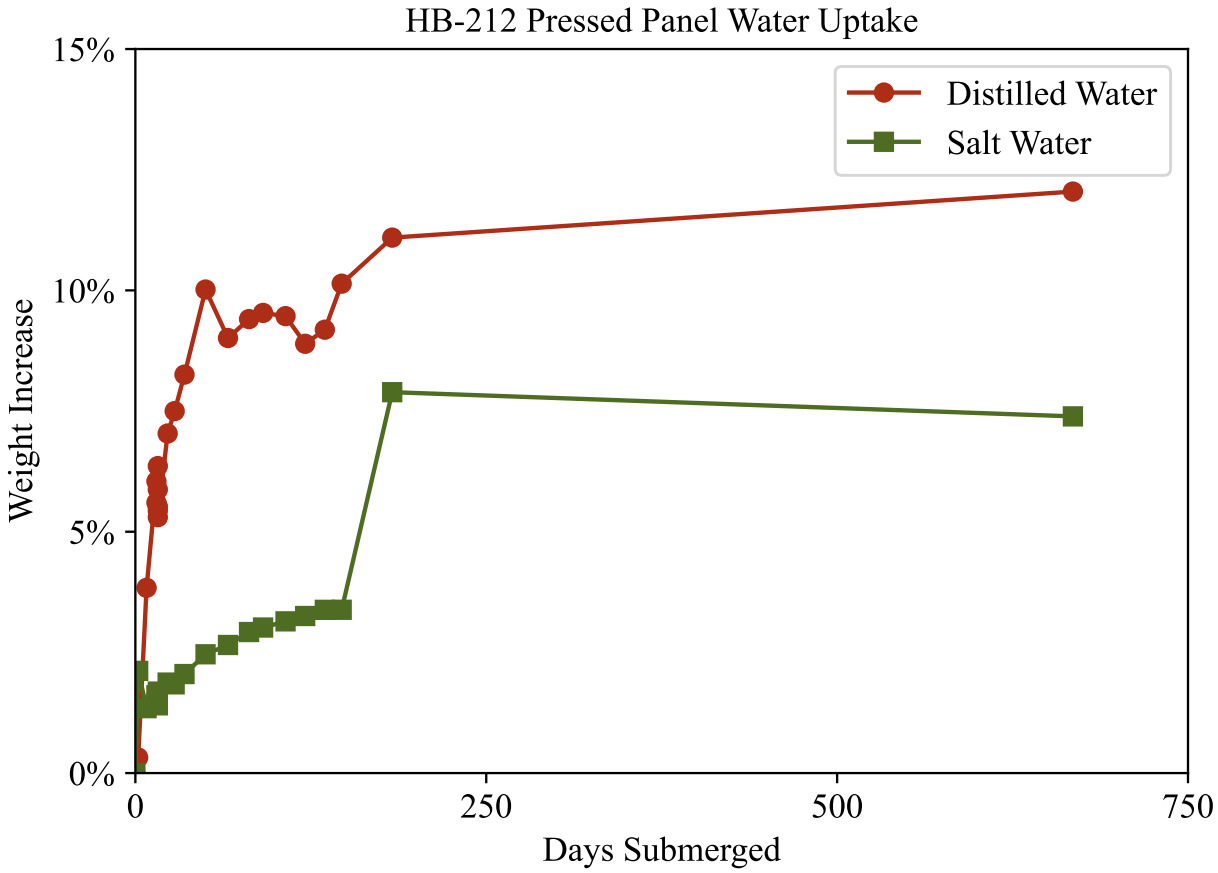

Figure 5.7: Average water uptake for 95 layer HB-212 water jet cut panels at 20°C.

The distilled water uptake increased the average weight of five coupons by 12%, while the salt water aged coupons increased by only 7% over the 669 day test. While the salt water can deposit salt crystals on the surface of the composite, potentially adding to the weight, the distilled water creates an environment that ages the matrix faster. As the distilled water has less total dissolved solids, the water has a higher ability to leach synthetic rubber matrix from the composite. The degradation of the matrix creates voids for the water to fill which increases the weight of the composite through this hydrolysis reaction faster than salt water.

Single Layer Aging

Single layer HB-210, HB-212, and SR-5241 were aged in separate jars of salt water and distilled water. At 37 days, both the HB-210 and HB-212 distilled water samples sank to the bottom of the jar. After 49 days, the HB-212 single layer samples in the salt water appeared neutrally buoyant, while the HB-210 in the salt water remained buoyant. There was a white powder precipitate that collected on the bottom the jars. The distilled water jars had a slightly thicker layer than the salt water jar. The stainless mesh had a thin mucus-looking deposit that formed in both salt water and distilled water containers. Figure 5.8 shows the (a) unaged and (b) 50 day aged HB-210 in distilled water. At the end of the 669 day test the HB-210 salt water aged samples still floated.

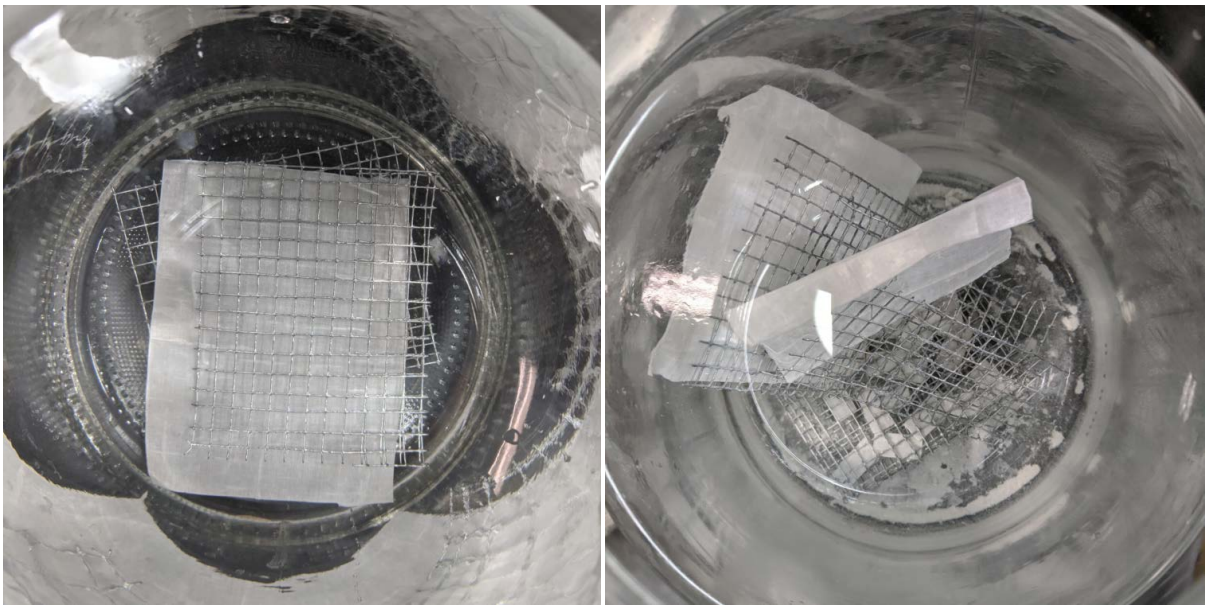

Figure 5.8: Aging in distilled water: (a) day 1 (b) day 50 with matrix collecting at base of jar.

The distilled water collected more white sediment at the bottom of soaking aging jars

compared to the salt water aged samples. Figure 5.10 shows corrosion products depositing onto the surface of the HB-212 distilled water samples, along with a large amount of white sediment on the bottom of the jar. This sediment is evidence of hydrolysis of the matrix. As the distilled water has less total dissolved solids compared to the salt water, there is a higher potential for matrix dissolution. The distilled water has fewer ions and therefore a lower state of entropy, which accelerated the aging process. While the presence of salt water can accelerate the corrosion process as the salt ions facilitate the movement of electrons, the higher solvency power of distilled water causes the corrosion of the matrix to occur at a faster rate.

At the end of the 669 days, the HB-210 salt water samples were the only single layer samples floating. This is likely due to the slower rate of matrix dissolution and the higher density of the salt water combined with the PUR matrix being less reactive with the water compared to the Kraton® rubber.

Single layer HB-210 and HB-212 were aged in distilled water for 669 days. The average increase in weight for the single layer HB-210 and HB-212 is shown in Figure 5.9.

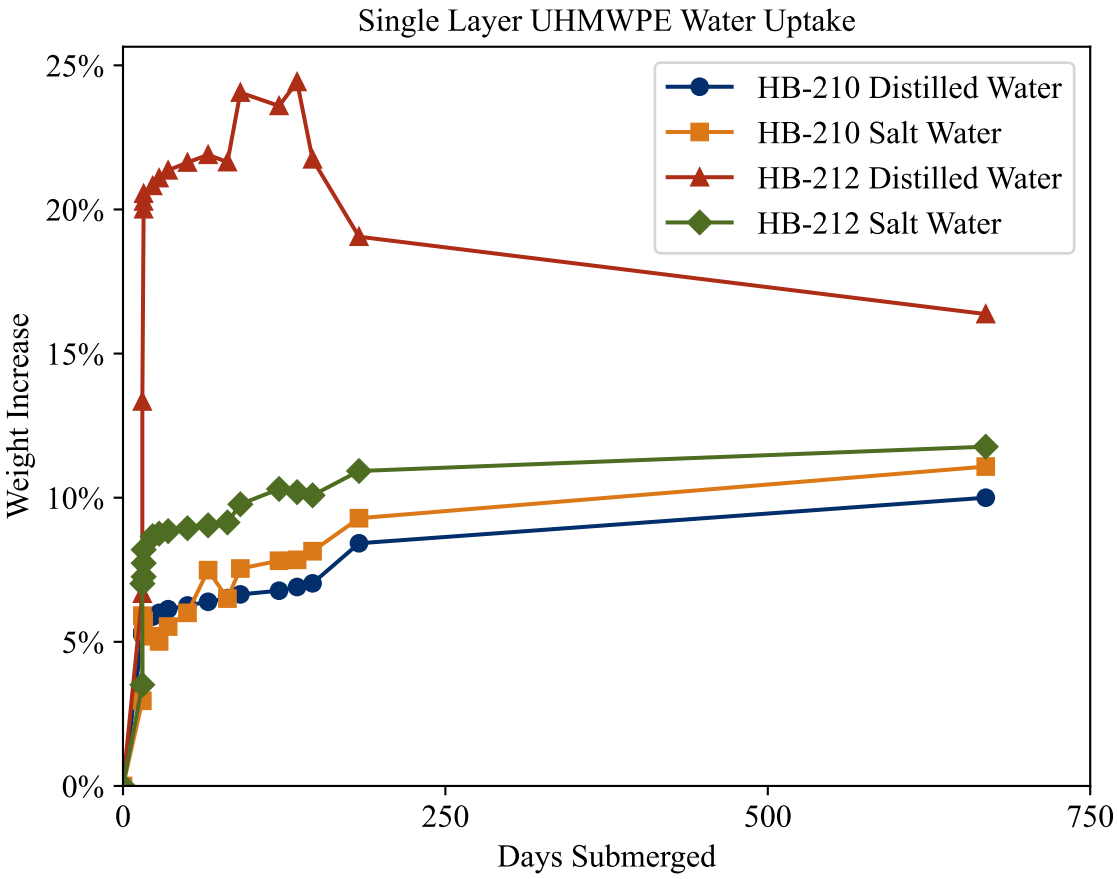

Figure 5.9: Average water uptake for single layer UHMWPE composites at 20°C.

The single HB-212 samples soaked in saltwater exhibit a higher average percentage increase in weight breaking from the trend established in the pressed ply's. This is attributed to the corrosion of the stainless steel cage within the solution, which subsequently deposited some of this oxidation onto the samples, as depicted in Figure 5.10.

Figure 5.10: Oxidation of stainless steel cage on HB-212 in distilled water with matrix material covering bottom of jar.

The single layer samples were also tested for fungal growth at NTS according to MIL-STD 810H. Figure 5.11 is a sample of SR-5241 at 28 days with a bit of fungal growth on the edge fibrils, likely from contamination after cutting. The single layer HB-210 and HB-212 samples showed no growth after 28 days. The full report following MIL-STD 810H for fungal testing conducted by NTS is in Appendix A.

Figure 5.11: Trace fungal growth, 28 days after fungal inoculation on single layer SR-5241.

The single layer HB-212 aged samples appeared delaminated and had significant fraying and fiber pull out as the matrix appeared to have significant hydrolysis and dissolution into both the salt water and distilled water. As such, these samples were unable to evaluated using dynamic mechanical analysis. Only the HB-210 single layer samples were able to be tested through dynamic mechanical analysis.

Figure 5.12 illustrates a slight decrease in storage modulus over temperature for the single layer HB-210 coupons after 669 days of water submersion. The error bars, representing the 95% confidence interval for the tests, are displayed every 40°C for clarity and readability. Comparatively, the salt water aged samples demonstrate a slightly higher storage modulus across the temperature range compared to those aged in distilled water.

The impact of distilled water on the storage modulus of the single-layer composite is attributed to matrix dissolution and potential chain scission of the fibers, occurring at a

higher rate than in salt water. Notably, the salt water aged samples exhibit a slight increase in storage modulus from 5°C to 40°C, possibly due to an averaging error from a small sample set. It is expected that as the number of tested coupons increases, this error will decrease. However, as the polymers approach the melting temperature, the ability of this composite to respond elastically is anticipated to decrease.

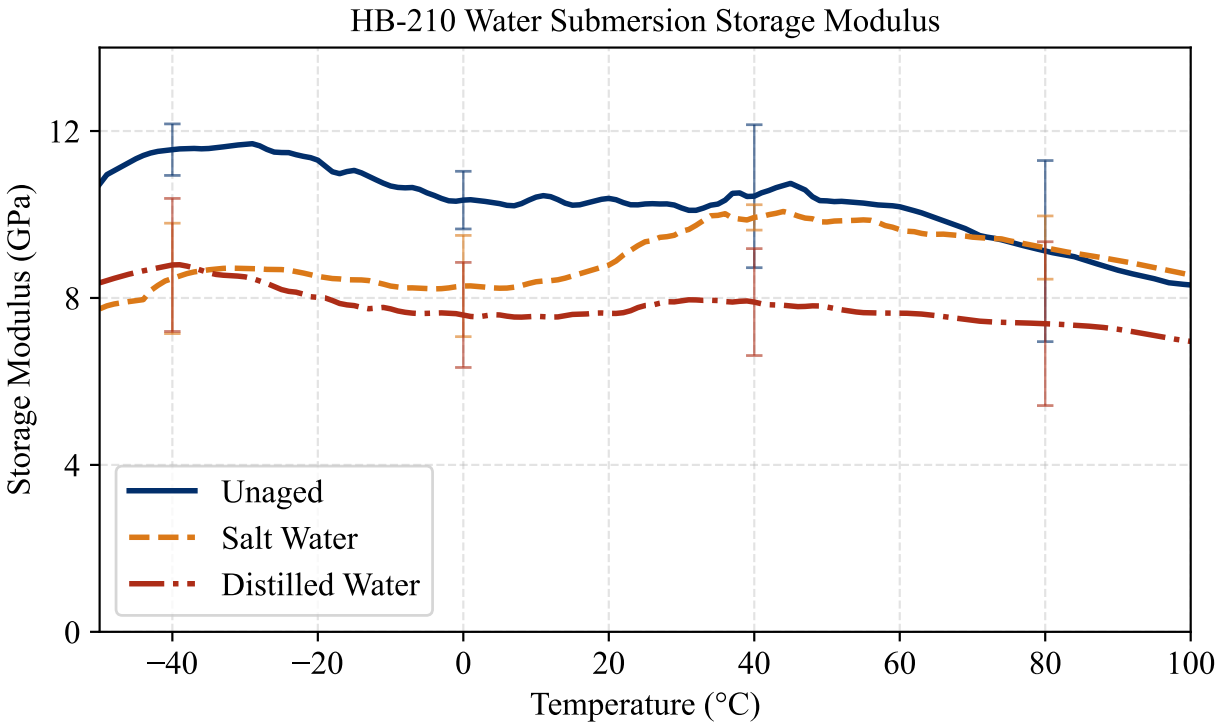

Figure 5.12: HB-210 storage modulus from DMA with a temperature ramp and single strain rate $4x10^{-3}$ (s^{-1}).

Figure 5.13 depicts the slight increase in loss modulus over temperature of the water submerged HB-210 single layer samples. The confidence interval for the unaged samples is higher for the storage modulus compared to the salt water and distilled water aged samples, due to the small sample size. With more testing, the average unaged loss modulus is expected to increase. The salt water aged samples outperform the distilled water through a higher loss modulus, meaning the composite retains more ability to dissipate energy.

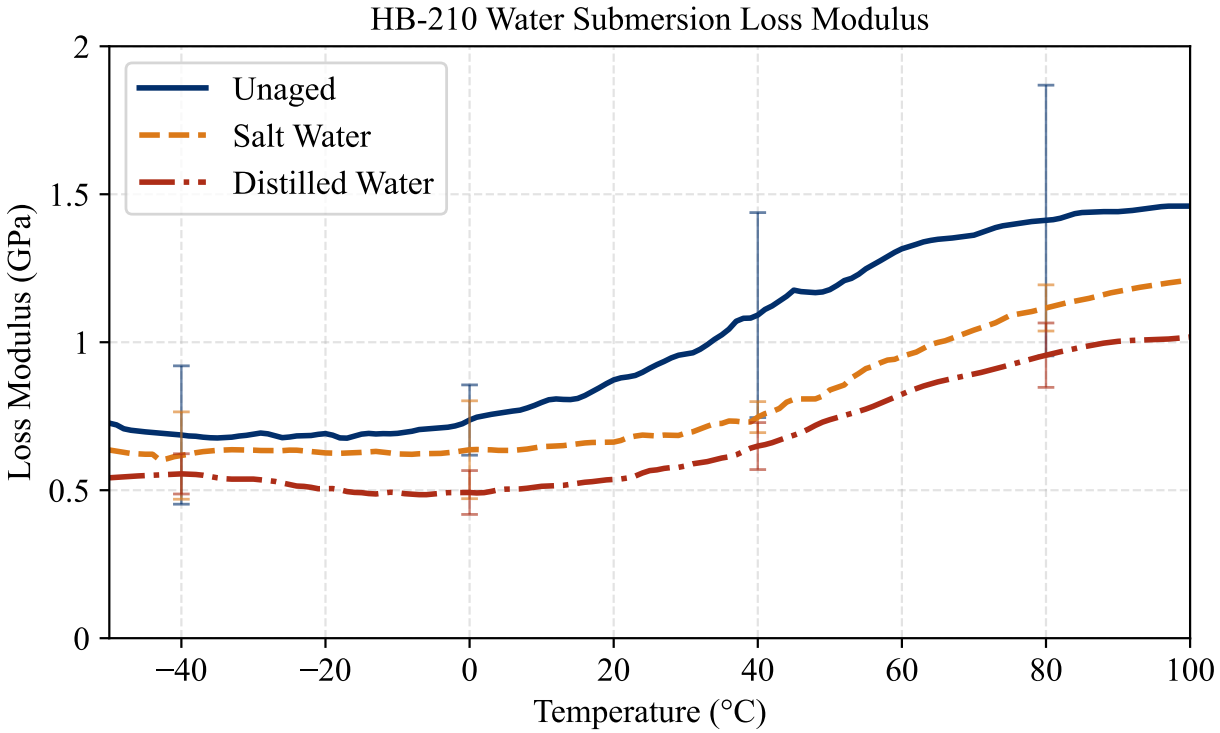

Figure 5.13: HB-210 loss modulus from DMA with a temperature ramp and single strain rate = $4x10^{-3}$ (s^{-1}).

The trend continues at 30°C as the strain rate increases. Figure 5.14 is the storage modulus over strain rate for HB-210 with the number of tests 'n' in the legend. The storage modulus is reduced by half with submersion. The distilled water reduces the storage modulus response slightly more than the salt water aging.

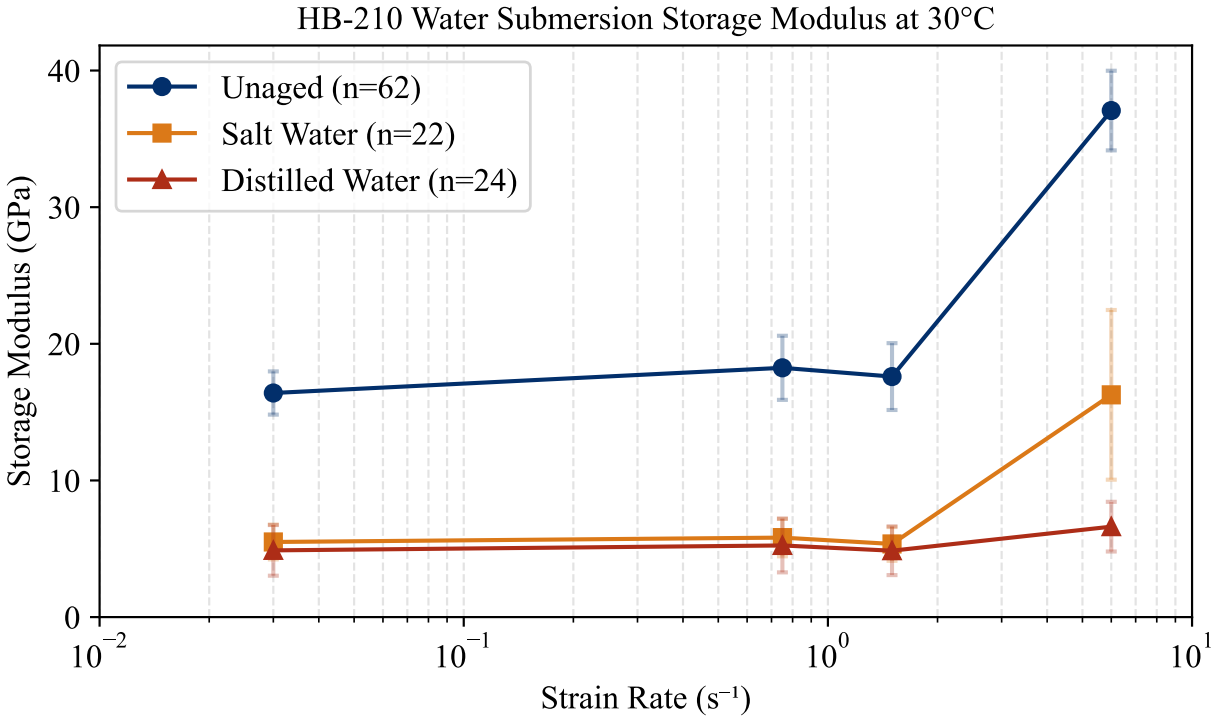

Figure 5.14: Storage modulus of HB-210 during isothermal (30°C) strain rate ramp .

Figure 5.15 is the loss modulus response of HB-210. Similar to the storage modulus, the viscous component also decreases with soaking age. The distilled water decreased the loss modulus greater than the salt water. As strain rate increases, both the viscous and elastic component of the modulus increases.

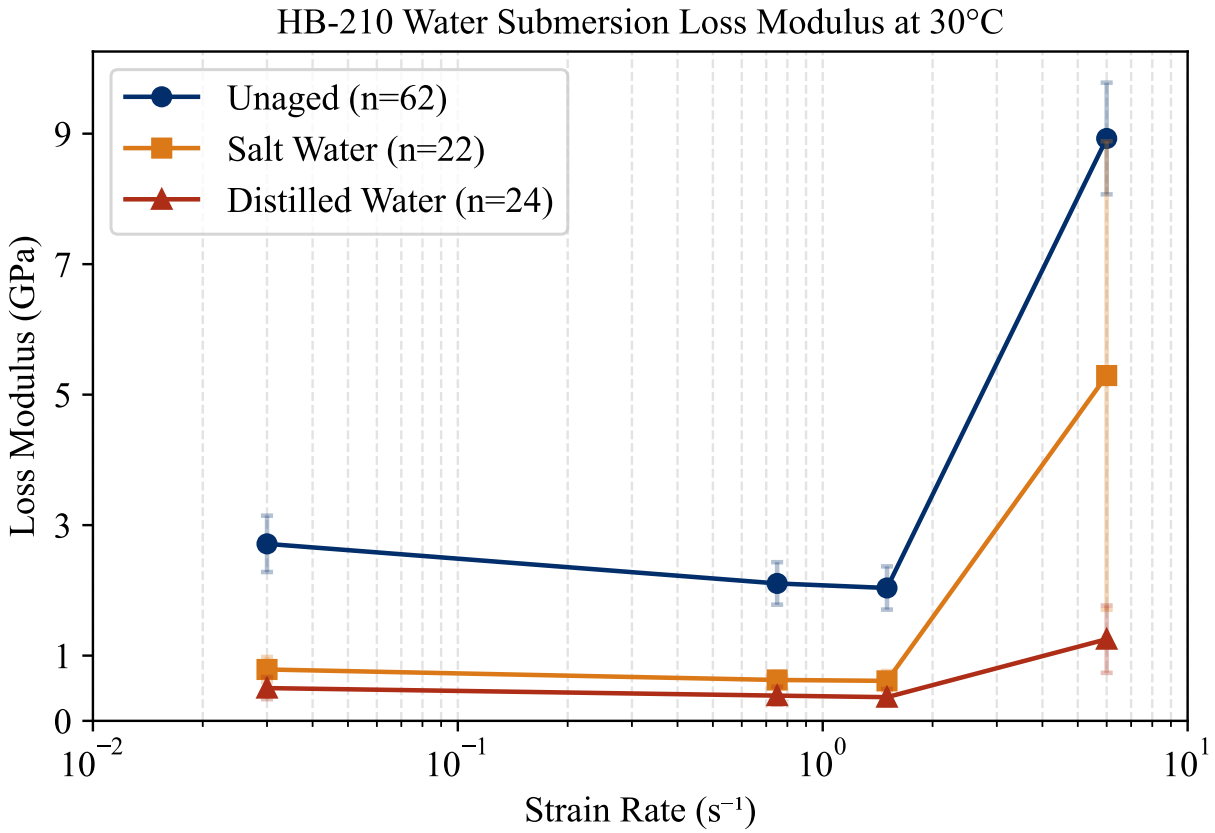

Figure 5.15: Loss modulus of HB-210 during isothermal 30°C strain rate ramp.

The single layer UHMWPE fiber reinforced composites were imaged using a field emission scanning election microscope (SEM). The surface morphology of these samples changed during submersion, lending insight into how the composite aged in salt water and distilled water. The SEM images of unaged HB-210 and HB-212 samples are shown in Figure 5.16. Figure 5.16 (a) shows the unaged HB-210 with a thick layer of polyurethane matrix covering the fibers with a few visible holes in the matrix where UHMWPE fibers are exposed. These holes are from manufacturing defects and are potential sites for hydrolysis reactions to concentrate. Figure 5.16 (b) is the unaged HB-212 which has on average less matrix covering on compared to the HB-210.

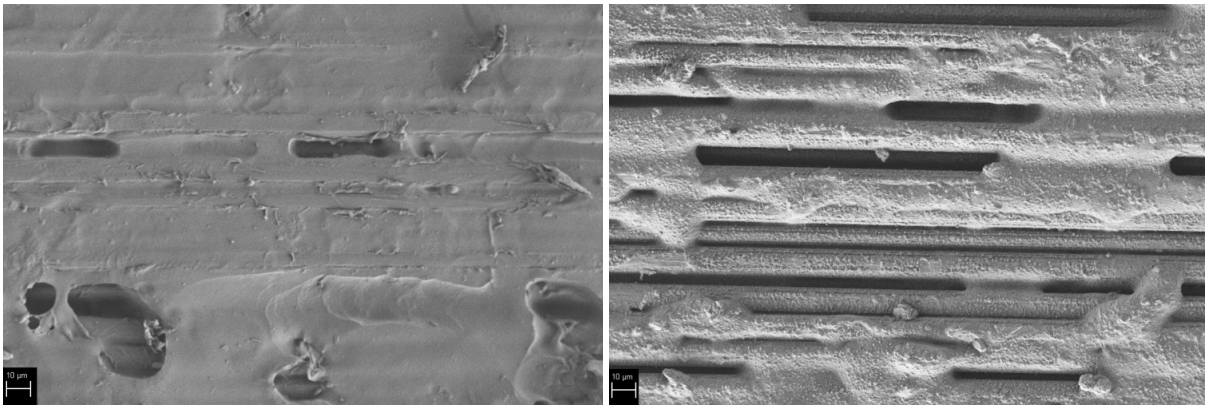

Figure 5.16: SEM image of unaged (a) HB-210 and (b) HB-212.

Figure 5.17 shows the distilled water aged samples for (a) HB-210 and (b) HB-212, exhibiting a few holes in the center of the matrix. The matrix coverage appears to be reduced compared to the unaged sample, from matrix dissolution into water as evidenced by the white power collecting at the bottom of the jars. The surface of the matrix appears rougher than the unaged sample.

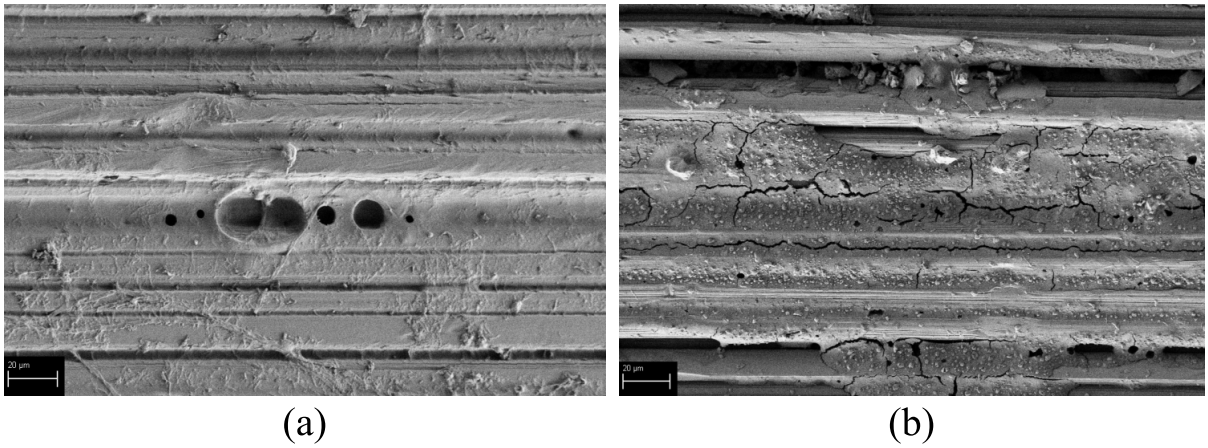

Figure 5.17: SEM image of (a) HB-210 and (b) HB-212 aged in distilled water.

Figure 5.18 presents the UHMWPE fiber reinforced composites (a) HB-210 and (b)

HB-212 after aging in salt water. Both types of UHMWPE composites have small amounts of salt crystals deposited on the surface. The HB-212 has less matrix coverage than the HB-210 as seen in both the SEM images and optically after submersion.

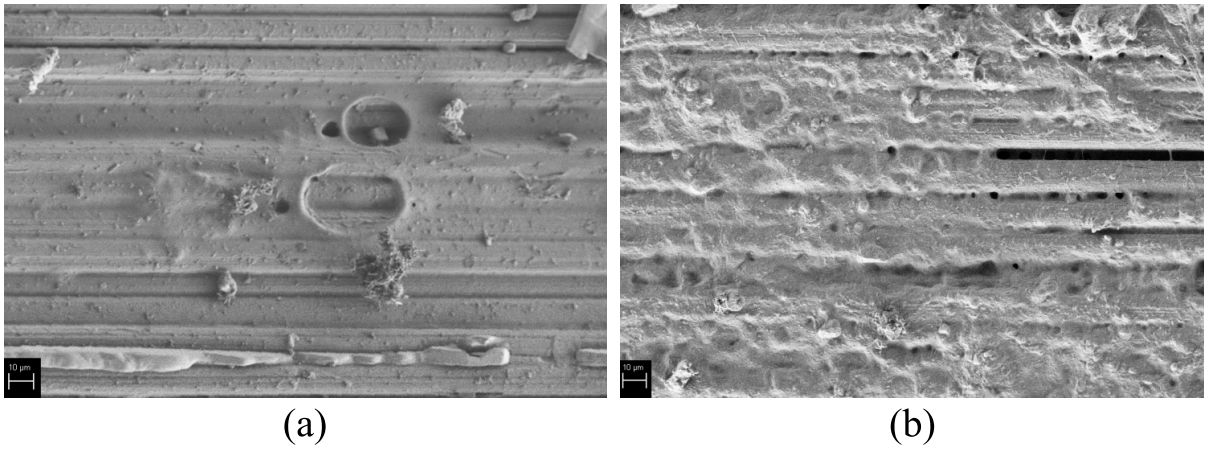

Figure 5.18: SEM image of (a) HB-210 and (b) HB-212 aged in salt water.

Comparing Figure 5.17 and Figure 5.18, there is less overall matrix coverage on the surface of the distilled water compared to the salt water aged samples.

Figure 5.19 provides an enlarged SEM image of the unaged HB-210 matrix void. It shows two full fibers and the top portion of a third fiber in a horizontal configuration, with the matrix surrounding them on the superior aspect and right side of the image. Striations on the fiber, potentially from the gel-spinning process, are visible. The smaller aggregates on the fibers are iridium residues from the SEM imaging process.

Figure 5.19: Enlarged SEM view of unaged HB-210 with matrix voids exposing fibers on the surface.

Figure 5.20 presents an enlarged SEM image of a HB-210 sample aged in distilled water. The surface morphology reveals contaminants resembling tiny fibers visible on the upper surface of the remaining matrix between fibers.

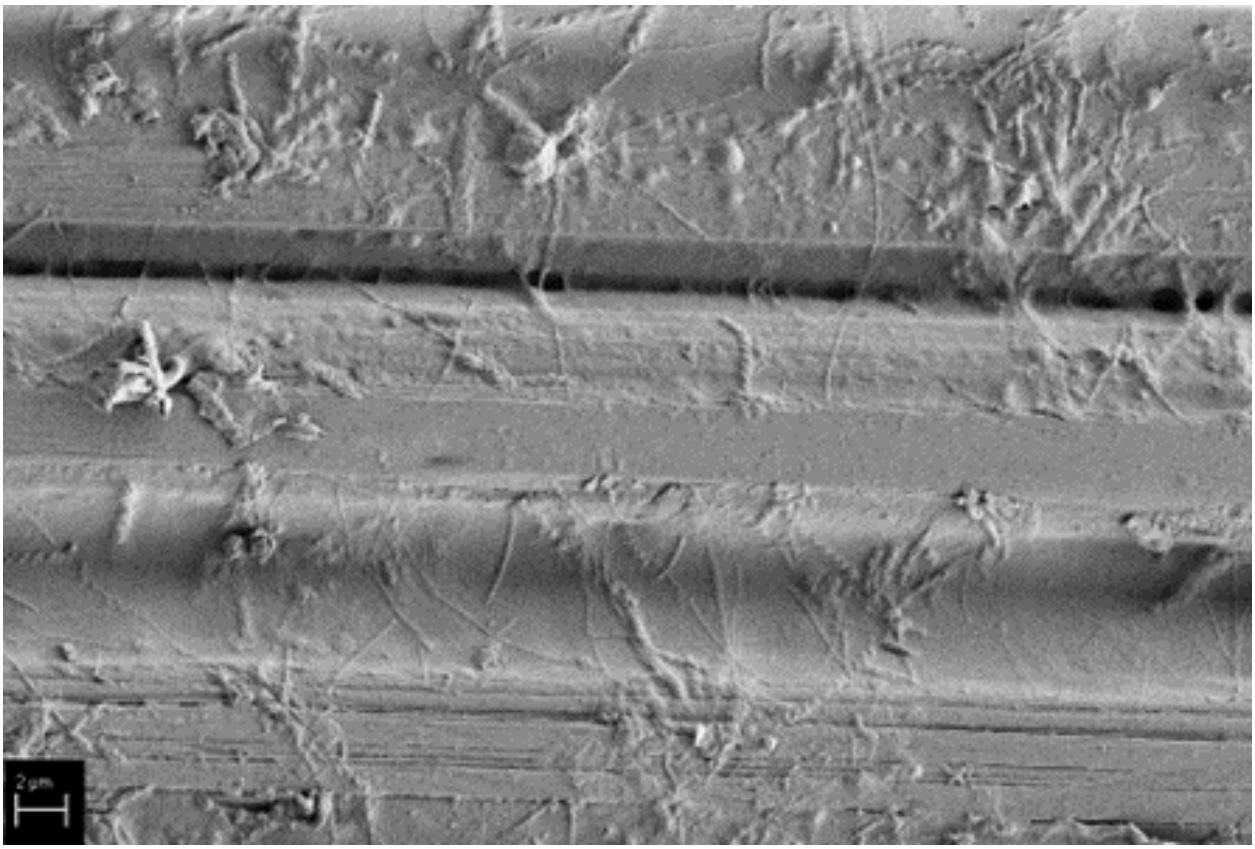

Figure 5.20: Enlarged view of a SEM image of HB-210 aged in distilled water.

Figure 5.21 provides a closer view of the HB-210 salt water aged sample, showing salt crystal growth on the surface, confirmed by EDX. The SEM image also reveals slight matrix cracking due to saltwater exposure, indicating a potential hydrolysis process. Several groups of highly crystalline objects are distinguishable, which are absent in the unaged and distilled water aged HB-210 samples. The small circular and elliptical drops on top of the matrix are iridium sputtering residues apparent throughout the image.

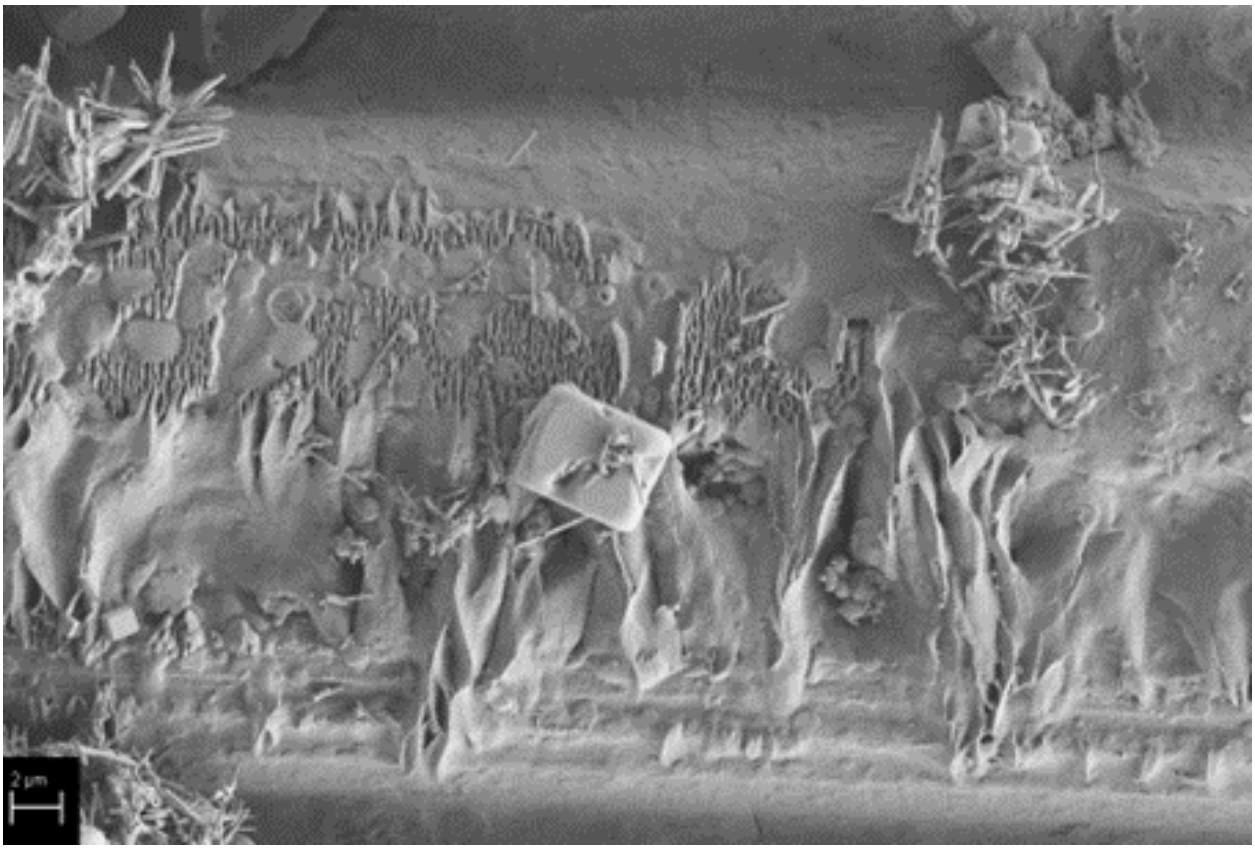

Figure 5.21: Enlarged SEM view of HB-210 aged in salt water showing crystal deposits on surface.

These experiments show that water aging, particularly in distilled water, significantly impacts the physical and mechanical properties of UHMWPE composites. Despite manufacturer claims, these materials are susceptible to hydrolysis, fungal growth under certain conditions, and mechanical property changes over prolonged exposure to water. The findings highlight the importance of considering environmental aging factors in the application and development of UHMWPE fiber reinforced composites.

ULTRA-VIOLET AGING RESULTS AND DISCUSSION

UHMWPE fiber reinforced composites were aged according to the procedure in Chapter 3. To understand the effect of Ultra Violet (UV) aging on UHMWPE composites, optical and dynamic mechanical analysis observations are presented in this chapter. As the UV aging involves the presence of both humidity and temperature cycling, studies on these separate effects are detailed in Chapter 3 as well.

Optical and Kinetic Observations

The UV aging test created optical and kinetic changes in the UHMWPE composites after aging. The effect of UV caused these composites to become brittle with time. The rubber matrix was altered to a greater degree than the PUR matrix.

Figure 6.1 shows how UV changes the rubber matrix in HB-212's color from white to yellow to brown. The 400 hour and 600 hour samples have the laser scoring marks for DMA samples. As stated earlier these were not used due to the edge effects dominating the DMA tests. The HB-210's PUR matrix did not have the same yellowing effect, but rather changed opacity ever so slightly. The camera was not able to detect the changes in the HB-210 and as such is not pictured here.

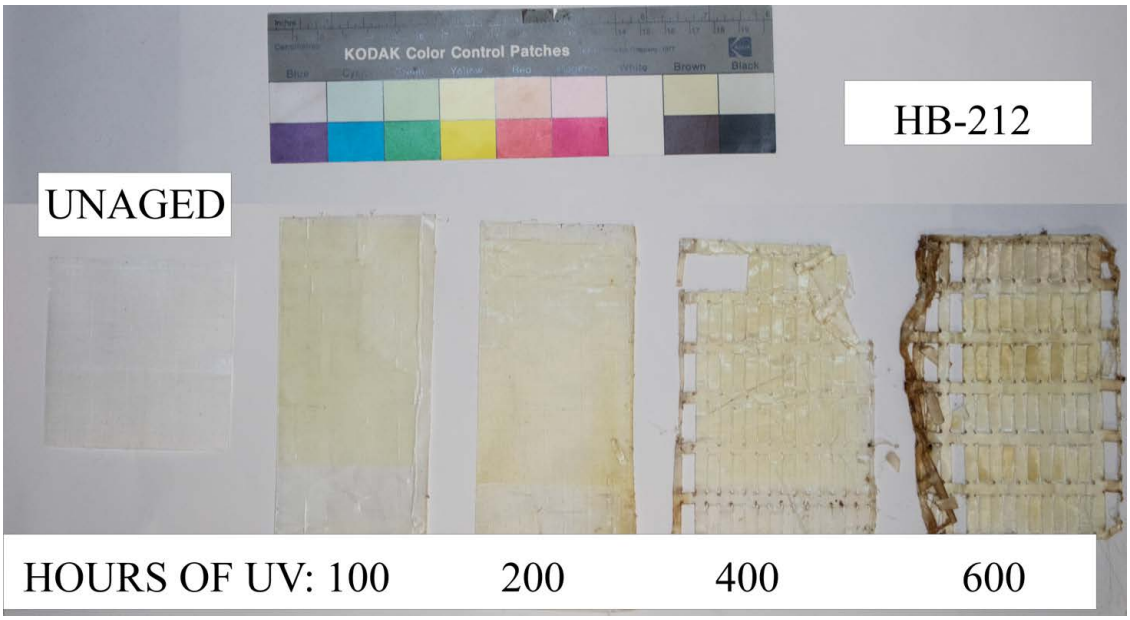

Figure 6.1: Color change from UV exposure in HB-212.

However, Figure 6.2 is the HB-210 and HB-212 after 800 hours of the UV test where the color is back to white because the matrix has fully disintegrated in the window exposed to UV-A light. The result is bare fibers in the UV bulb exposure window highlighted with black in Figure 6.3.

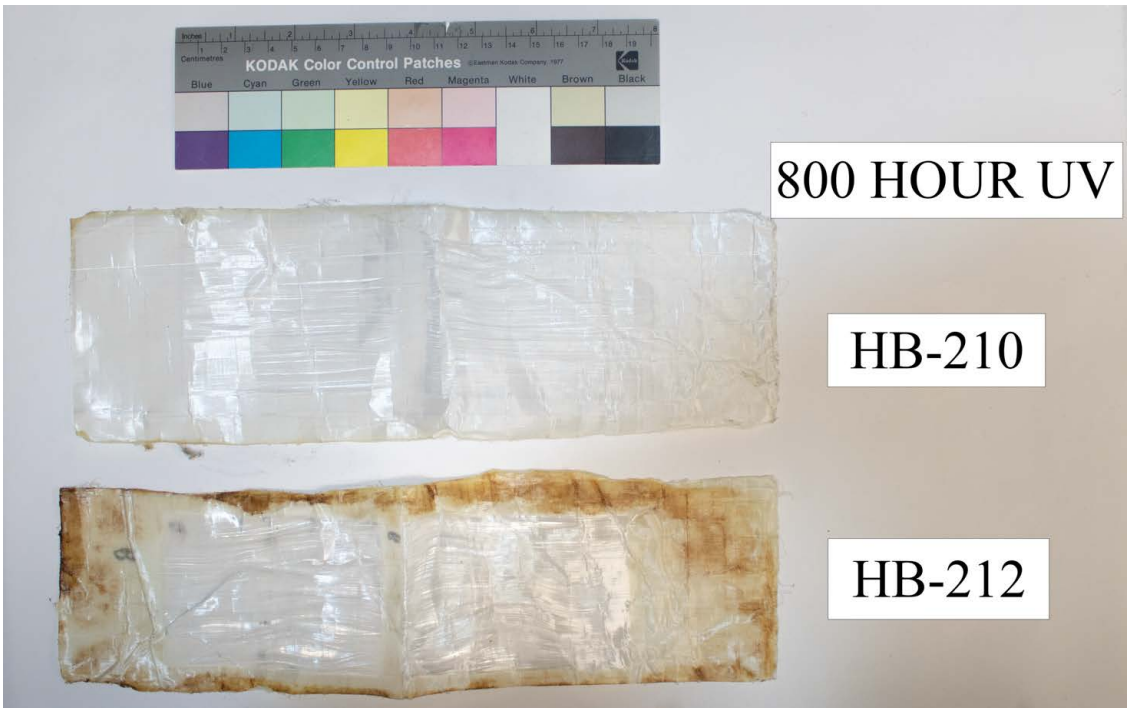

Figure 6.2: UV aging of HB-210 and HB-212 after 800 hours.

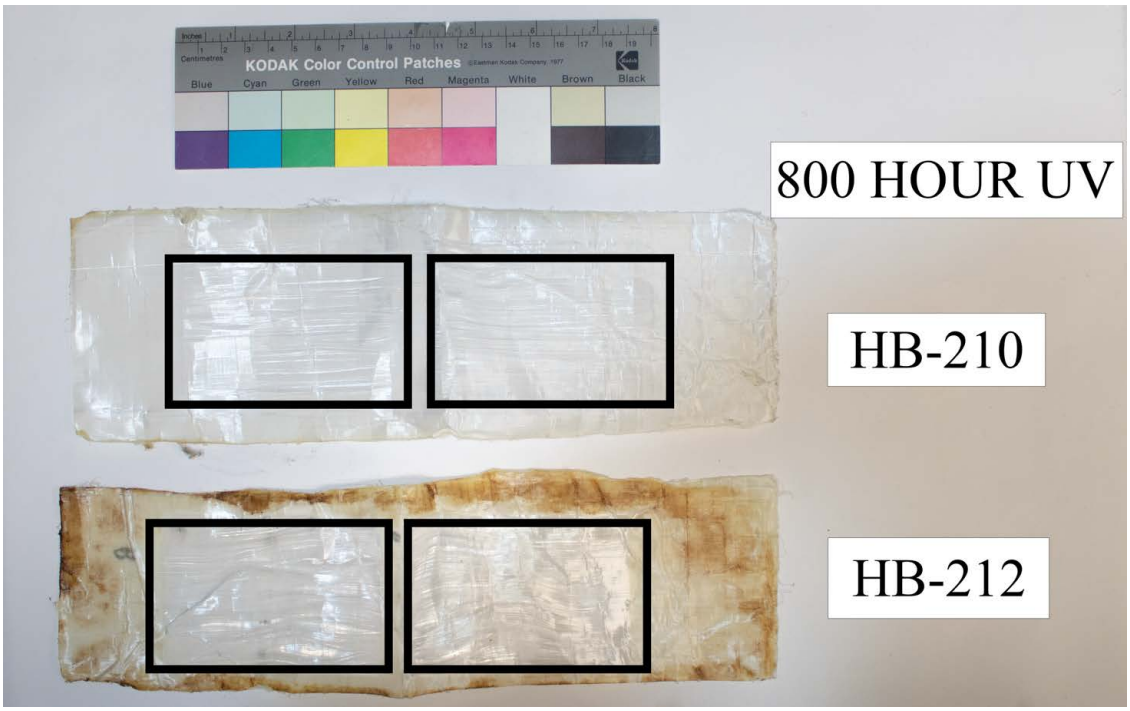

Figure 6.3: Bare fibers exposed in the UV window highlighted black after 800 hours exposure.

SEM

Scanning electron microscopy (SEM) gives more insight into the optical changes of this material. Figure 6.4 contrasts the unaged (a) HB-210 with the PUR matrix to (b) HB-212 with the synthetic rubber based matrix. In Figure 6.4 (a) shows the uniform and thick coverage of the PUR matrix on the surface of the composite. Figure 6.4 (b) shows a section of the UHMWPE fiber reinforced composite with a 0° fiber bundle missing in the center, revealing the 90° ply beneath.

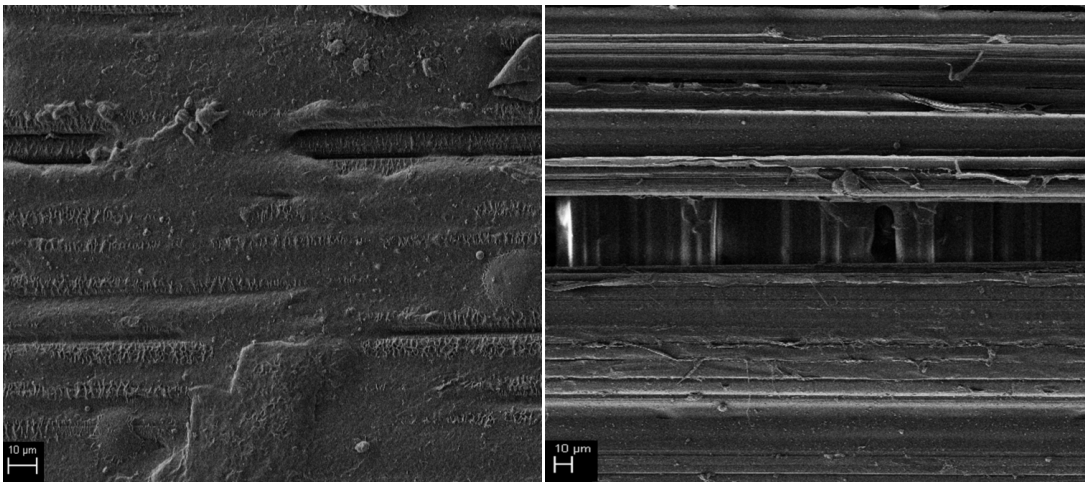

(a) (b)

Figure 6.4: Comparison of unaged (a) HB-210 (b) HB-212.

After 100 hours of UV aging the matrix material's in both composite systems began to degrade. Figure 6.5 (a) shows the PUR matrix appearing to flow down like it is melting. The PUR matrix coverage is similar to the unaged still. After 100 hours the HB-212 matrix became brittle and began to yellow as shown in Figure 6.1, which weakens the matrix-fiber interface. During mounting of the sample onto the carbon tape for SEM imaging, the fibers pulled out, leaving behind a brittle matrix as seen in Figure 6.5 (b). The embrittlement is likely from chain scission and crosslinking in the matrix.

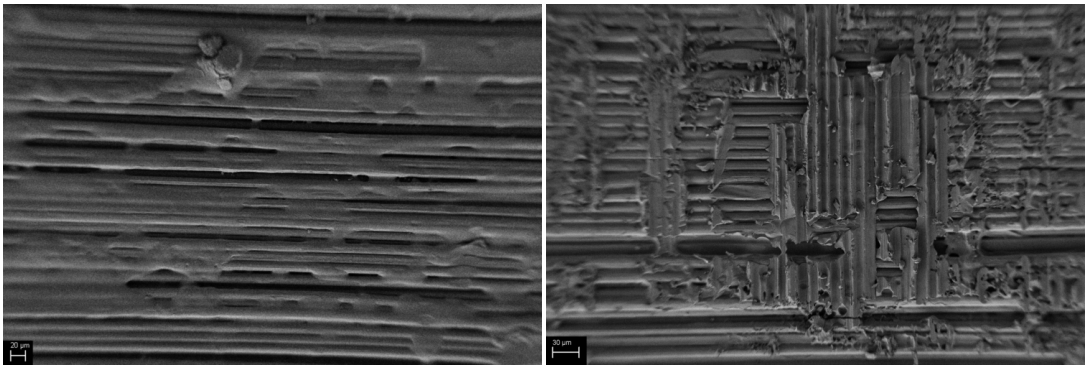

(a) (b)

Figure 6.5: Comparison of 100 hour UV aged (a) HB-210 (b) HB-212.

Figure 6.6 depicts the HB-210 and HB-212 after 200 hours of aging. The HB-210 still has a small amount of matrix visible on the surface of the composite seen in Figure 6.6 (a). The HB-212's matrix has almost completely disappeared in Figure 6.6 (b), where there is a small amount remaining in the center of the SEM image after 200 hours of UV exposure. This matrix degraded through hydrolysis and collected in the base of the QUV machine.

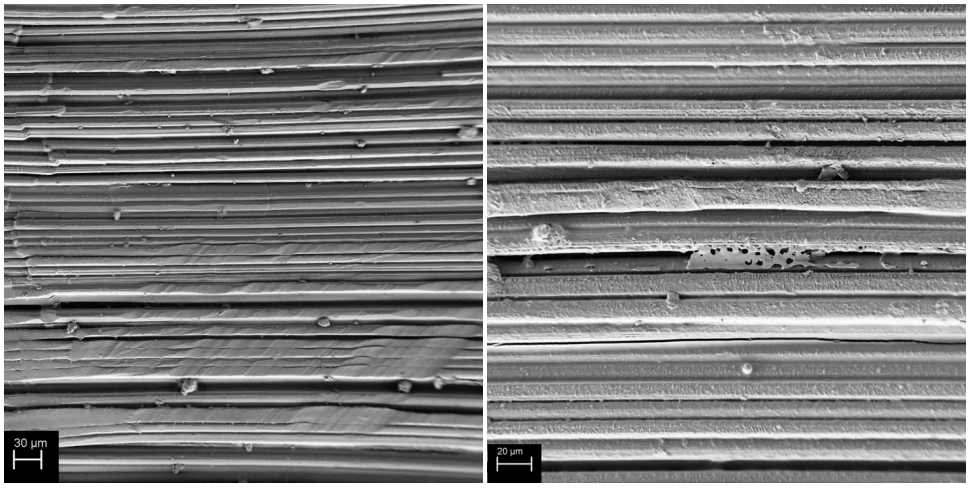

(a) (b)

Figure 6.6: Comparison of 200 hour UV aged (a) HB-210 (b) HB-212.

Figure 6.7 shows the SEM image of (a) HB-210 and (b) HB-212 after 600 hours of UV. Both samples have lost all matrix at this point as the Figure 6.7 shows bare UHMWPE fibers without the matrix materials. The fibers felt brittle in hand when mounting to the SEM slide.

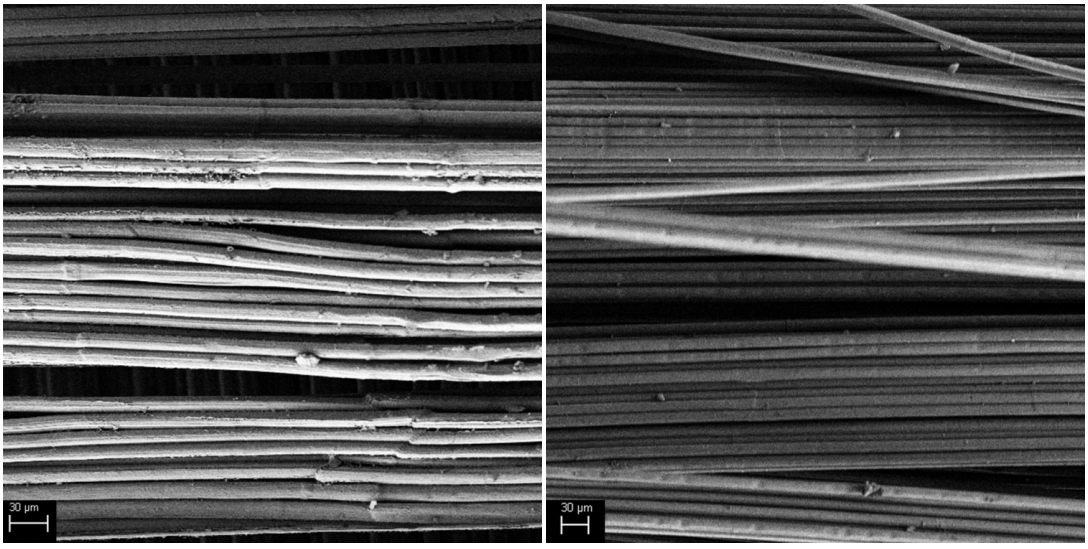

Figure 6.7: Comparison of 600 hour UV aged (a) HB-210 (b) HB-212.

UV DMA

Dynamic mechanical analysis was performed on HB-210 to characterize how the material viscoelastically responds changes in temperature after UV aging. Comparing the unaged HB-210's storage modulus to that of 100 hours of UV exposure $4x10^{-2}$ (s^{-1}) shows that the elastic response of the material is not affected.

Figure 6.8 shows how the storage modulus for the unaged and 100 hour UV fall along the same line within the 95% confidence interval. This reaction suggests the storage modulus is not altered at this level of UV radiation. However, Figure 6.5 (a) shows how the PUR matrix

is beginning to change on the surface of the composite, even though this is not measured by this DMA technique. As the temperature of the composite increases towards the melting temperature of polyethylene the storage modulus decreases.

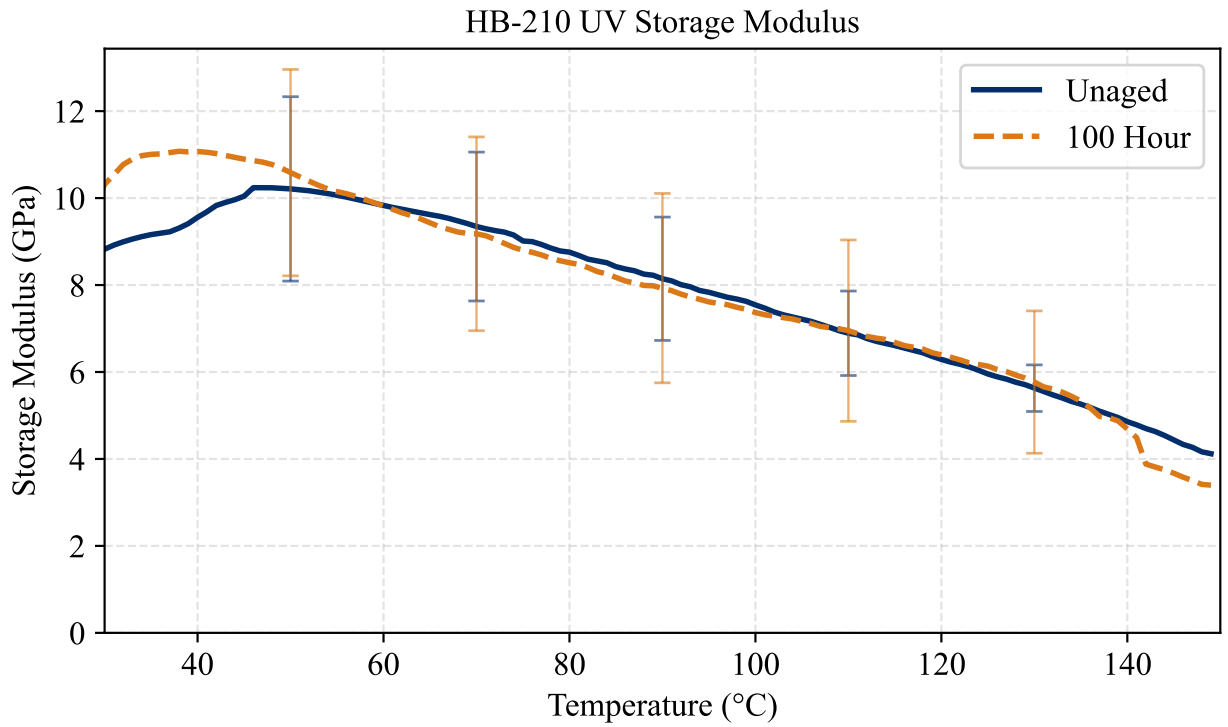

Figure 6.8: Storage modulus of HB-210 during a temperature ramp at 3°C/min with a strain rate of $4x10^{-2}$ (s^{-1}).

The UV aging causes on the viscous component of the modulus of HB-210 to increase as shown in Figure 6.9. This increase in loss modulus can be explained by the DMA recording the maximum loss modulus for the sinusoidal period. As this material is non-linear viscoelastic, as the stress strain curve moves up and to the left, the loss modulus will increase. This increase in loss modulus is at a reduction of the strain to failure. The confidence interval for these loss results is much higher for the UV aged loss modulus compared to the unaged and the storage modulus of the UV. This variability may be due to stochastic error in the DMA during these tests. As the samples felt more brittle, it was expected that the loss

modulus would decrease. However, at this strain rate, the unaged test may be dominated by matrix effects. Only after this matrix degraded through UV exposure, the fibers are able to be loaded and dominate the loss modulus response of the composite.

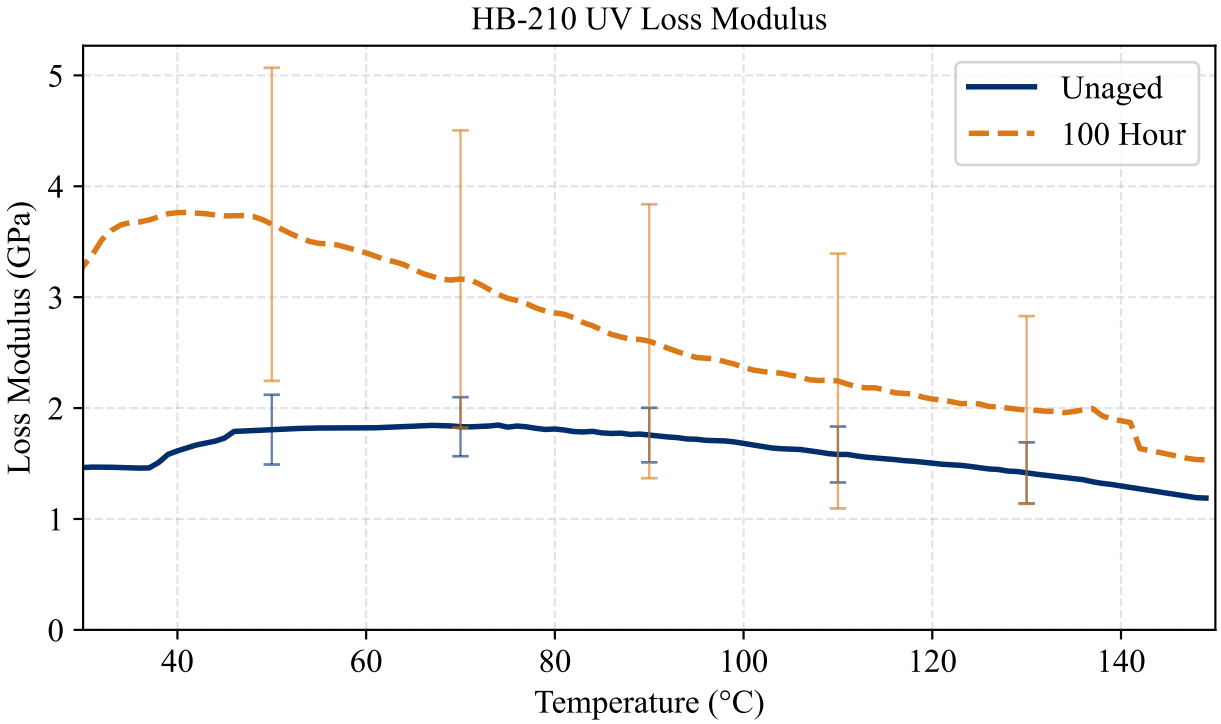

Figure 6.9: Loss modulus of HB-210 during a temperature ramp at 3°C/min with a strain rate of $4x10^{-2}$ (s^{-1}).

Hygrothermal DMA

To isolate the effects of UV-A photons from the temperature cycling and humidity present in the standard UV aging tests, the UHMWPE fiber reinforced composites were aged in a hygrothermal environment. The storage modulus response increases with hygrothermal aging. Figure 6.10 is the storage modulus response at a strain rate of $4x10^{-2}$ (s^{-1}) with a temperature ramp of 3°C/min. While the hygrothermal aging increases the initial elastic component of the modulus, as the temperature approaches the melting temperature of

polyethylene (~150°C) the elastic component of the modulus decreases to the same level as the unaged.

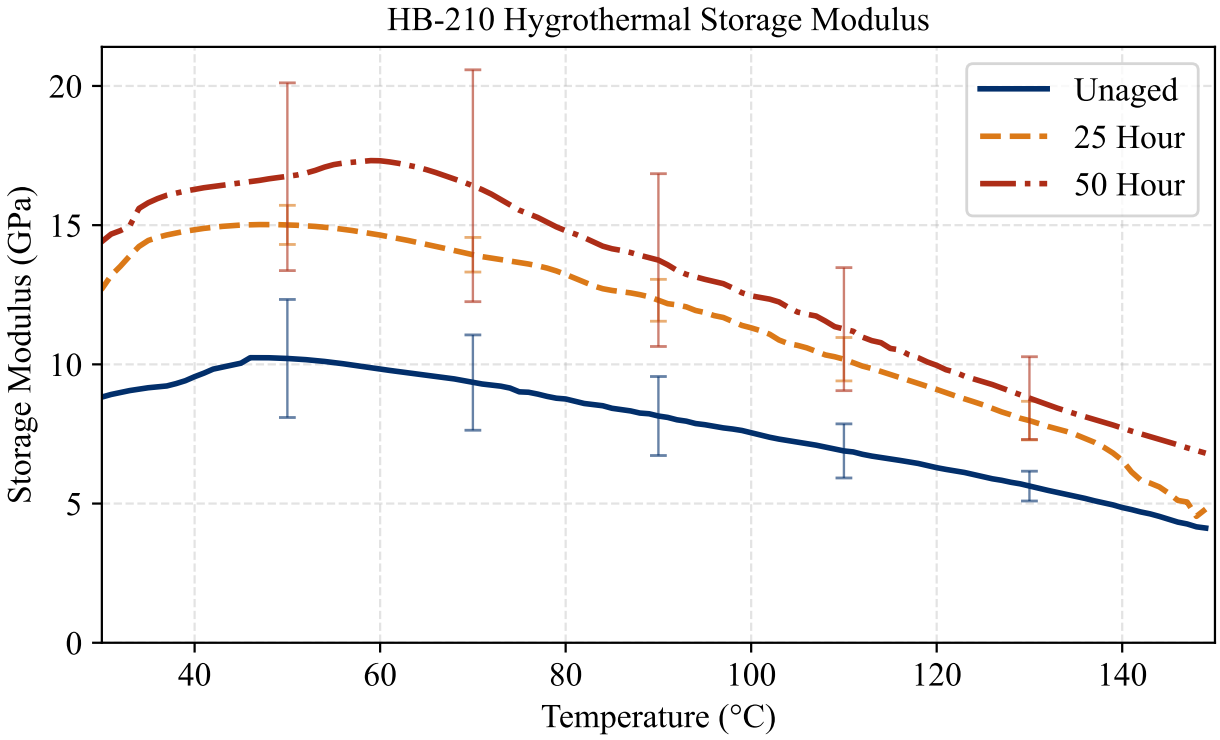

Figure 6.10: Storage modulus response of HB-210 after hygrothermal cyclical aging.

Figure 6.11 depicts the viscous component of the modulus of HB-210 at a strain rate of $4x10^{-2}$ (s^{-1}) across temperatures approaching the melting temperature of polyethylene. As hygrothermal aging increases, the loss modulus response also increases.

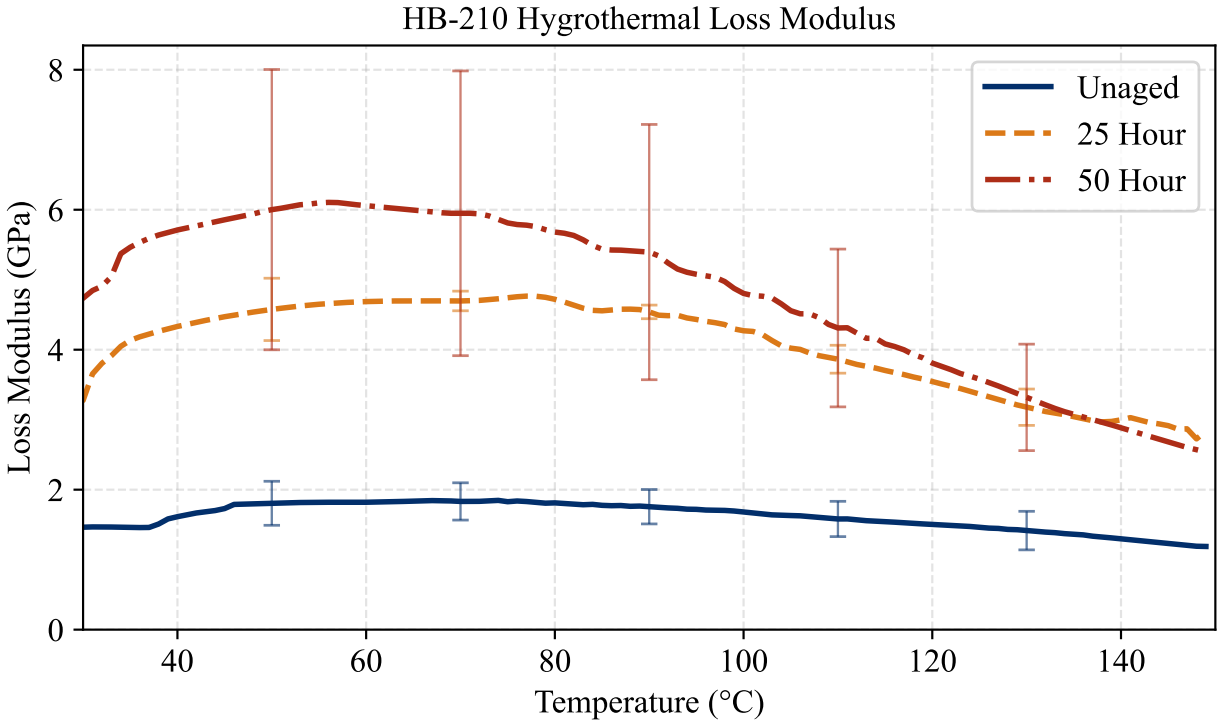

Figure 6.11: Loss modulus response of HB-210 after hygrothermal cyclical aging.

Temperature Cycling

As mentioned in Chapter 2, a common use case for this material is ballistics protection. These composite system can sit in cases or inside vehicle panels for an extended duration before use. These composites were subjected to accelerated aging from temperature cycling based on this use environment scenario. Over time, this temperature cycling can cause the composite material to deform slowly under constant stress, a phenomenon known as creep, and may even lead to material flow. To examine how temperature cycling influences creep behavior, DMA was used to characterize the composite during the creep tests. These creep tests compare how the UHMWPE composite responds to aging in UV, hygrothermal, and dry temperature cycling (oven).

Figure 6.12 is the maximum strain recovery (%) after a creep test of HB-210. The control for this test is at Hours = 0. Strain recovery is ratio of recovered strain, which is the amount of strain the material recovers after the stress is removed, divided by the total strain UHMWPE composites experience. This recovery phase is essential in characterizing the viscous and elastic response. Figure 6.12 shows that UV and hygrothermal aging have a deleterious influence on the ability for HB-210 to recover from strain, confirming that the UHMWPE material is undergoing increasing viscous behavior with age, as shown by the loss modulus increase in Figure 6.9 and Figure 6.11. Even though the storage modulus increased with hygrothermal aging in Figure 6.10, the material is still susceptible to plastic deformation under the same stress.

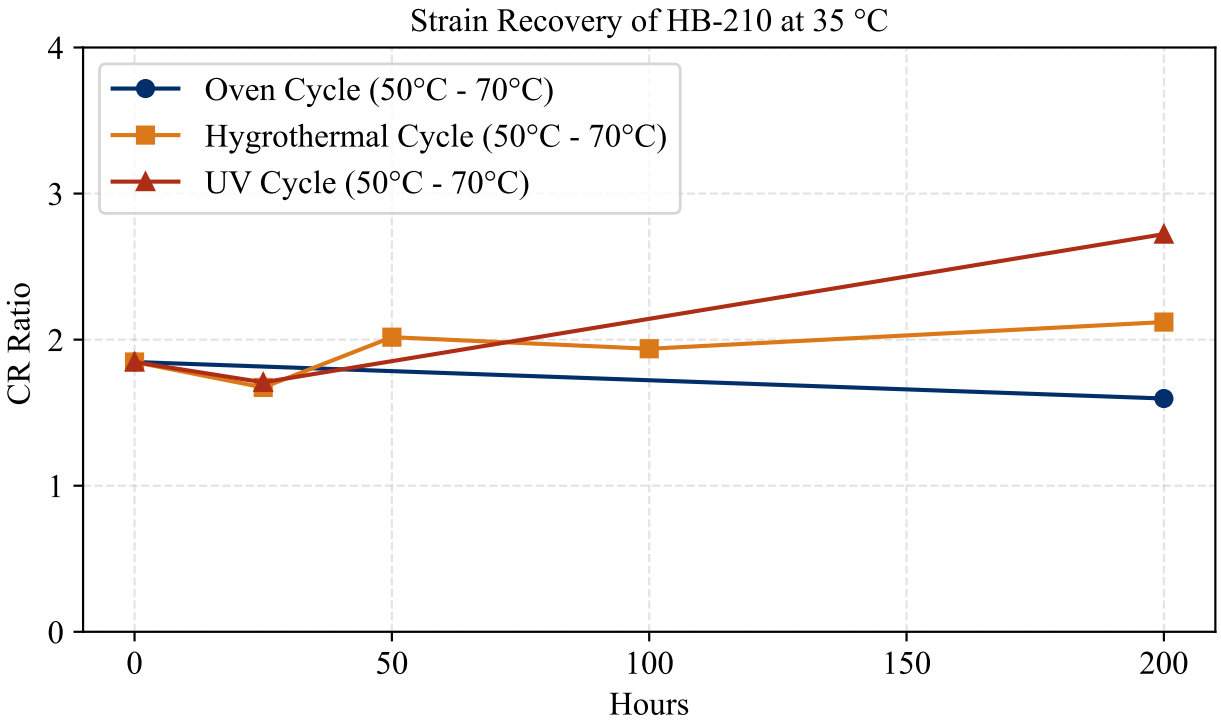

Figure 6.12: Maximum strain recovery of aged HB-210 after creep test at 35°C.

Figure 6.13 is the ratio of the creep compliance to the recovery compliance. This relationship confirms that as the composite is aged in UV and hygrothermal environments, the material has a higher tendency to not only deform, but also less ability to recover after that deformation. The dry temperature cycling inside an oven has nearly no effect. The UV and hygrothermal aging cause material changes through chain scission and crosslinking resulting in a more brittle composite. The hydrolysis of the matrix occurs faster in the synthetic rubber matrix in HB-212 faster than HB-210 preventing measurements via DMA.

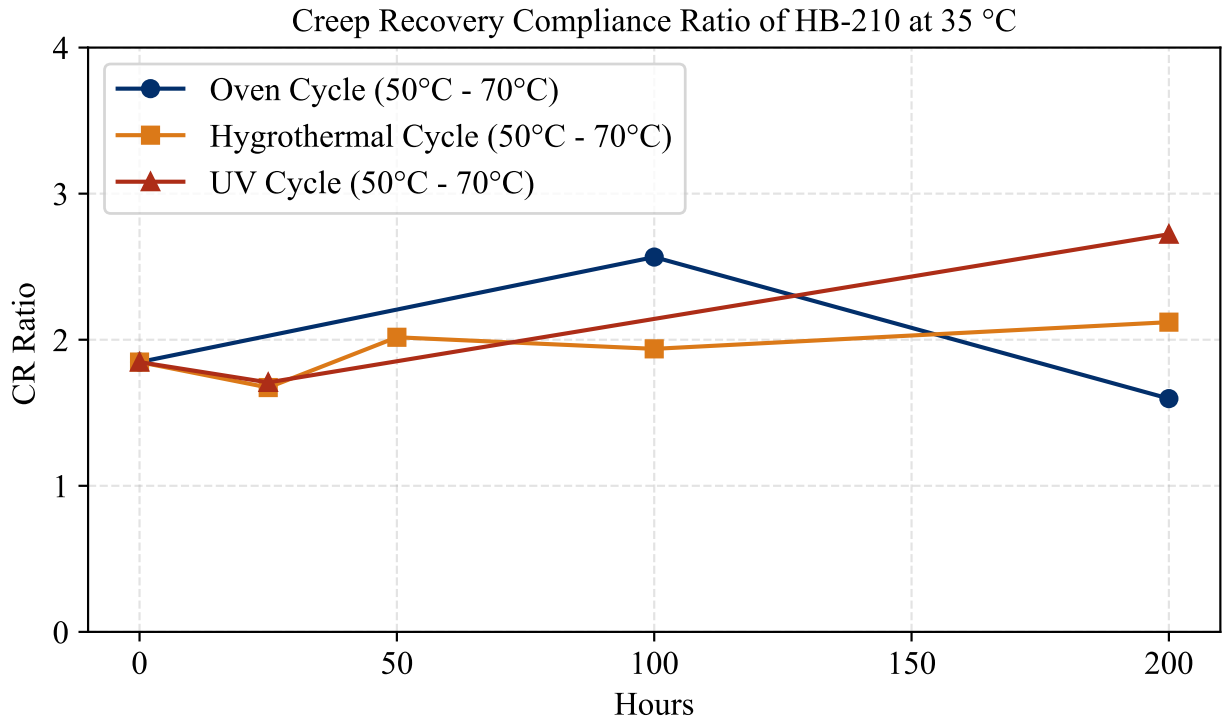

Figure 6.13: Ratio of creep compliance to recovery compliance after creep testing at 35°C.

During cyclical UV and hygrothermal aging, the magnitude of the complex modulus is increasing. This is likely at the cost of ductility as the material become more brittle. In classical elastic mechanics, the stress-strain curve is shifting up and to the left, decreasing the toughness of the material. As shown through the comparison of the dry oven temperature cycling compared to the UV and hygrothermal, the presence of water alters the fiber-matrix

bond and can cause this composite to age quicker. The SEM images confirm that observation and showcase how the rubber matrix in HB-212 is more vulnerable to aging than the PUR matrix in HB-210.

RADIATION AGING RESULTS AND DISCUSSION

UHMWPE fiber reinforced composites were aged in radiation environments of X-rays, γ-rays, and neutrons. After aging, these single layer composite samples were interrogated for changes in the viscoelastic response characterized by Dynamic Mechanical Analysis (DMA). These DMA tests followed a standard procedure described in Chapter 3. The results and discussion of how these UHMWPE fiber reinforced composites responded to DMA after ionizing radiation exposure are stated in this chapter.

Figure 7.1 shows the storage modulus response of unaged UHMWPE composites from strain rates $1x10^{-1}$ (s^{-1}) to $3x10^{1}$ (s^{-1}). The unaged HB-210 and HB-212 have a higher storage modulus compared to the SR-5241 due to the choice of gel-spinning solvent resulting in a higher drawing ratio.

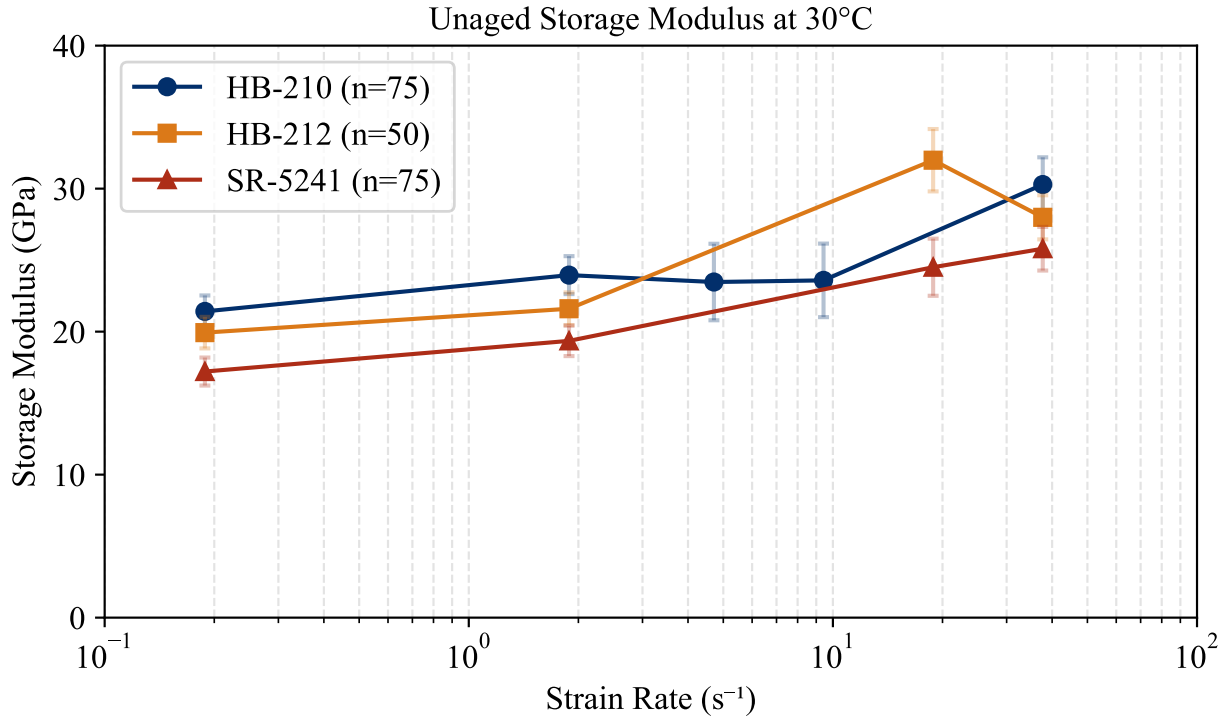

Figure 7.1: Comparison of unaged $[0/90]_2$ UHMWPE composite's storage modulus over isothermal strain rates.

Figure 7.2 is the loss modulus response of these same unaged UHMWPE composites. This shows that with an increasing strain rate, the composites have a higher viscous response, which is advantageous for dissipating energy.

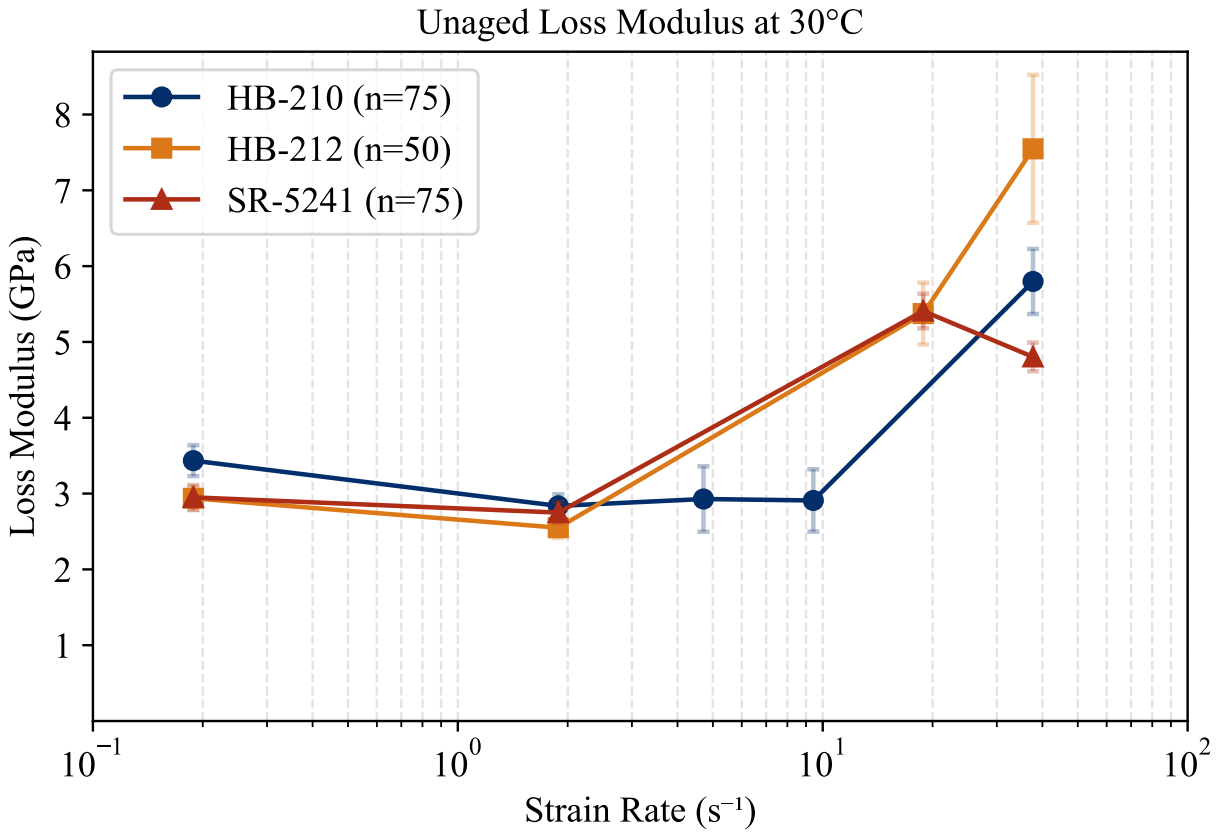

Figure 7.2: Comparison of unaged $[0/90]_2$ UHMWPE composite's loss modulus over isothermal strain rates.

X-ray Aging

X-rays are a type of ionizing radiation that have a lower energy than γ-rays. Each aging level was conducted on a separate sample of UHMWPE fiber reinforced composite. These plots are the average with the number of tests represented by 'n' in the legend. The error bars are the 95% confidence interval.

HB-210 X-ray Exposure

Figure 7.3 depicts the average tan δ response of HB-210 after X-ray exposure. The unaged HB-210 has the lowest tan δ compared to the X-ray aging. The 50 Gy dose, created a large degree of uncertainty at $1.9x10^{1}$ (s^{-1}), where the tan δ nearly tripled from the strain rate of $1.9x10^{0}$ (s^{-1}). This is likely an error in testing methodology as the DMA machine began to resonate at this strain rate. The storage modulus increases with strain rate which is expected for this viscoelastic material.

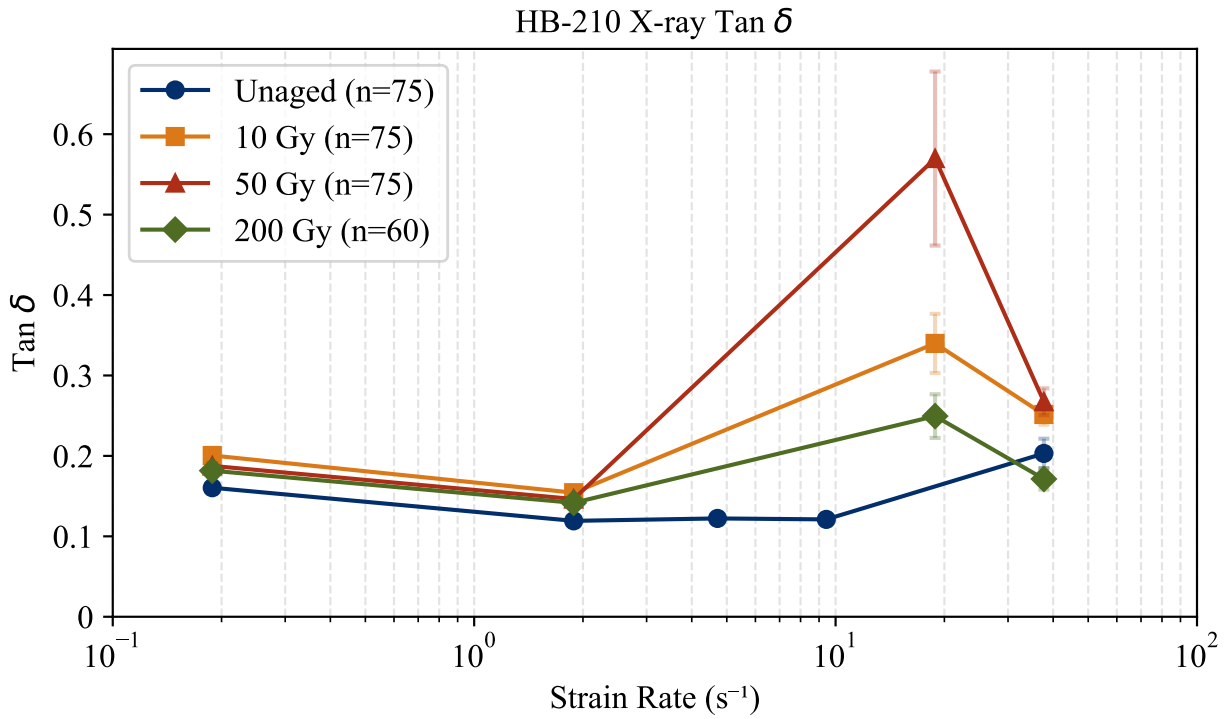

Figure 7.3: Mean tan δ over strain rate of HB-210 $[0/90]_2$ after X-ray exposure.

The storage modulus response of HB-210 to X-ray exposure is presented in Figure 7.4. As the strain rate increases, the storage modulus response also increases linearly across the log scale. However, the 10 Gy aging has the highest storage modulus for all strain rates tested. The 50 Gy and 200 Gy are statistically identical over the strain rates. While the unaged has the lowest storage modulus response compared to the X-ray aging, which is expected as the

ionizing radiation has the potential to increase the storage modulus through crosslinking.

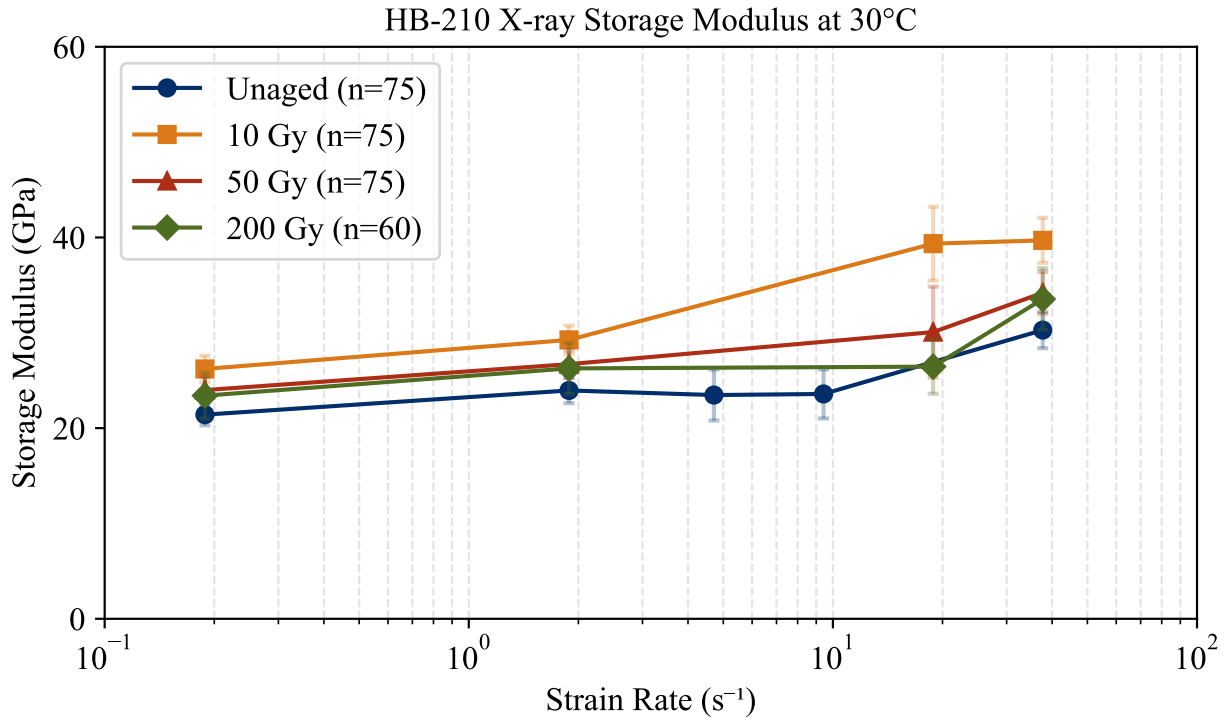

Figure 7.4: Mean storage modulus over strain rate of HB-210 $[0/90]_2$ after X-ray exposure.

Figure 7.5 is the loss modulus response of HB-210 after X-ray aging. The loss modulus of the X-ray aged samples decreases from $1.9\text{x}10^0$ (s^{-1}) to $3.8\text{x}10^1$ (s^{-1}), while the unaged HB-210 increases over that same interval. As X-ray dose increases, the HB-210's loss modulus response also decreases which is expected as the ionizing radiation causes chain scission, which will reduce the dampening potential for this material. However, in the case of HB-210, the unaged coupons have a lower loss modulus response compared to the X-ray exposed samples. This response is from the overall complex modulus increasing as the material becomes less tough but more brittle. Another part of this error could have arisen from stochastic error potentially from selection of a weaker sample area from the composite to for the DMA coupons.

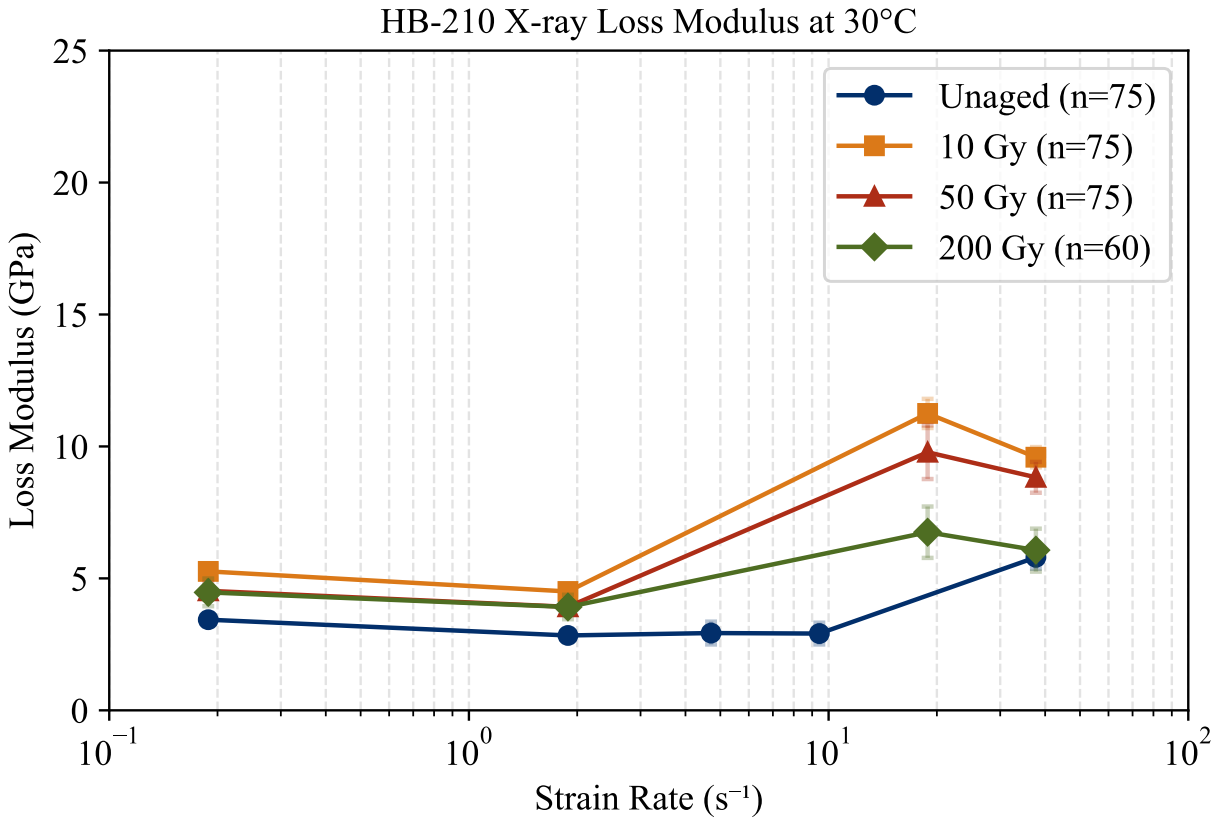

Figure 7.5: Mean loss modulus over strain rate of HB-210 $[0/90]_2$ after X-ray exposure.

HB-212 X-ray Exposure

The tan δ response of the HB-212 material is presented in Figure 7.3. The 50 Gy and 200 Gy X-ray aged samples are nearly identical in the tan δ response. The 10 Gy tan δ has a higher degree of uncertainty at the higher strain rates, likely from the lower number of samples tested via DMA. The unaged HB-212 tan δ has an increasing trend with strain rate, meaning that the ratio of the loss modulus increases at a faster rate than the storage modulus.

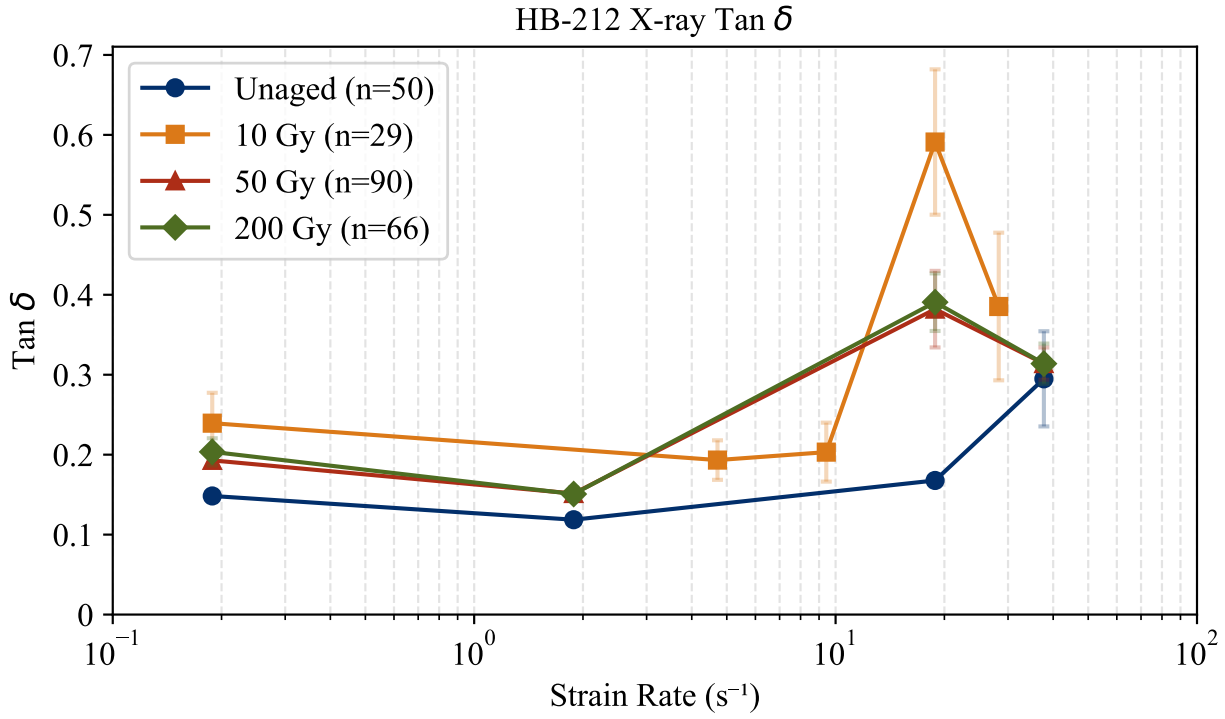

Figure 7.6: Mean tan δ over strain rate of HB-212 $[0/90]_2$ after X-ray exposure.

Figure 7.7 is the average HB-212 storage modulus at 30°C after X-ray aging. The unaged and 50 Gy samples have an identical storage modulus response, within the confidence interval. The 200 Gy sample has the highest storage modulus response and follows the same trend as the unaged and 50 Gy tests. This follows the theory that ionizing radiation increases the storage modulus through crosslinking. Deviating from theoretical expectations, the sample

exposed to 10 Gy exhibits a lower storage modulus response than its unaged counterpart. This anomaly could be attributed to the smaller sample size, potentially influencing the unexpected response.

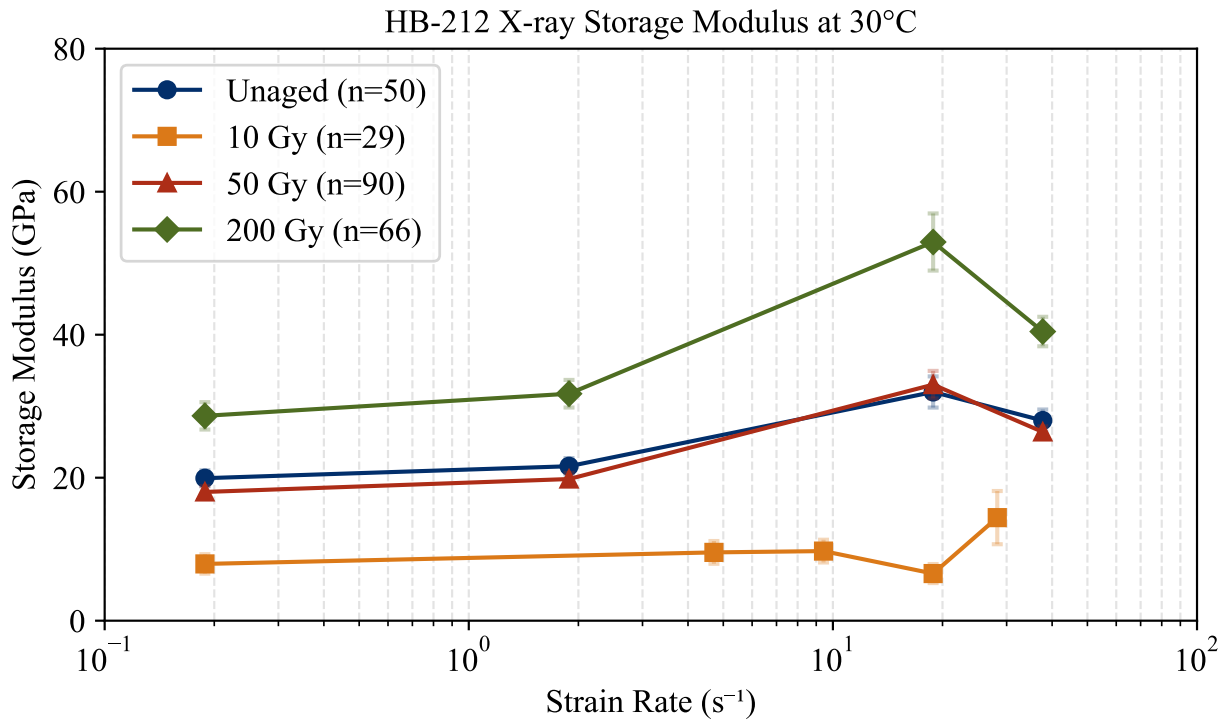

Figure 7.7: Mean storage modulus over strain rate of HB-212 $[0/90]_2$ after X-ray exposure.

The average loss modulus response at 30°C for the X-ray aged HB-212 is shown in Figure 7.8. The 200 Gy samples have a higher average loss modulus than the rest. The unaged and 50 Gy samples have nearly identical loss moduli values except for at $1.9\text{x}10^1$ (s^{-1}) where the 50 Gy doubles that of the unaged. This could be from a stochastic resonance in the DMA that occurs at this driving frequency/strain rate. The unaged and 10 Gy follow the same trend over the strain rates, while the 200 Gy and 50 Gy follow the same spike trend at $1.9\text{x}10^1$ (s^{-1}).

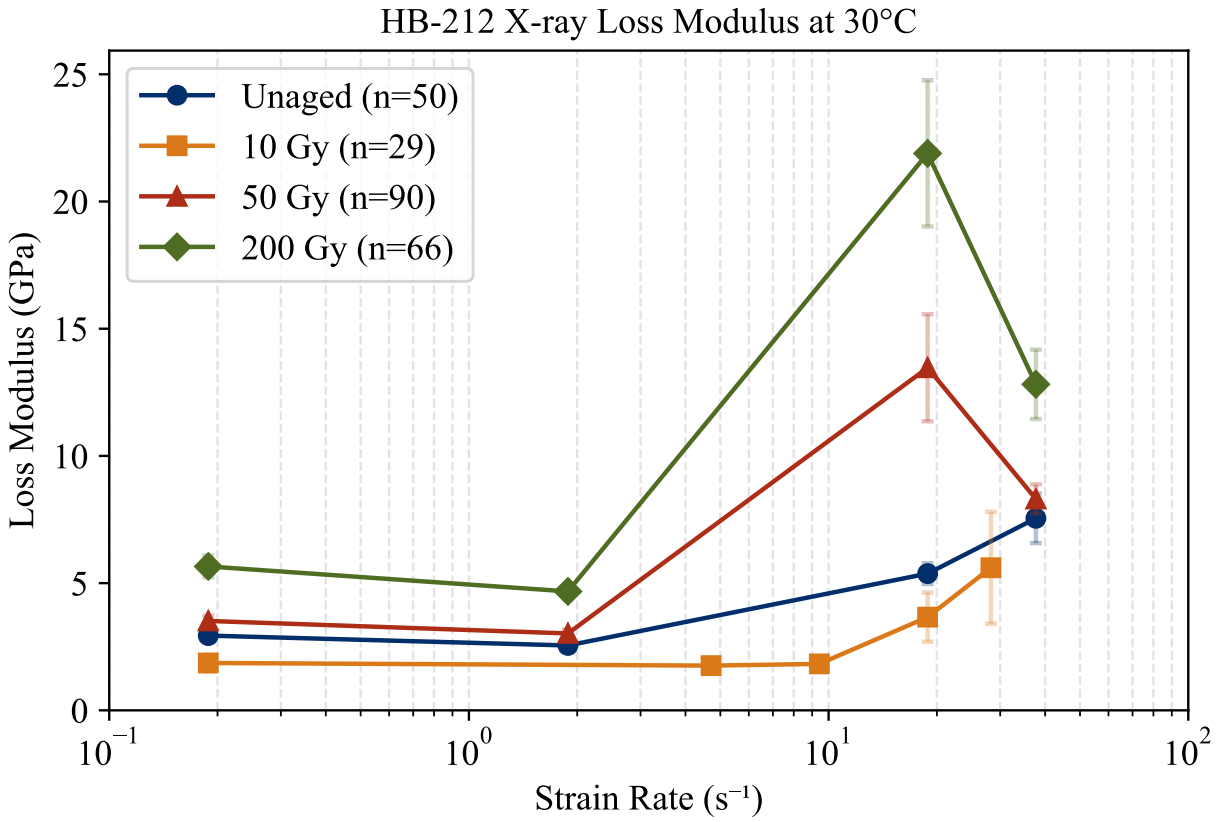

Figure 7.8: Mean loss modulus over strain rate of HB-212 $[0/90]_2$ after X-ray exposure.

SR-5241 X-ray Exposure

Figure 7.9 is the average tan δ response to X-ray exposure of SR-5241. The tan δ remains nearly constant across the strain rate and through the X-ray doses, except for the 200 Gy samples at the strain rate of $1.9x10^{1}$ (s^{-1}), where it doubles from 0.2 to 0.4. This jump in tan δ is also accompanied by a large increase in the error bars. This is likely from resonance in the dynamic mechanical analysis machine during these test at the sinusoidal 100 Hz displacement, as evidenced by a vibration noise during this frequency testing, and not a reflection of the material properties.

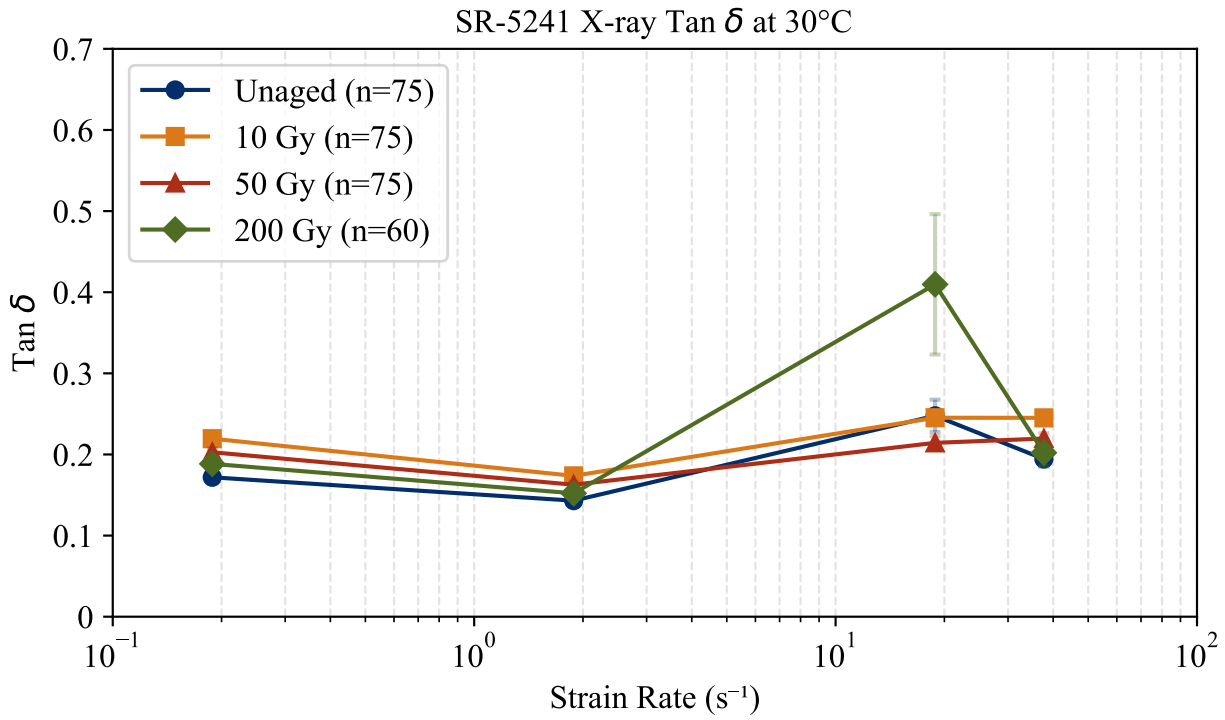

Figure 7.9: Mean tan δ over strain rate of SR-5241 $[0/90]_2$ after X-ray exposure.

Unpacking the tan δ, the storage modulus of the SR-5241 after X-ray exposure is presented in Figure 7.10. The unaged SR-5241 has the lowest storage modulus over the strain rate of any of the samples. As the material is exposed to higher doses of ionizing radiation, chain scission and crosslinking is more likely to occur, which will increase the

storage modulus response as the material becomes more brittle.

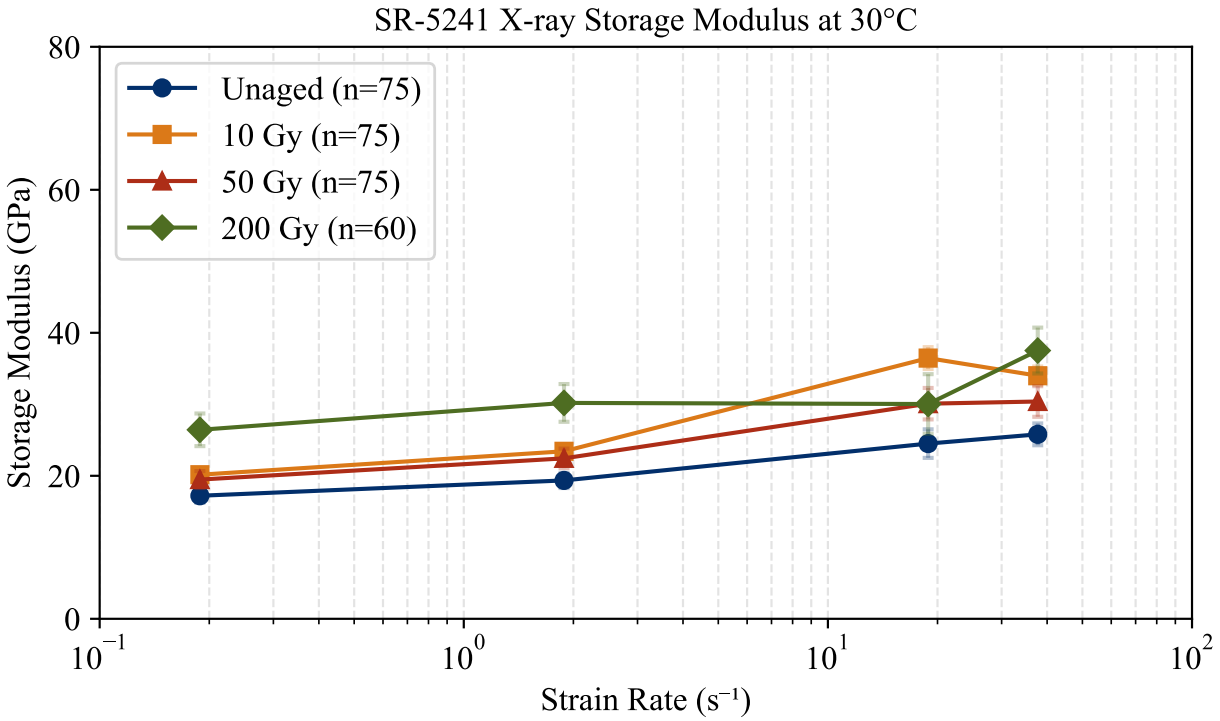

Figure 7.10: Mean storage modulus over strain rate of SR-5241 $[0/90]_2$ after X-ray exposure.

The average loss modulus for the SR-5241 is reported in 7.11. The X-ray aging does not seem to have a large effect on the dampening response of this composite. There is a slight increase in loss modulus with X-ray aging, but is difficult to discern at these total doses. As the strain rate increases both the unaged and various X-ray dosed samples have a higher loss modulus response. This response is expected for this material to have a higher dampening ability as the strain rate increases.

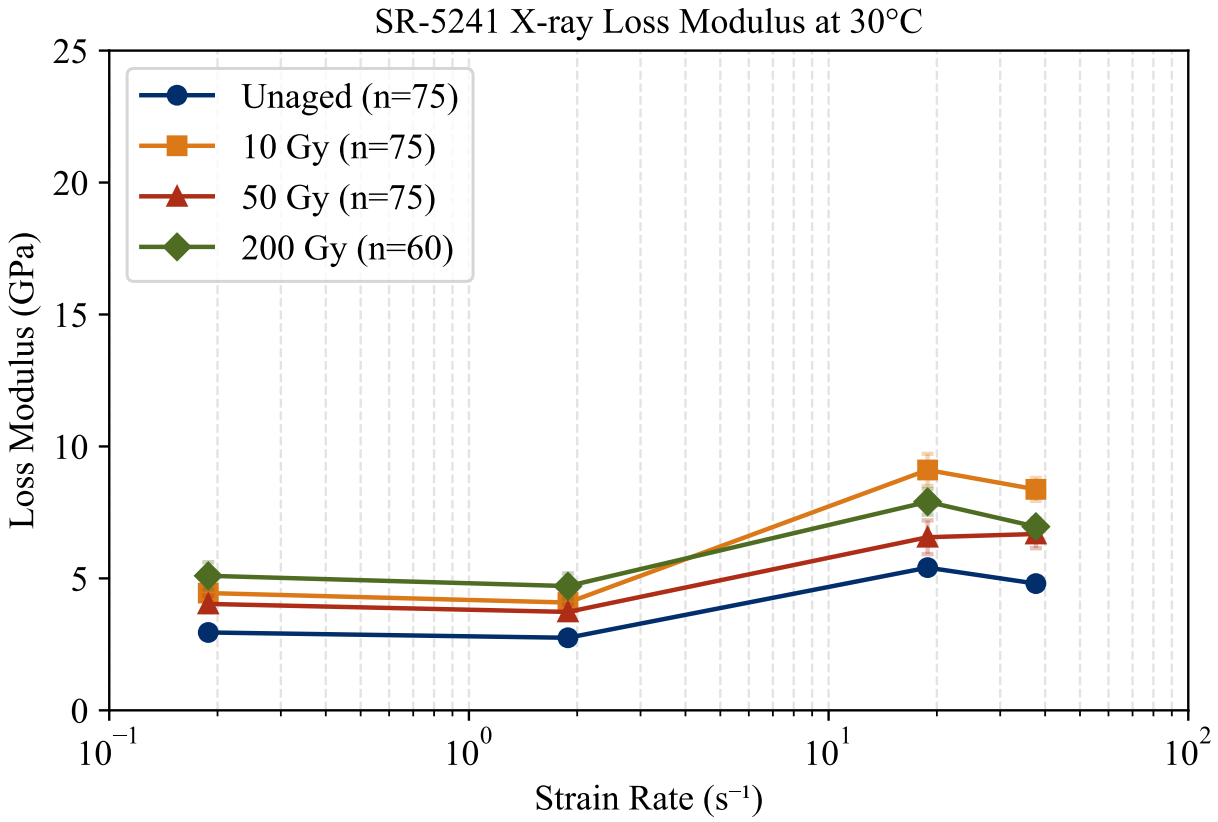

Figure 7.11: Mean loss modulus over strain rate of SR-5241 $[0/90]_2$ after X-ray exposure.

γ-ray Aging

To increase the amount of ionizing radiation exposure of these composites, a γ-ray source was used to age the UHMWPE fiber reinforced single layer composites. The viscoelastic response was characterized using dynamic mechanical analysis. Each total dose level was conducted on a separate sample of the UHMWPE fiber reinforced composite. These plots are the mean average, with the number of tests represented by 'n' in the legend. The error bars are the 95% confidence interval of the plotted mean.

HB-210 γ-ray Exposure

Figure 7.12 is the average tan δ response of HB-210 after exposure to a γ-ray source. For strain rates between $1x10^{-1}$ (s^{-1}) and $1x10^{0}$ (s^{-1}), the tan δ response is identical. However, at $1x10^{1}$ (s^{-1}), the 0.1 kGy, 10 kGy, and 100 kGy have a higher response than the unaged. The 1 kGy has a spike at that strain rate but is likely from stochastic resonance in the DMA at that strain rate as evidenced by the higher confidence interval and the downward trend at the higher strain rates.

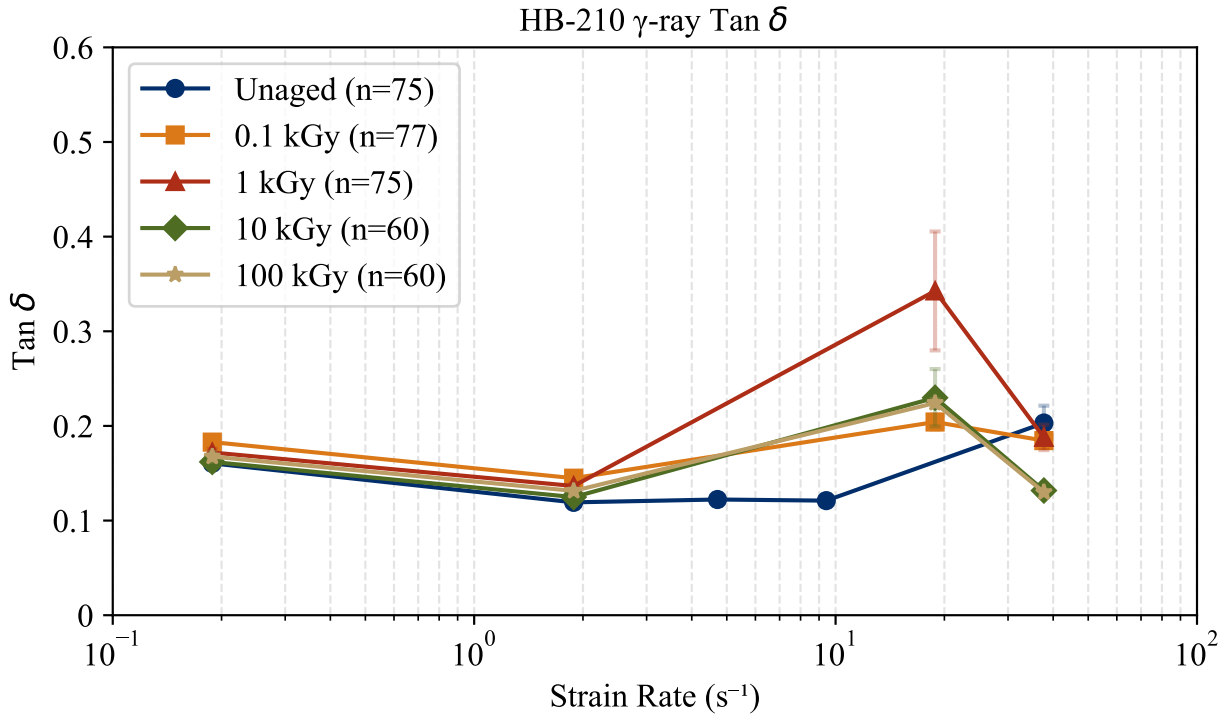

Figure 7.12: Mean tan δ over strain rate of HB-210 $[0/90]_2$ after γ-ray exposure.

The storage modulus for the γ-ray aged composites is shown in Figure 7.13. The unaged storage modulus is less compared to the γ-ray exposed composites, which is expected as the ionizing radiation causes chain scission and crosslinking. The increasing strain rate results in a average increase in storage modulus across the experiment, which known for these UHMWPE fiber reinforced composites.

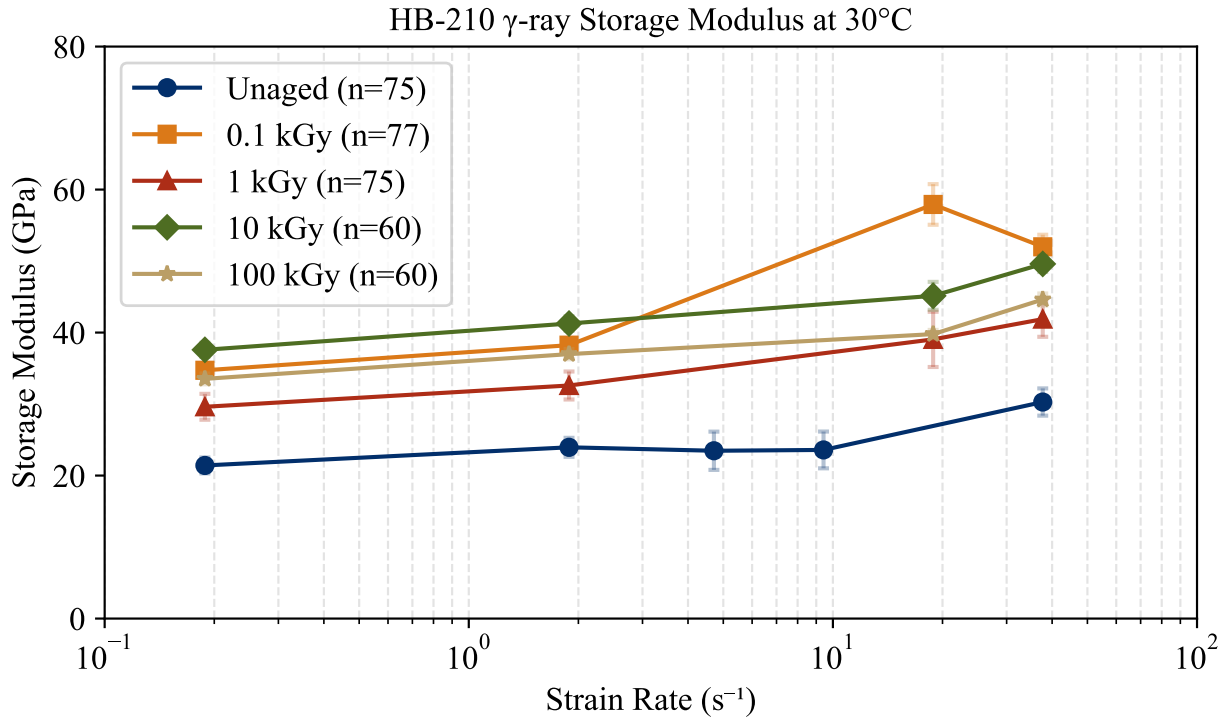

Figure 7.13: Mean storage modulus over strain rate of HB-210 $[0/90]_2$ after γ-ray exposure.

Figure 7.14 depicts the average isothermal loss modulus at 30°C for the HB-210 UHMWPE fiber reinforced composite. The γ-ray aged samples exhibit a similar pattern over the stain rate range, while the unaged remains nearly constant until strain rates above $1.9\text{x}10^{0}$ (s^{-1}) where it increases to 5 GPa. The 0.1 kGy coupons have a higher loss modulus across all strain rates, which does not follow the theory that increasing radiation will decrease the dampening ability of the material through crosslinking. This deviation could be in part due to stochastic error during sample selection and preparation. The coupons cut from the

composite roll used for the 0.1 kGy aging could have contained higher molecular weight fibers than the other samples used in this experiment.

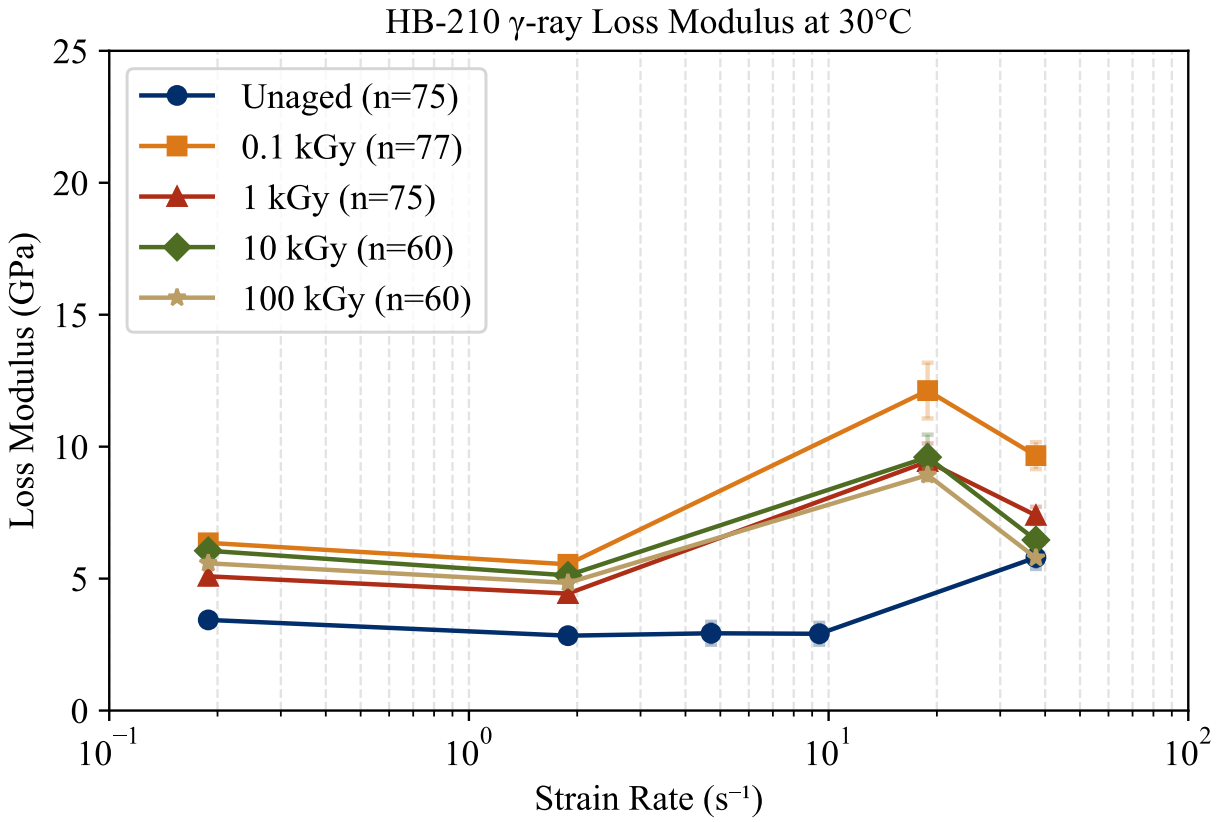

Figure 7.14: Mean loss modulus over strain rate of HB-210 $[0/90]_2$ after γ-ray exposure.

HB-212 γ-ray Exposure

Figure 7.15 is the average tan δ response after γ-ray aging. This shows that the γ-ray aging increases the proportion of viscous component of the complex modulus over the strain rates compared to the unaged.

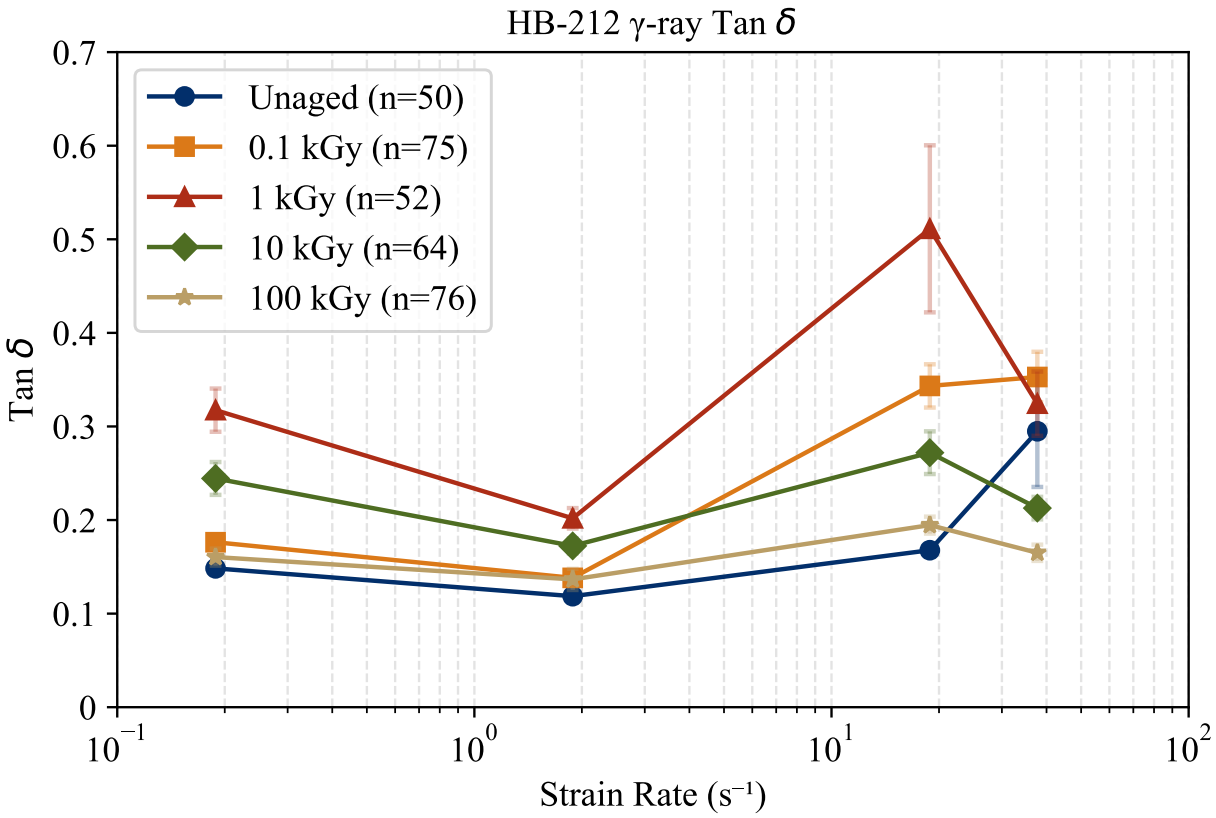

Figure 7.15: Mean tan δ over strain rate of HB-212 $[0/90]_2$ after γ-ray exposure.

Figure 7.16 depicts the isothermal storage modulus response of single layer HB-212 after γ-ray radiation. The γ-rays interact with the polymer to cause chain scission, but at the same time can impart heat into the sample creating more crosslinks within the chain structure. As strain rate increases, the storage modulus response increases, with the exception of $1x10^{1}$ (s^{-1}), which is due to the DMA recording the resonance as the material's storage modulus. The storage modulus nearly doubles from the unaged to the 100 kGy aged samples across the strain rates. This trend holds true except for the 0.1 kGy which ranges between the 100 kGy storage modulus and the 1 kGy storage modulus over the strain rates tested. This error could be from manufacturing as the molecular weight of the gel-spun polymers is not uniform throughout the material and since these DMA coupons are small, they could have been selected from a portion of the HB-212 roll that has a higher molecular weight leading to a higher storage modulus.

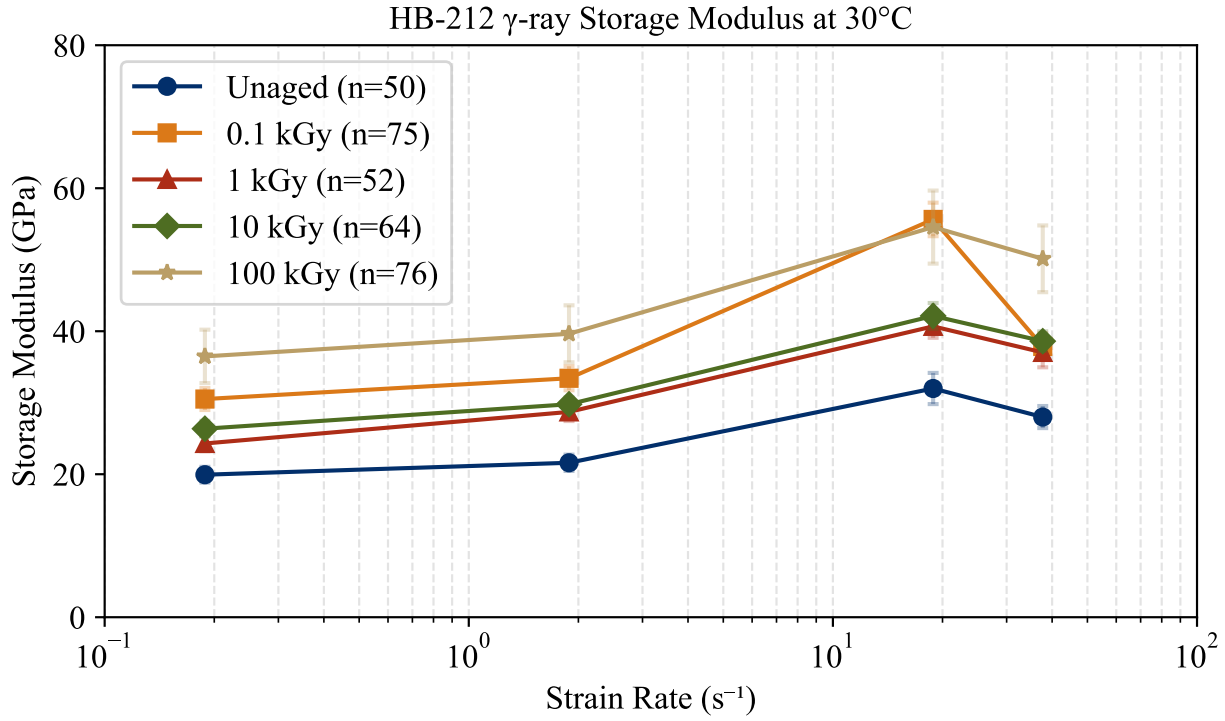

Figure 7.16: Mean storage modulus over strain rate of HB-212 $[0/90]_2$ after γ-ray exposure.

The loss modulus response of HB-212 after exposure to γ-rays is shown in Figure 7.17. The unaged HB-212 shows a typical response of increasing loss modulus as the strain rate increases. However, the 1 kGy and 0.1 kGy have a spike at $1.9\text{x}10^{1}$ (s^{-1}). The general trend of γ-ray irradiated HB-212 is a slight decrease, under 15% decrease from strain rates $1.9\text{x}10^{-1}$ (s^{-1}) to $1.9\text{x}10^{0}$ (s^{-1}), and increasing from $1.9\text{x}10^{0}$ (s^{-1}) to $1.9\text{x}10^{1}$ (s^{-1}), and slightly decreasing as the strain rate approaches 10^{2} (s^{-1}). However, the viscoelastic nature of this material would suggest that the higher the strain rate in this realm would lead to a higher loss modulus response. There has been a stochastic resonance in the DMA at strain rates around $1.9\text{x}10^{1}$ (s^{-1}), which explains this spike.

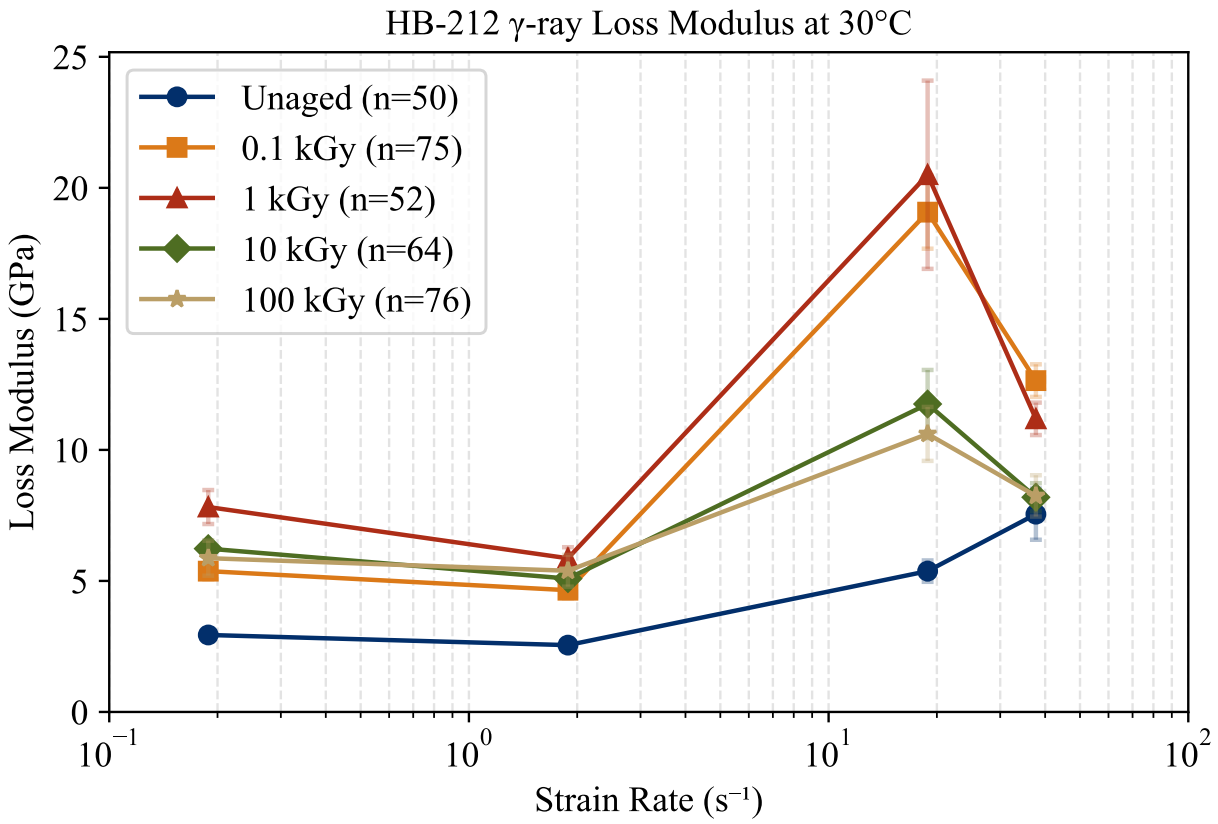

Figure 7.17: Mean loss modulus over strain rate of HB-212 $[0/90]_2$ after γ-ray exposure.

SR-5241 γ-ray Exposure

Figure 7.18 depicts the average tan δ vs strain rates for SR-5241 single layer composites after γ-ray radiation. For strain rates less than 1.9x10^1 (s^{-1}) the 100 kGy aged coupons have a highest tan δ.

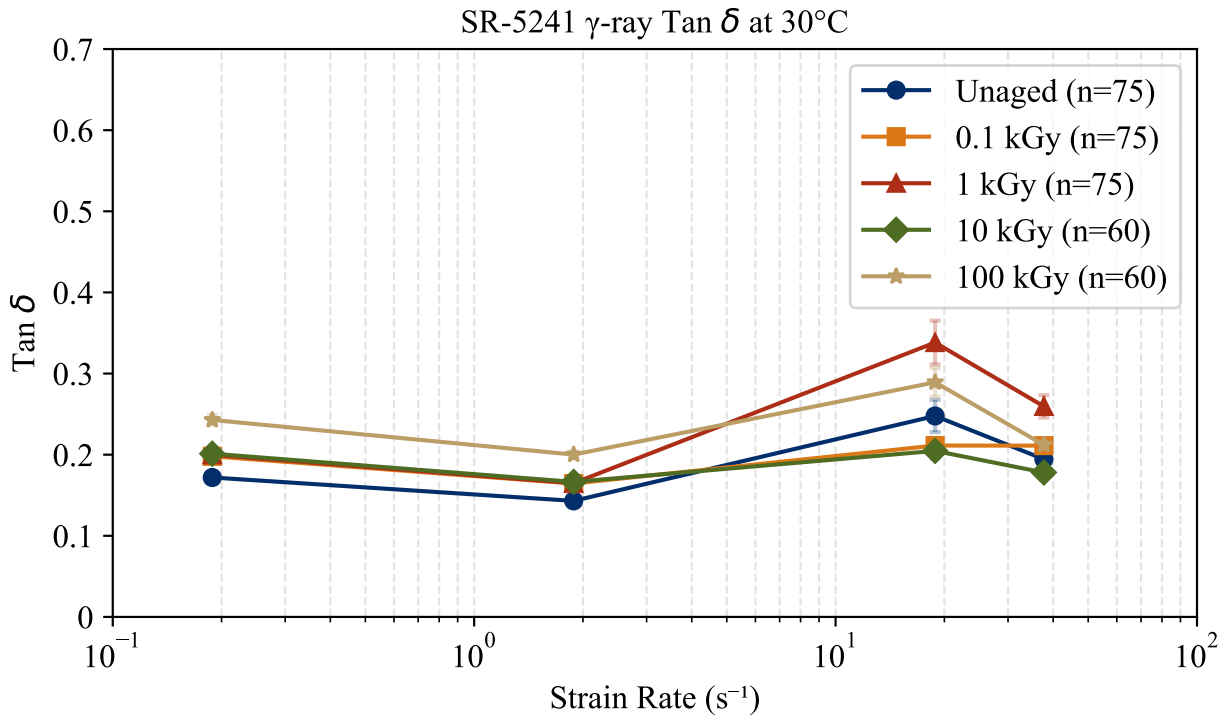

Figure 7.18: Mean tan δ over strain rate of SR-5241 $[0/90]_2$ after γ-ray exposure.

The storage modulus response of the composite made from gel-spun fibers dissolved in decalin consolidated with a polyurethane rubber matrix is plotted in Figure 7.19. As the strain rate increases on the logarithmic scale the storage modulus increases linearly. As the samples were left in the γ-ray radiation longer the storage modulus increased as the ionizing radiation causes chain scission and forms crosslinks in the polymer. The interesting response is that the 0.1 kGy and 1 kGy samples have a closely paired response, as does the 10 kGy and the 100 kGy γ-ray aged SR-5241. The 100 kGy γ-ray aged sample begins to deviate from the 10 kGy at 3.8x10^1 (s^{-1}).

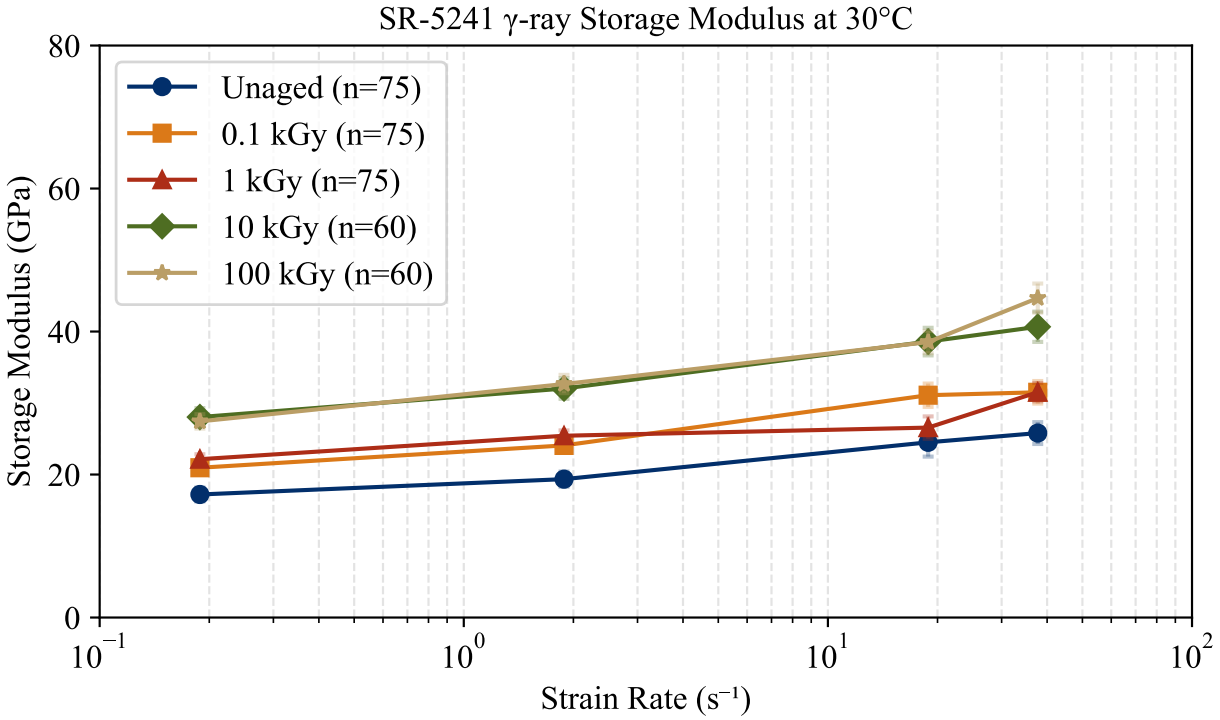

Figure 7.19: Mean storage modulus over strain rate of SR-5241 $[0/90]_2$ after γ-ray exposure.

Figure 7.20 shows the loss modulus response over increasing strain rates of SR-5241 $[0/90]_2$ after γ-ray radiation. With aging, the loss modulus increases uniformly from unaged to 100 kGy across the strain rates. This response shows the radiation aging causes the composite to become brittle which shifts the stress strain curve up and to the left which can increase the maximum loss modulus response recorded by the DMA.

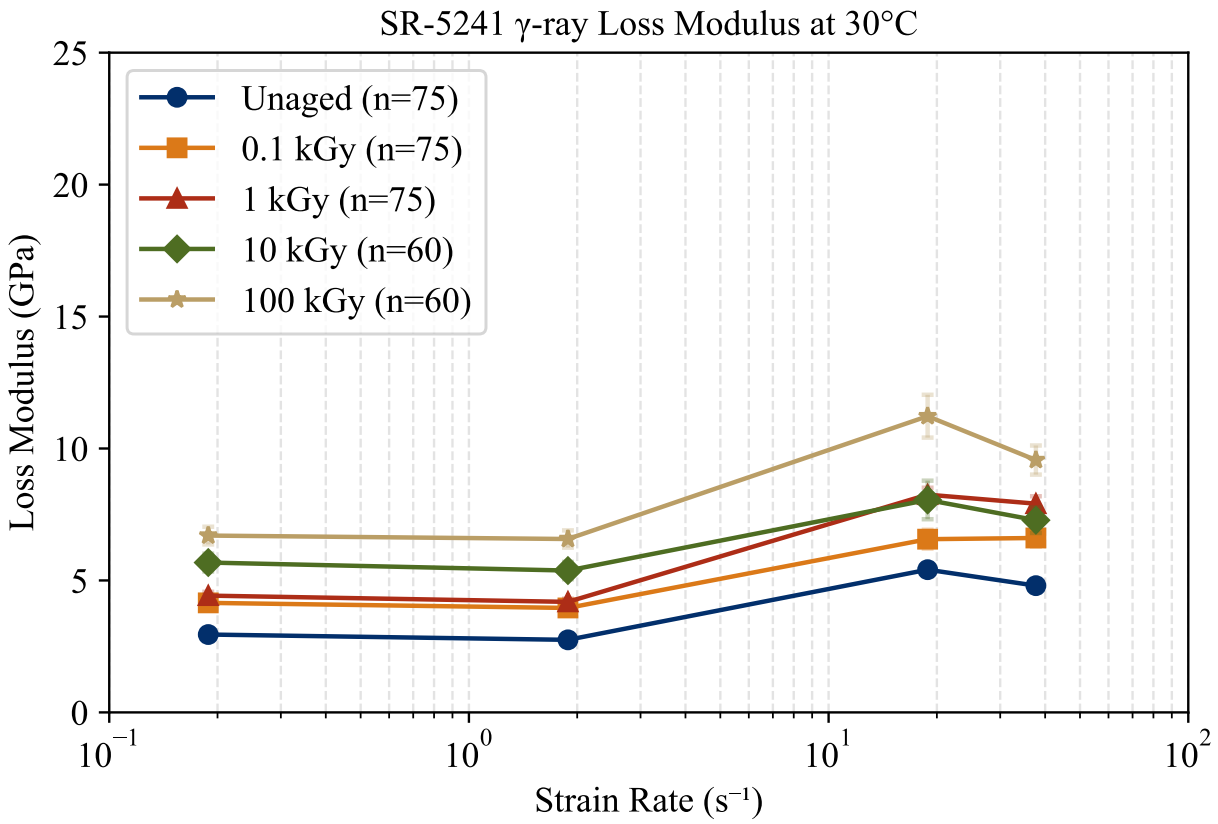

Figure 7.20: Mean loss modulus over strain rate of SR-5241 $[0/90]_2$ after γ-ray exposure.

Figure 7.21 depicts the color change after 100 kGy γ-ray exposure. The SR-5241's appearance was altered to an almond-beige color, while the color of HB-210 only turned to a light straw color, despite both of these composites having a matrix made from PUR. The SR-5241 appeared to be affected by radiation to a higher degree. The HB-212's synthetic rubber matrix was in the middle of the other two in terms of discoloration. There was no

noticeable color change for lower doses of γ-rays or X-rays.

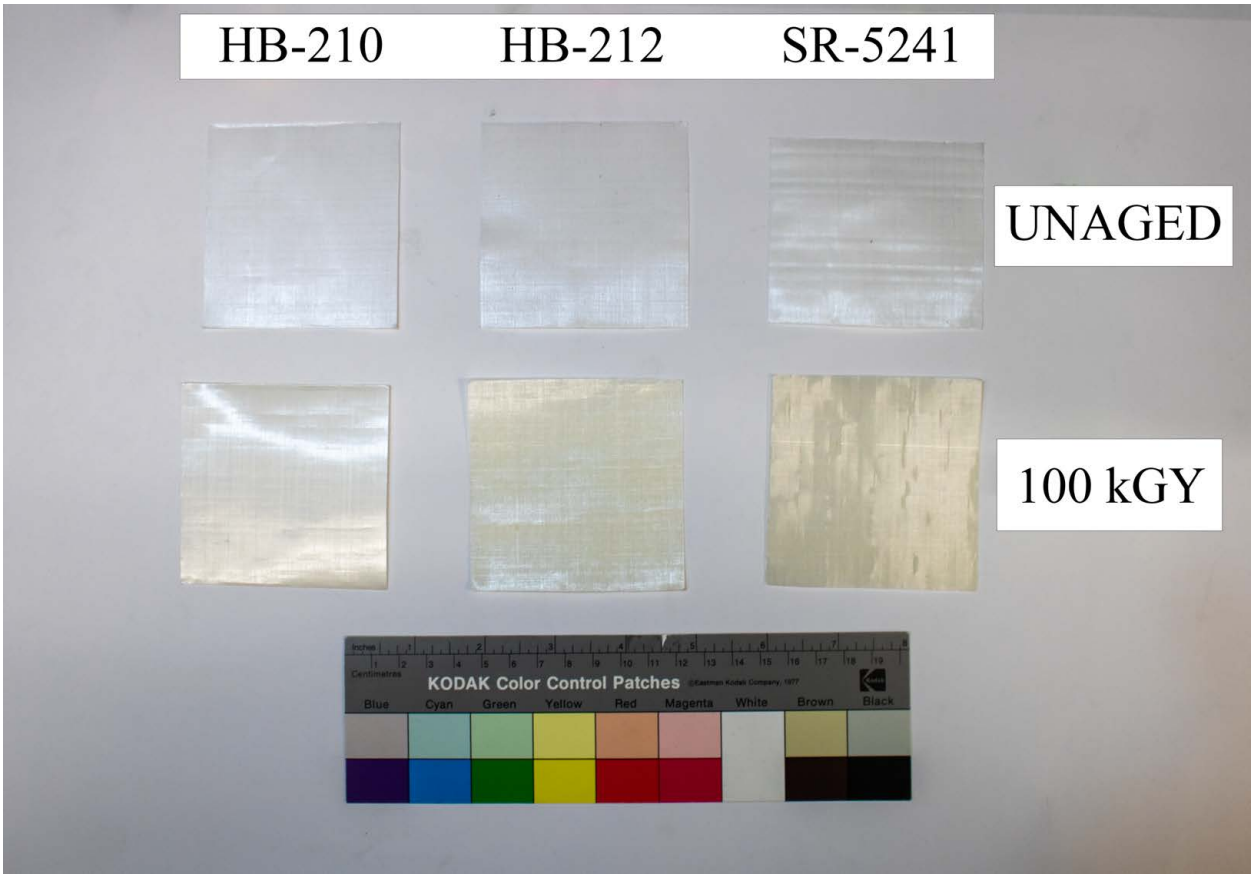

Figure 7.21: Darkening of the composites after 100 kGy γ-ray exposure.

Thermal Neutron Aging

The UHMWPE fiber reinforced composites were exposed to thermal neutrons before evaluating the viscoelastic response through dynamic mechanical analysis.

HB-210 Neutron Exposure

Figure 7.22 is the tan δ response after exposing a single layer of HB-210 to thermal neutrons. As the strain rate increases the unaged loss modulus increases at a higher

proportion to the storage modulus. The neutron aged samples have an inverse relationship, due to chain scission and crosslinking of coupons from the radiation.

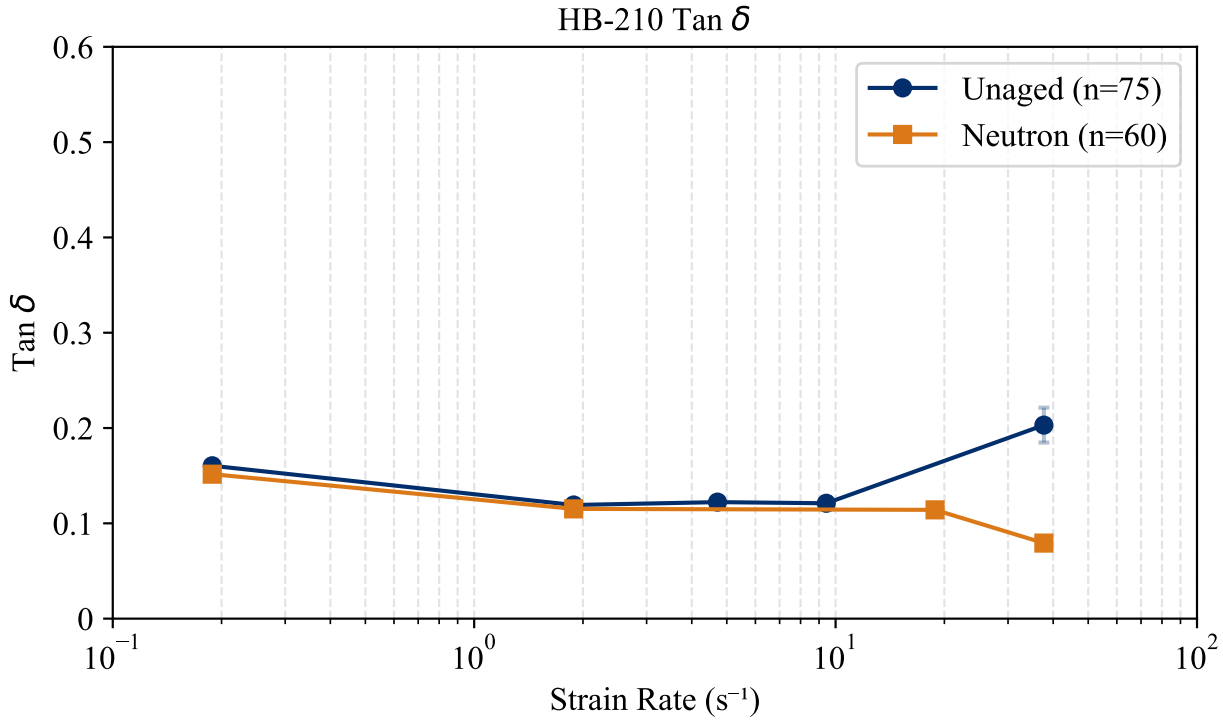

Figure 7.22: Mean tan δ over strain rate of HB-210 $[0/90]_2$ after exposure to thermal neutrons.

The storage modulus of HB-210 after exposure to thermal neutron aging is shown in Figure 7.23. The HB-210 follows the trend of an increasing storage modulus over the strain rates presented, in a linear fashion. The neutron aging appears to double the storage modulus response at 30°C over strain rates 1.9x10^{-1} (s^{-1}) to 3.8x10^{1} (s^{-1}). The neutron aged samples felt less flexible and more brittle after removing from the reactor. The opacity of the matrix deepened from the neutron aging as well. Unfortunately, this deepening in color was not able to be detected on camera due to the reflection. The color change was not as pronounced as the 100 kGy γ aged samples, suggesting less crosslinking. The crystallinity and molecular weight was not tested to confirm this hypothesis. These visual and kinetic cues are indicators that verify the storage modulus is higher likely from crosslinking in both the fibers and matrix.

In addition to the neutrons, this experiment had an elevated temperature, which has the potential to relax the chains and form more entanglements that can contribute to a higher storage modulus.

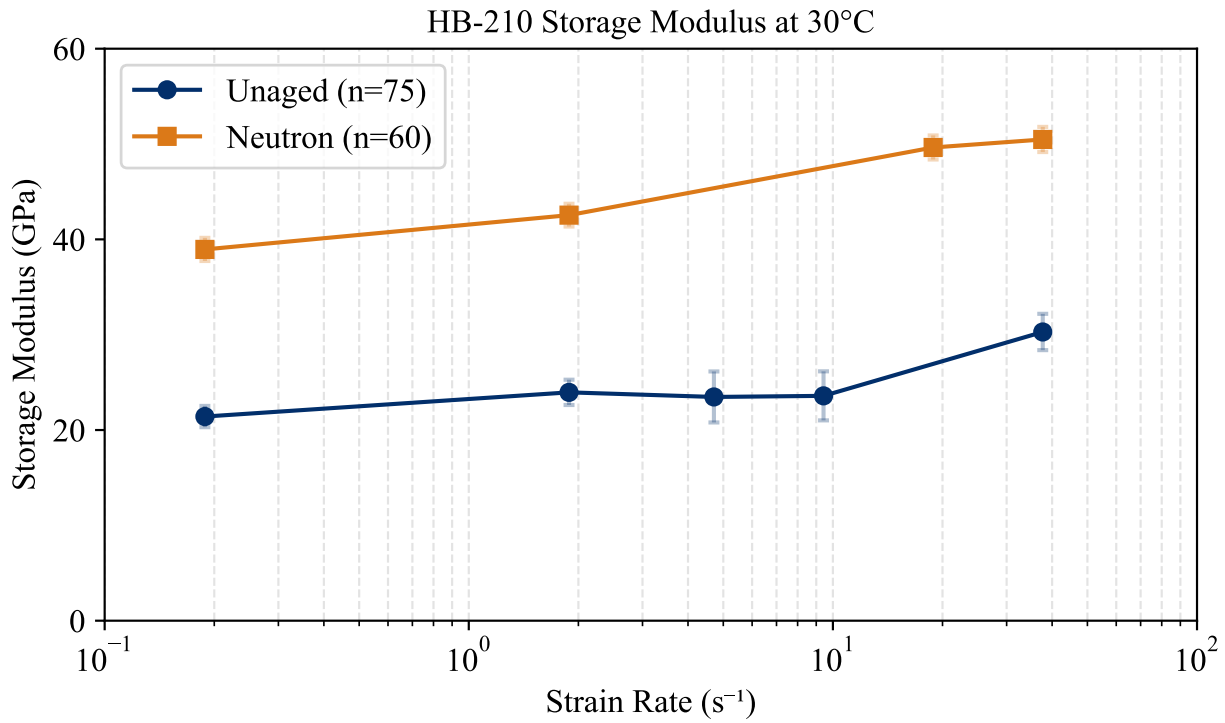

Figure 7.23: Mean storage modulus over strain rate of HB-210 $[0/90]_2$ after exposure to thermal neutrons.

The loss modulus after neutron aging of HB-210 is shown in Figure 7.24. It is important to note, that the neutron source also had an elevated temperature that could have increased the amount of amorphous phases in the UHMWPE, explaining the increase in loss modulus at the lower strain rates. However, the unaged and neutron aged HB-210 loss modulus converges in strain rates above $1.9\text{x}10^1$ (s^{-1}), which is expected as the strain rate increases for the unaged to have a higher loss modulus response.

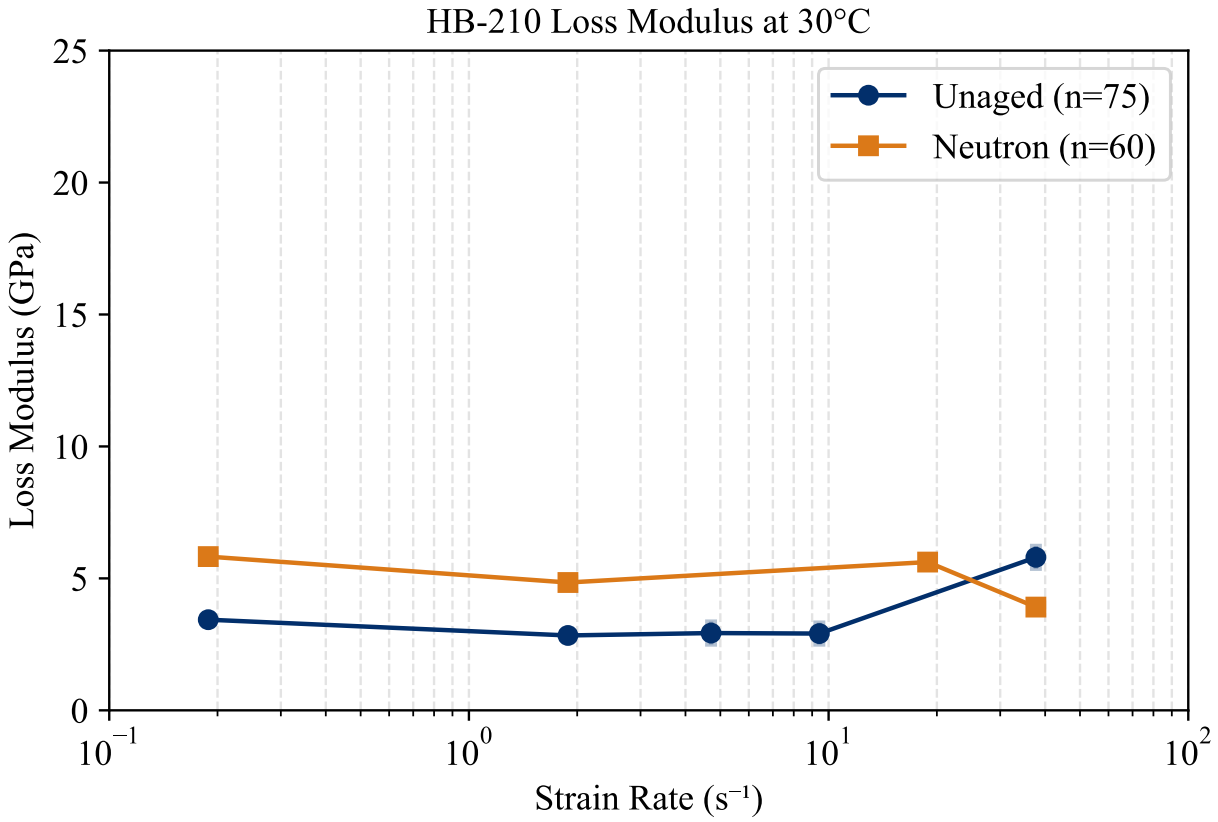

Figure 7.24: Mean loss modulus over strain rate of HB-210 $[0/90]_2$ after exposure to thermal neutrons.

HB-212 Neutron Exposure

Figure 7.25 is the average tan δ response of HB-212 to thermal neutron aging. As the neutron line has a higher tan δ response for strain rates below 1.9x10^{1} (s^{-1}), the neutron aging causes HB-212 to have a higher viscous response.

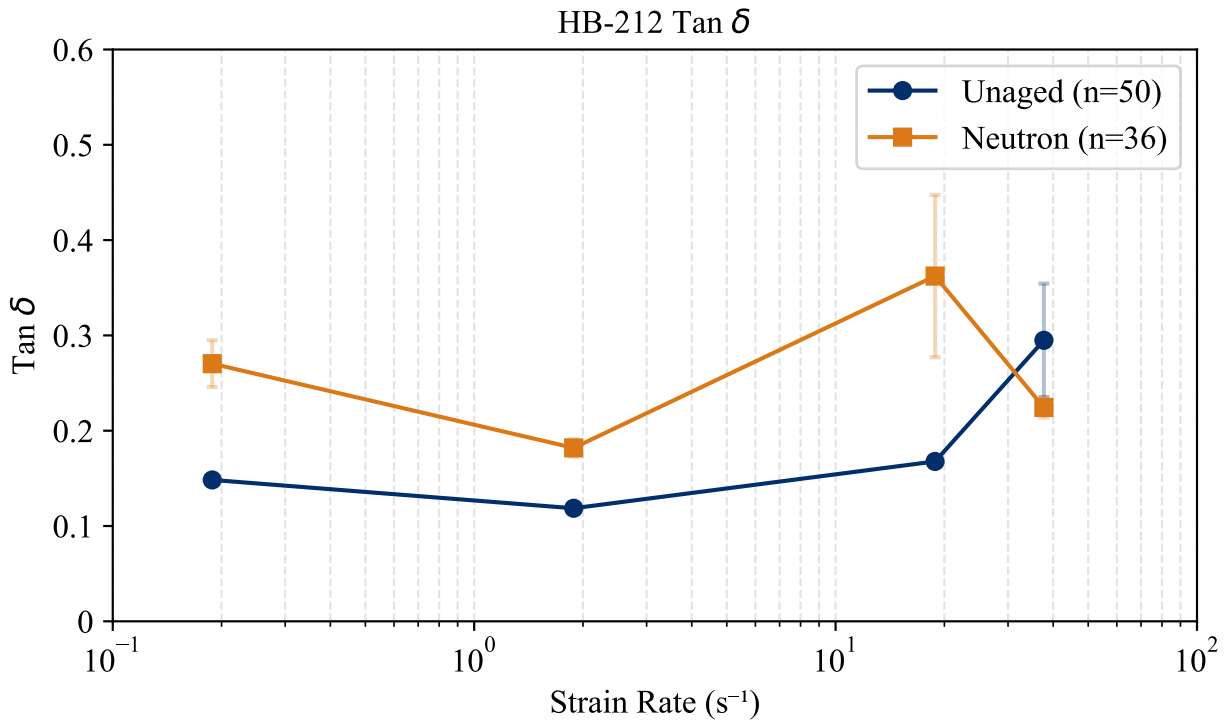

Figure 7.25: Mean tan δ over strain rate of HB-212 $[0/90]_2$ after exposure to thermal neutrons.

Figure 7.26 shows the average storage modulus response of HB-212 after neutron aging. Both the unaged and neutron aged composites follow the same trend across the strain rates. The HB-212's storage modulus after neutron aging is on average 30% higher which is likely due to crosslinking and increasing the number of chain entanglements.

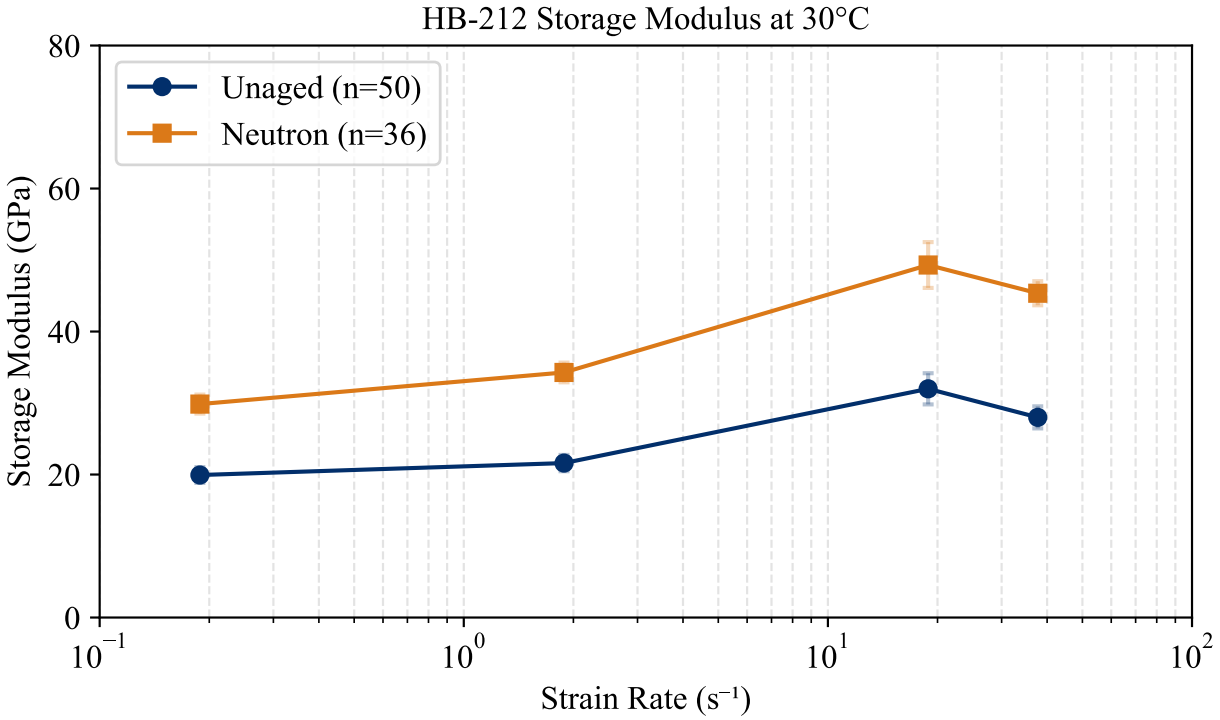

Figure 7.26: Mean storage modulus over strain rate of HB-212 $[0/90]_2$ after exposure to thermal neutrons.

The loss modulus response of HB-212 after neutron aging is shown in Figure 7.27. The neutron aged samples have a higher loss modulus response compared to the unaged HB-212. They appear to be trending towards an intersection at higher strain rates like the HB-210 did, however the DMA began to experience a stochastic resonance at a strain rate of 1.9x10^{1} (s^{-1}) during the neutron tests which is reflected in the loss modulus spike and increased range of the 95% confidence interval.

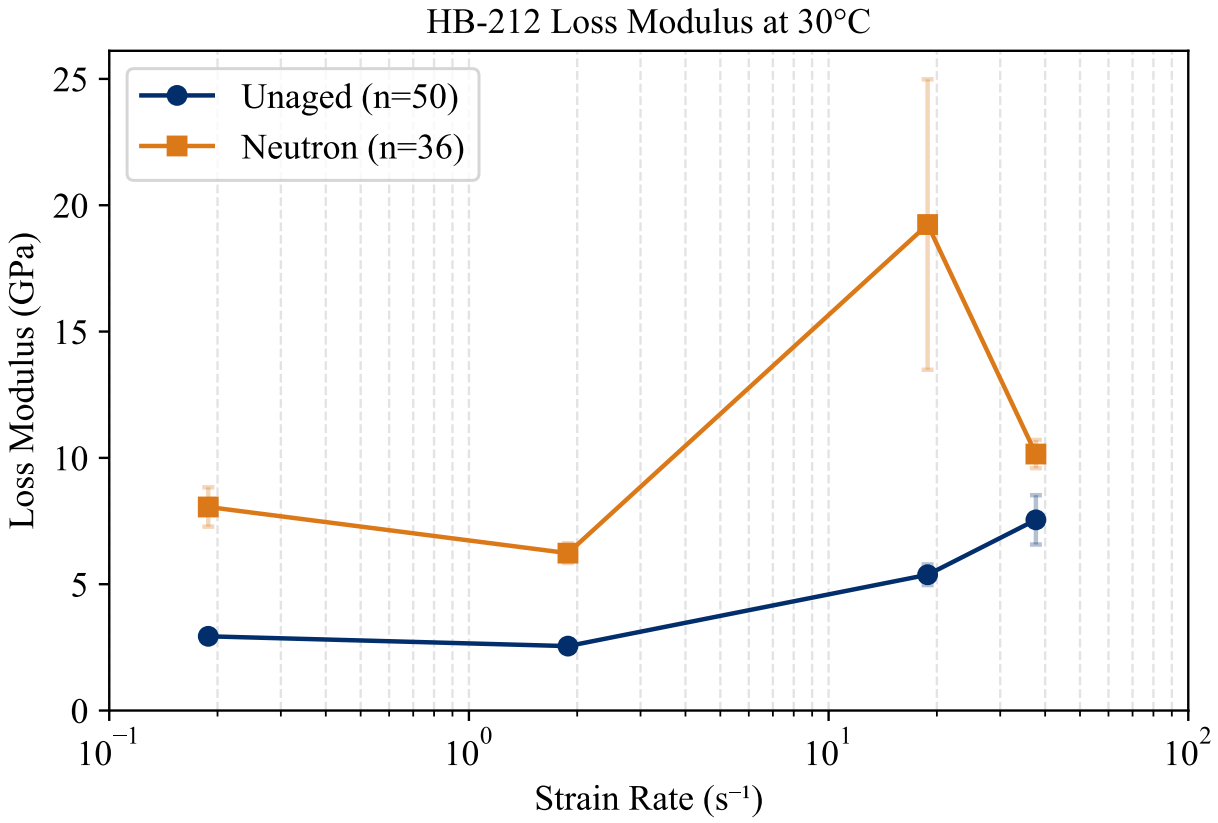

Figure 7.27: Mean loss modulus over strain rate of HB-212 $[0/90]_2$ after exposure to thermal neutrons.

SR-5241 Neutron Exposure

The tan δ response of SR-5241 after neutron aging is shown in Figure 7.28. For strain rates below 1x10^{0} (s^{-1}), both the unaged and neutron aged SR-5241 coupons have the same

proportion of viscous to elastic response. Both sets of coupons follow the same trend of tan δ response at the higher strain rates, however the neutron aged SR-5241 has twice the tan δ response at a strain rate of $1.9x10^{1}$ (s^{-1}), before decreasing below the unaged at a strain rate of $3.8x10^{1}$ (s^{-1}).

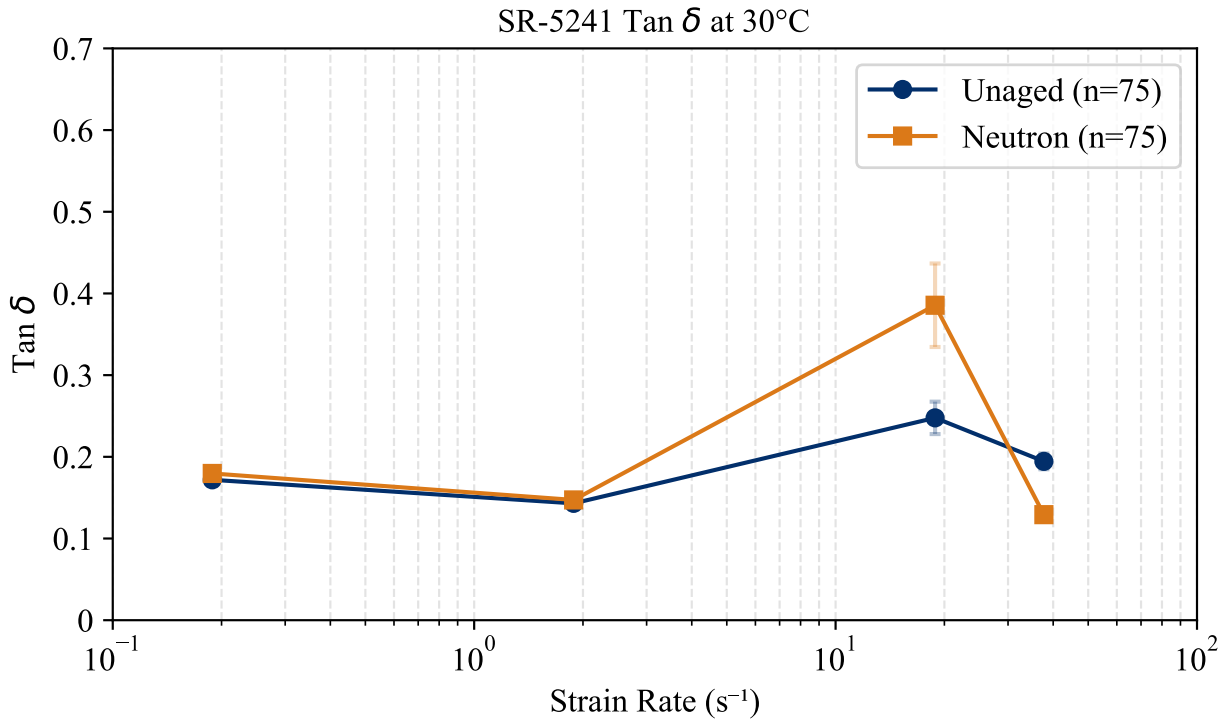

Figure 7.28: Mean tan δ over strain rate of SR-5241 $[0/90]_2$ after exposure to thermal neutrons.

Figure 7.29 is the isothermal storage modulus response of SR-5241 after exposure to neutrons. The neutron aged SR-5241 has on average twice the storage modulus response compared to the unaged. This increased storage modulus is due to the neutrons causing chain scission in the polymer leading to increased formation of crosslinks.

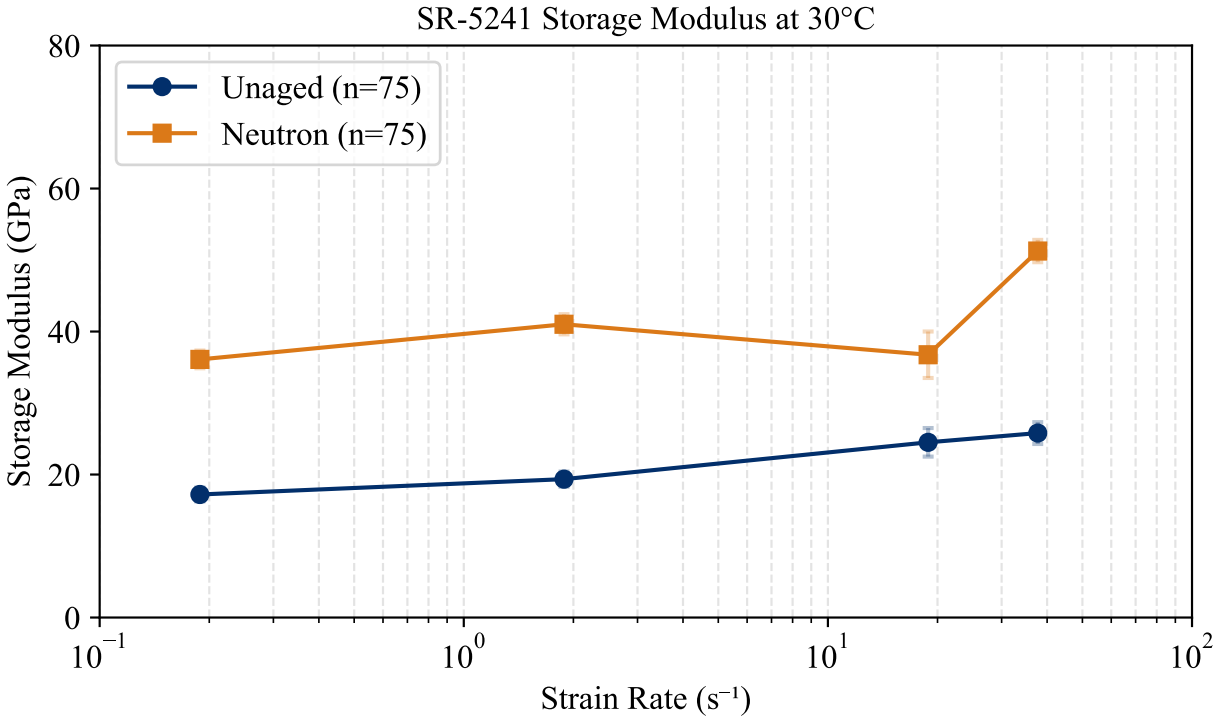

Figure 7.29: Mean storage modulus over strain rate of SR-5241 $[0/90]_2$ after exposure to thermal neutrons.

The loss modulus of SR-5241 after neutron aging is shown in Figure 7.30. The neutron aged SR-5241 loss modulus is on average 110% higher than the unaged for strain rates up to $1.9x10^{1}$ (s^{-1}). The increase in the loss modulus after neutron aging is in part due to the embrittling of the UHMWPE composite. As the polymer forms more crosslinks, the strain to failure decreases as the modulus increases. This increase in modulus can also result in not only a higher loss modulus but also an increased storage modulus. Additionally, this increase in the loss modulus could be from the increased temperature during neutron aging that led to more amorphous phases after cooling back to room temperature.

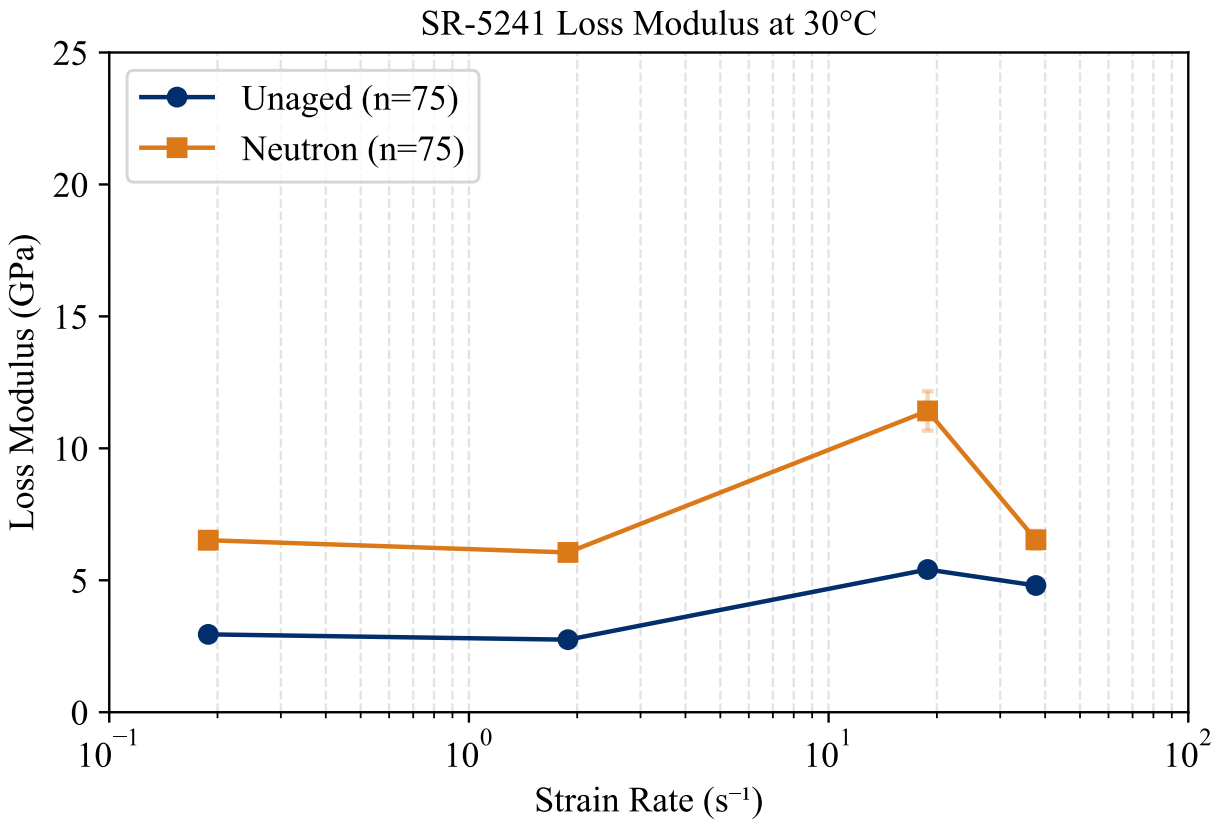

Figure 7.30: Mean loss modulus over strain rate of SR-5241 $[0/90]_2$ after exposure to thermal neutrons.

Neutron Aging Comparison

The HB-210 and HB-212 UHMWPE composites have the same fiber type, Dyneema® SK-99, which is a gel-spun fiber dissolved in decalin to allow for a higher DR. They differ in the consolidation material, HB-210 has a polyurethane rubber (PUR) matrix and HB-212 has a Kraton® synthetic rubber. The SR-5241, has a similar PUR matrix as the HB-210, but a different type of gel-spinning fiber process by dissolving the UHMWPE in a paraffin before spinning, resulting in a lower DR. A comparison of the storage modulus response of HB-210, HB-212, and SR-5241 after exposure to neutrons is shown in Figure 7.31. The PUR matrix composites have a larger storage modulus response to neutron aging compared to the synthetic rubber matrix UHMWPE composite, with the exception of strain rates around $1.9x10^{1}$ (s^{-1}). However, as discussed previously the DMA has a stochastic resonance that appears around this strain rate impacting the tests. The composites are expected to increase in storage modulus along the linear trend presented across the strain rates.

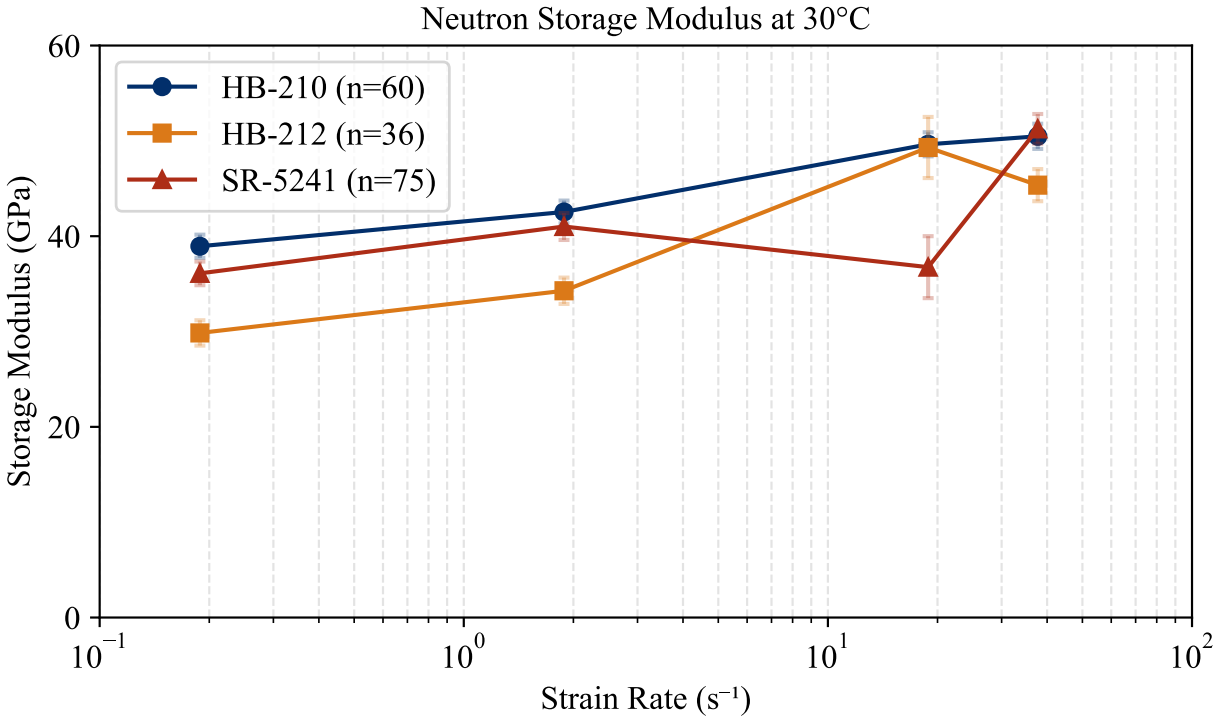

Figure 7.31: Comparison of the mean storage modulus over strain rate after exposure to thermal neutrons.

Comparison of the viscous component of the modulus response of single layer UHMWPE composites after neutron aging is shown in Figure 7.32. The synthetic rubber matrix composite, HB-212, has a higher loss modulus response compared to the PUR matrix composites. This translates to a lower back face deformation (BFD) at higher strain rates.

The matrix selection has trade-offs on how the material ages and performs after neutron radiation exposure as seen by the inverse relationship between the storage and loss modulus aging response in Figure 7.31 and Figure 7.32, where the HB-212 has the lowest storage modulus response but the highest loss modulus response over the strain rates presented. Conversely, the HB-210, which has the same fiber but different matrix has a higher storage modulus and lower loss modulus after neutron aging.

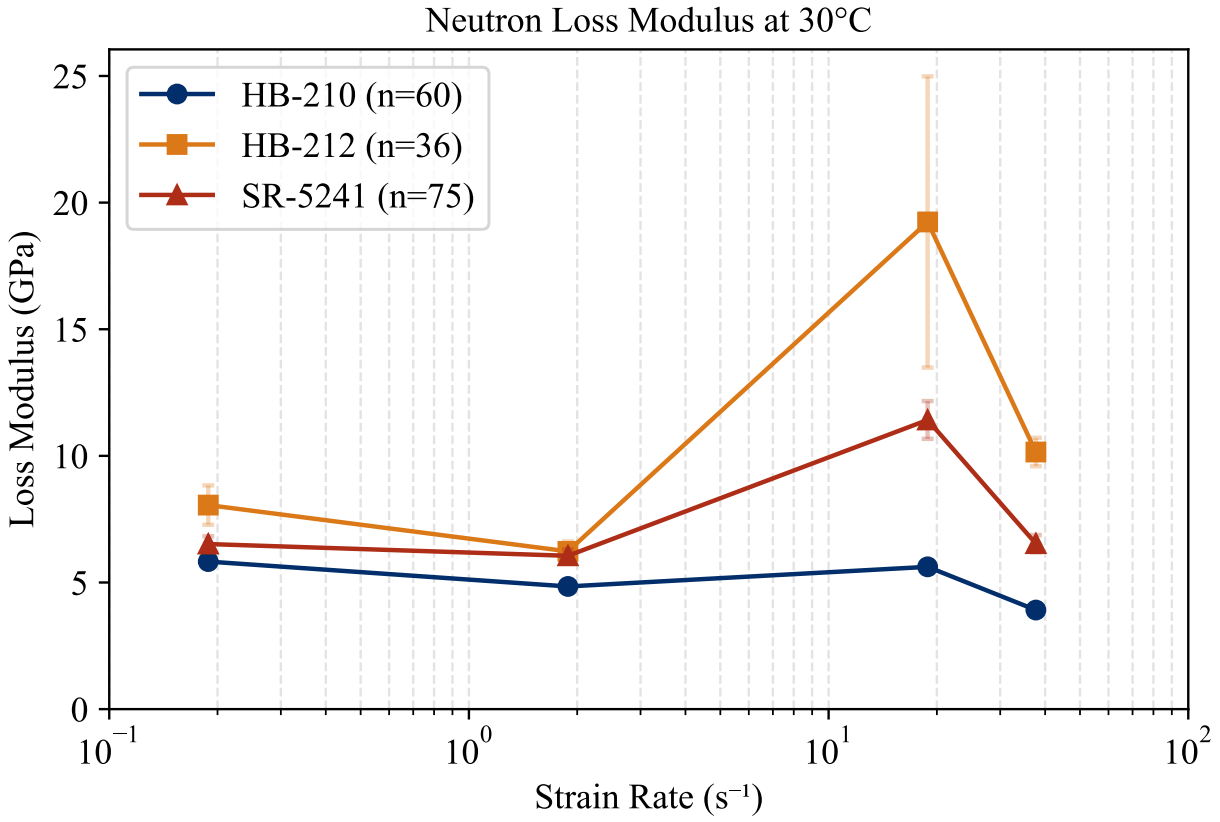

Figure 7.32: Comparison of the mean loss modulus over strain rate after exposure to thermal neutrons.

CONCLUSIONS

This study characterized the thermomechanical viscoelastic response of UHMWPE fiber reinforced composites after exposure to extreme environments. These environmental conditions were informed by previous use cases and predicted use cases through collaborations with suppliers, end users, scientists, and other government agencies. The findings indicated that the degradation of the matrix material after aging has a significant effect on the viscoelastic performance of the composite.

As UHMWPE fiber reinforced composites are often used in marine applications, submersion in both simulated sea water (ASTM salt water) and distilled water lead to an increase in the weight of the composites as the matrix degraded and absorbed water through hydrolysis. Distilled water aged samples exhibited reduced matrix coverage and contaminants on the matrix surface, while salt water aged samples showed salt crystal deposits on the surface. The 95 layer pressed panel, cut by a waterjet and aged in salt water, displayed interlaminar fungal growth stemming from contamination during manufacturing. However, single layer UHMWPE fiber reinforced composites appeared resilient to fungal growth according to MIL-STD 810H requirements. The susceptibility of the matrix material to hydrolysis diminishes the material's lifespan by affecting the fiber-matrix bond. Scanning Electron Microscopy (SEM) analysis corroborates this phenomenon, revealing more pronounced degradation in surface morphology the rubber matrix of HB-212 than in the PUR matrix of HB-210.

UV aging significantly affects the mechanical and optical properties of UHMWPE composites, causing them to become brittle and yellow over time through chain scission and crosslinking. The extent of alteration varies among different matrix materials, with synthetic rubber more affected than PUR. Evidence of this includes a color change in the rubber matrix from white to yellow to brown, ultimately leading to the matrix's disintegration under

prolonged UV exposure. The synthetic rubber matrix aged faster than the PUR during the combined UV, hygrothermal, and temperature cycling tests.

Isolating the effects of UV-A photons from temperature cycling and humidity indicates that hygrothermal aging can initially increase the elastic component of the modulus. However, as the temperature approaches the melting point of polyethylene, the elastic component decreases to levels similar to the unaged material. UV and hygrothermal aging negatively affect the material's ability to recover from strain, suggesting an increase in viscous behavior with age. Dry temperature cycling appears to have a less detrimental effect on the material's creep and recovery compliance.

During both the hygrothermal cyclical aging and the combined UV cycling exposure, the complex modulus increases. This rise in modulus comes at the cost of a decreased toughness as the material becomes more brittle. This combined UV cycling aging eventually leads to matrix dissolution and the fibers are left bare. X-ray aging slightly increased the complex modulus over the doses tested, but did not result in a color change of the matrix. The 100 kGy γ-ray dose induces brittleness and yellowing in both PUR and rubber matrix fiber reinforced composites. While the magnitude of the loss and storage modulus response after radiation aging varies, the trend of ionizing radiation increases both the loss and storage modulus response. This increased moduli response does arise from the material behaving non-linear viscoelastically and decreasing the toughness as stiffness increases for the strain rates investigated.

This work directly assists in the development of both engineering and analytical models for design of ballistic protection systems through collaborations with Los Alamos National Laboratory (LANL) and Pennsylvania State University. The strain rates tested fit the gaps between work conducted at Pennsylvania State with a miniature Kolsky Bar and the rates tested at LANL. The characterization methodology on both the dynamic and quasi-static rates will assist the future work by standardizing this testing methodology. The aging studies

on the UHMWPE fiber reinforced composites provide valuable insights to determine the strengths and vulnerabilities of this composite to various use environments.

FUTURE WORK

As science is a process with no end, there are numerous experiments that will assist the characterization of both aged and unaged mechanical properties of UHMWPE fiber reinforced composites. The lowest hanging fruit begins with basic polymer science. Characterization of the molecular weight and the crystallization will also be of great value to determine the degree these material properties influence the viscoelastic response after aging.

Applying composite theory will provide great insights into how to improve the performance of these UHMWPE fiber reinforced composites, such as conducting studies on various fiber layups for creating better body armor. In personal body armor protection, these plates are often formed with a die press to have a radius of curvature through a large die press. Creating non-symmetric layups could both eliminate this costly manufacturing step and reduce back face deformation. Determining the fiber and matrix material properties after aging will be a great next step in this research.

Additional aging studies of these composites is necessary to ensure the safety and reliability in the field of ballistics protection. For example, soaking in various fuel blends, diesel, unleaded, and jet fuel, before characterizing the composite integrity would be a logical next step. Determining the concentration and duration of the life of these composites after soaking will determine how long and where these composites can be used in vehicle reinforcement. Moreover, evaluating additional temperature ranges that correspond to the UHMWPE fiber-reinforced polyethylene's temperature sensitivities, including cycles above the melting temperature and subsequent cooling to inform the recrystallization. Increasing the scope of radiation dose levels will delineate the material's limits post-exposure. It is also critical to study radiation transmission through the composite to determine the absorbed dose, which will be instrumental in defining safe thicknesses for radiation shielding.

Incorporating ceramic particles, such as boron carbide, into the matrix may serve a dual purpose: enhancing radiation absorption and impeding penetrators. Exploring the integration of additional materials to increase the impedance mismatch between layers could further improve performance. As mentioned in Chapter 2, UHMWPE can be made from powder compaction. This manufacturing methodology eliminates the weak fiber-matrix bond. This material warrants further study for aging and viscoelastic performance, as this study proved the matrix is most vulnerable to aging.

Broadening these experiments to encompass multiple layers will benefit the scientific community at large. Future research should also include modeling efforts to reduce testing costs, offering substantial value to designers and end-users of UHMWPE composites. Lastly, it is crucial to test the aged material under ballistic strain rates to assess the performance of aged composites in real-world applications.

REFERENCES CITED

[1] L. H. (Leslie Howard) Sperling. *Introduction to Physical Polymer Science*. Wiley, Hoboken, N.J, 4th ed. edition, 2006. ISBN 1-119-10374-6.

[2] U. Heisserer, Ahead Material, K. Harrison, D. Cunningham, M. Bults, H. Van Der Werff, M. Jongedijk, M. Van Es, N. Eussen, J. Elburg, W. Roovers, R. Schielen, R. Marissen, P. Douven, V. Widdershoven, R. Jensz, P. Engelen, M. Bulters, J. Stolk, T. Engels, and J. Goossens. Tensile properties of Dyneema ® HB plies Project : To :. Technical report, Material Science Center, 2011.

[3] Ramon van Rooij and Jonmichael Weaver. Teijin and Endumax, Author Conducted Interview, November 2022.

[4] L. H. Sperling. *Introduction to Physical Polymer Science*. Wiley, New York, 2nd ed edition, 1992. ISBN 978-0-471-53035-0.

[5] Bor Z. Jang. *Advanced Polymer Composites*. ASM International, Materials Park, OH, 1994. ISBN 978-0-87170-491-7.

[6] H. Van Der Werff and U. Heisserer. High-performance ballistic fibers. In *Advanced Fibrous Composite Materials for Ballistic Protection*, pages 71–107. Elsevier, 2016. ISBN 978-1-78242-461-1. doi: 10.1016/B978-1-78242-461-1.00003-0.

[7] Winfried Bott, Bob Fifield, and Pieter Jan Lemstra. Chapter 2: High-performance fibers and tapes based on PP and PE. *Advanced Industrial and Engineering Polymer Research*, 5(2):60–69, April 2022. ISSN 25425048. doi: 10.1016/j.aiepr.2022.03.005.

[8] Johan Verbeek and Lisa van den Berg. Recent Developments in Thermo-Mechanical Processing of Proteinous Bioplastics. *Recent Patents on Materials Science*, 200, November 2009. doi: 10.2174/1874464810902030171.

[9] N. G. McCrum, C. P. Buckley, and C. B. Bucknall. *Principles of Polymer Engineering*. Oxford University Press, Oxford [Oxfordshire] ; New York, 1988. ISBN 978-0-19-856152-1 978-0-19-856155-2.

[10] Wangxuan Zhang, Xiaofei Jing, Yanqiang Bai, Xiaoming Shan, Xiaoyu Qi, Maoxin Yan, and Zhongyu Cui. Study on the Aging Behavior of an Ultra-High Molecular Weight Polyethylene Fiber Barrier Net in a Marine Environment. *Materials*, 15(16): 5599, January 2022. ISSN 1996-1944. doi: 10.3390/ma15165599.

[11] Corrosion of polymers. https://www.grindex.com/en-us/, 2024.

[12] Tetsuo Kanamoto, Akeharu Tsuruta, Koji Tanaka, Masatami Takeda, and Roger S. Porter. Superdrawing of Ultrahigh Molecular Weight Polyethylene. 1. Effect of Techniques on Drawing of Single Crystal Mats. *Macromolecules*, 21:470–477, 1988.

[13] Thamer Sabri M. Rawah. *Variability in UHMWPE Gel Spinning*. PhD thesis, Drexel University, 2019.

[14] Lorenzo Iannucci, Stefano Del Rosso, Paul T. Curtis, Dan J. Pope, and Phillip W. Duke. Understanding the thickness effect on the tensile strength property of Dyneema®HB26 laminates. *Materials*, 11(8), 2018. ISSN 19961944. doi: 10.3390/ma11081431.

[15] Pieter Jan Lemstra. Chapter 1: High-performance polyethylene fibers. *Advanced Industrial and Engineering Polymer Research*, 5(2):49–59, April 2022. ISSN 2542-5048. doi: 10.1016/j.aiepr.2022.03.001.

[16] Matthew Hudspeth, Xu Nie, and Weinong Chen. Dynamic failure of Dyneema SK76 single fibers under biaxial shear/tension. *Polymer*, 53(24):5568–5574, November 2012. ISSN 0032-3861. doi: 10.1016/j.polymer.2012.09.020.

[17] A. N. Ozerin, E. K. Golubev, S. S. Ivanchev, V. A. Aulov, A. S. Kechek'yan, T. S. Kurkin, E. M. Ivan'kova, and N. Yu. Adonin. Reactor Powders of Ultra-high Molecular Weight Polyethylene for Solid-state Processing into High-strength Materials and Products. *Polymer Science, Series A*, 64(2):73–83, April 2022. ISSN 0965-545X, 1555-6107. doi: 10.1134/S0965545X22020067.

[18] Teijin. Teijin - Edumax Twaron Brochure. Technical report, Teijin Aramid, 2023.

[19] J. Singletary and B. Lauke. 13 - Polyolefin film–reinforced composites for personal protection. In X. Chen, editor, *Advanced Fibrous Composite Materials for Ballistic Protection*, pages 389–408. Woodhead Publishing, January 2016. ISBN 978-1-78242-461-1. doi: 10.1016/B978-1-78242-461-1.00013-3.

[20] Paul Smith, Henri D. Chanzy, and Bruno P. Rotzinger. Drawing of virgin ultrahigh molecular weight polyethylene: An alternative route to high strength/high modulus materials: Part 2 Influence of polymerization temperature. *Journal of Materials Science*, 22(2):523–531, February 1987. ISSN 0022-2461, 1573-4803. doi: 10.1007/BF01160764.

[21] S. S. Ivanchev, E. I. Ruppel', and A. N. Ozerin. Optimization of the conditions of ethylene polymerization into reactor powders of ultra-high-molecular-weight polyethylene suitable for solid-phase formation into oriented ultra-high-strength and ultra-high-modulus film yarns. *Doklady Physical Chemistry*, 468(2):89–92, June 2016. ISSN 1608-3121. doi: 10.1134/S0012501616060026.

[22] A. N. Ozerin, S. S. Ivanchev, S. N. Chvalun, V. A. Aulov, N. I. Ivancheva, and N. F. Bakeev. Properties of oriented film tapes prepared via solid-state processing of a nascent ultrahigh-molecular-weight polyethylene reactor powder synthesized with a postmetallocene catalyst. *Polymer Science Series A*, 54(12):950–954, December 2012. ISSN 1555-6107. doi: 10.1134/S0965545X12100033.

[23] Oleg V. Lebedev, Alexander N. Ozerin, Alexander S. Kechek'yan, Vitaly G. Shevchenko, Tikhon S. Kurkin, Evgeny K. Golubev, Evgeny A. Karpushkin, and Vladimir G. Sergeyev. A study of oriented conductive composites with segregated network structure obtained via solid-state processing of UHMWPE reactor powder and carbon nanofillers.

Polymer Composites, 40(S1), January 2019. ISSN 0272-8397, 1548-0569. doi: 10.1002/pc.24532.

[24] G. H. Michler, V. Seydewitz, M. Buschnakowski, L. P. Myasnikowa, E. M. Ivan'kova, V. A. Marikhin, Y. M. Boiko, and S. Goerlitz. Correlation among powder morphology, compactability, and mechanical properties of consolidated nascent UHMWPE. *Journal of Applied Polymer Science*, 118(2):866–875, October 2010. ISSN 0021-8995, 1097-4628. doi: 10.1002/app.32346.

[25] Sanjay Rastogi, Yefeng Yao, Sara Ronca, Johan Bos, and Joris van der Eem. Unprecedented High-Modulus High-Strength Tapes and Films of Ultrahigh Molecular Weight Polyethylene via Solvent-Free Route. *Macromolecules*, 44(14):5558–5568, July 2011. ISSN 0024-9297. doi: 10.1021/ma200667m.

[26] Sara Ronca, Giuseppe Forte, Hendrik Tjaden, and Sanjay Rastogi. Solvent-Free Solid-State-Processed Tapes of Ultrahigh-Molecular-Weight Polyethylene: Influence of Molar Mass and Molar Mass Distribution on the Tensile Properties. *Industrial & Engineering Chemistry Research*, 54(30):7373–7381, August 2015. ISSN 0888-5885, 1520-5045. doi: 10.1021/acs.iecr.5b01469.

[27] Crandall Turner. Dyneema® Launches New Website and Brand Identity, Showcasing the Strengths It Brings to Its Value Chain | Avient. https://www.avient.com/news/dyneema-launches-new-website-and-brand-identity-showcasing-strengths-it-brings-its-value-chain, January 2024.

[28] DSM. Ultra High Molecular Weight Polyethylene Fiber from DSM Dyneema, January 2017.

[29] Instagram: @thedyneemaproject. https://www.instagram.com/thedyneemaproject/, 2024.

[30] Ballistic Vest Inserts and Shields. https://www.dyneema.com/sectors/law-enforcement-and-military/ballistic-vest-inserts-and-shields/, 2024.

[31] Avient Corporation. Avient Announces Agreement to Acquire DSM Protective Materials (Dyneema®). https://www.prnewswire.com/news-releases/avient-announces-agreement-to-acquire-dsm-protective-materials-dyneema-and-plans-to-explore-sale-of-distribution-301528666.html, April 2022.

[32] About Us. https://www.dyneema.com/experience-more/about-us/, 2024.

[33] Mike Klasco. Endumax from Teijin Aramid - An Exciting New Speaker Cone Material. https://audioxpress.com/article/Endumax-from-Teijin-Aramid-An-Exciting-New-Speaker-Cone-Material, February 2015.

[34] Michael Buckstein and Zeeuw, Hendrik de. Announcing the Purchase of Endumax. http://www.barrday.com/blogs/barrday-purchase-of-endumax-assets-from-teijin.htm, July 2023.

[35] HD Tech. News: Information and development peers. https://www.huidunuhmwpe.com/news/information-and-development-peers/, September 2022.

[36] Product. http://www.sinopecgroup.com, 2024.

[37] High-strength High-modulus PE Fiber Production Line. https://www.shenhe-technology.com/high-strength-high-modulus-pe-fiber-production-line-15820069168008730.html, 2024.

[38] Claudia H. Deutsch and Laura M. Holson. Allied Signal And Honeywell To Announce Merger Today. *The New York Times*, June 1999. ISSN 0362-4331.

[39] BAE to Acquire Armor Holdings for $4.53B - Defense Industry Daily, 2024.

[40] Cal Biesecker. DuPont Plans To Acquire Assets of BAE Systems' Tensylon; Aims Toward New Armor Materials. https://www.defensedaily.com/dupont-plans-to-acquire-assets-of-baesystems-tensylon-aims-toward-new-armor-materials/business-financial/, June 2012.

[41] Pieter Jan Lemstra. Epilogue. *Advanced Industrial and Engineering Polymer Research*, 5(2):133–135, April 2022. ISSN 25425048. doi: 10.1016/j.aiepr.2022.04.003.

[42] Ryan Jordan. Dyneema, Cuben Fiber, and the Future of Outdoor Gear. https://backpackinglight.com/cuben-fiber-dyneema-ultralight-film-outdoor-gear-apparel-cottage/, January 2016.

[43] Maquita Peters. Skydiver Luke Aikins Sets Record For Highest Jump Without Parachute. *NPR*, July 2016.

[44] Changsheng Dong, Yang Yang, Mingliang Huo, Jinliang Li, and Haidong Wang. Research on the Transmission and Ballistic Resistance Performance of the Ultra-high Molecular Weight Polyethylene Radome. In *Proceedings of the Seventh Asia International Symposium on Mechatronics*, volume 588 of *Lecture Notes in Electrical Engineering*, pages 314–322. Springer Singapore Pte. Limited, Singapore, 2019. ISBN 978-981-329-436-3. doi: 10.1007/978-981-32-9437-0_34.

[45] D. S. M. Dyneema. Product Specification: HB212 Ultra-High Molecular Weight Polyethylene fiber based composite laminate. Technical report, DSM, 2014.

[46] Chad S. Cummings, Eric M. Lucas, Justin A. Marro, Tri M. Kieu, and John D. DesJardins. The effects of proton radiation on UHMWPE material properties for space flight and medical applications. *Advances in Space Research*, 48(10):1572–1577, 2011. ISSN 02731177. doi: 10.1016/j.asr.2011.07.009.

[47] Donruedee Toyen, Ekachai Wimolmala, Narongrit Sombatsompop, Teerasak Markpin, and Kiadtisak Saenboonruang. Sm2O3/UHMWPE composites for radiation shielding applications: Mechanical and dielectric properties under gamma irradiation and thermal neutron shielding. *Radiation Physics and Chemistry*, 164, November 2019. ISSN 18790895. doi: 10.1016/j.radphyschem.2019.108366.

[48] M. I. Sayyed, Alyaa H. Abdalsalam, Malaa M. Taki, M. H. A. Mhareb, Bünyamin Alim, Ali Baltakesmez, and Erdem Şakar. MoO3 reinforced Ultra high molecular weight PE for neutrons shielding applications. *Radiation Physics and Chemistry*, 172, July 2020. ISSN 18790895. doi: 10.1016/j.radphyschem.2020.108852.

[49] Oussama Mehelli, Mehdi Derradji, Raouf Belgacemi, Slimane Abdous, Abdelmalek Habes, and Wenbin Liu. Outstanding thermal neutrons shields based on epoxy, UHMWPE fibers and boron carbide particles. *Applied Radiation and Isotopes*, 176: 109837, 2021.

[50] Oussama Mehelli, Mehdi Derradji, Raouf Belgacemi, and Slimane Abdous. Development of lightweight and highly efficient fast neutrons composites shields based on epoxy, UHMWPE fibres and boron carbide particles. *Radiation Physics and Chemistry*, 193: 109510, 2022.

[51] Mehdi Derradji, Oussama Mehelli, Raouf Belgacemi, and Slimane Abdous. High Performance Dual Ballistic and Thermal Neutrons Shields From Kevlar Fibers Reinforced Epoxy/B4C Hybrid Composites. *Frontiers in Physics*, 10, February 2022. ISSN 2296-424X. doi: 10.3389/fphy.2022.740673.

[52] Slimane Abdous, Mehdi Derradji, Zineb Mekhalif, Karim Khiari, Oussama Mehelli, and Younes Bourenane Cherif. Advances in Polymeric Neutron Shielding: The Role of Benzoxazine-h-BN Nanocomposites in Nuclear Protection. *Radiation Research*, 200(3): 242–255, 2023.

[53] Ignacio Urrutia. The Arms Race between Morocco and Algeria: A Strategic Assessment, November 2022.

[54] Atalayar. Marruecos aumentará en un 6% su gasto en defensa en 2022. https://www.atalayar.com/en/articulo/politics/morocco-increase-defence-spending-6-2022/20220428132444156195.html, April 2022.

[55] Ifeoluwa Dada. China to invest $36 billion in multi-sectoral projects in Algeria, July 2023.

[56] Chinedu Okafor. China is set to invest $36 billion in some of Algeria's key economic sectors. *Business Insider Africa*, July 2023.

[57] S. Pal Arya. *Introduction to Micrometeorology*, volume 42. Academic Press, 1 edition, 1988. ISBN 978-0-08-095982-5.

[58] Cristina L. Archer and Ken Caldeira. Global assessment of high-altitude wind power. *Energies*, 2(2):307–319, 2009. ISSN 19961073. doi: 10.3390/en20200307.

[59] Uwe Ahrens, Moritz Diehl, and Roland Schmehl. *Green Energy and Technology Airborne Wind Energy*. Springer-Verlab Berlin Heidelberg, 2013.

[60] Massimo Ippolito. KiteGen Research Details. http://www.kitegen.com/en/technology/details/, September 2009.

[61] Giancarlo Abbate and Eugenio Saraceno. What Else is Emerging from the Horizon? In Ahmad Vasel and David S.-K. Ting, editors, *Advances in Sustainable Energy*, pages 177–213. Springer International Publishing, 2019. ISBN 978-3-030-05636-0. doi: 10.1007/978-3-030-05636-0_10.

[62] B. W. Roberts, D. H. Sheapard, K. Caldeira, D. G. Eccles, A. J. Grenier, and J. F. Freidin. Harnessing high-altitude wind power. *IEEE Trans Energy Convers.*, 22:136–144, 2007.

[63] Michel van Pelt. *Space Tethers and Space Elevators*. Springer New York, 1st ed. 2009. edition, 2009. ISBN 1-282-29210-2.

[64] Table of Material Properties: Composite Materials Design. https://sites.google.com/site/compositematerialsdesign/home/table-of-material-properties, 2024.

[65] Tom Crouch. Felix Baumgartner's "Edge of Space" Capsule Goes on Display | Air & Space Magazine| Smithsonian Magazine. *Smithsonian Magazine*, 2014.

[66] William J. Broad. Wreckage in the Desert Was Odd but Not Alien. *The New York Times*, September 1994. ISSN 0362-4331.

[67] Manish Singh. Alphabet shuts down Loon internet balloon company | TechCrunch. https://techcrunch.com/2021/01/21/google-alphabet-is-shutting-down-loon-internet/, January 2021.

[68] Aerostar. Raven Industries Aerostar Flies a New Revolutionary Design.... https://aerostar.com/news/raven-industries-aerostar-flies-a-new-revolutionary-design-for-a-stratospheric-high-altitude-balloon-mission-for-nasa, March 2024.

[69] Kevin Roach. Variable weft webbing for use as superpressure envelope load tendon. Number US9085348B1. Patent US9085348B1, July 2015.

[70] Kevin Roach. Outer membrane for aerial vehicles. Number US11577813B2. Patent US11577813B2, February 2023.

[71] Kevin Roach, Venkata Akula, and Paul Frey. Outer membrane for aerial vehicles. Number US20220185442A1. Patent US20220185442A1, June 2022.

[72] TCOM Holdings Announces Acquisition of Aerostar – TCOM. https://tcomlp.com/tcom-holdings-announces-acquisition-of-aerostar/, July 2022.

[73] Zhaoxiang Liu and Haochen Zhang. Ultra-high molecular weight polyethylene: Preparation and applications. *Journal of Physics: Conference Series*, 2229(1):012006, March 2022. ISSN 1742-6588, 1742-6596. doi: 10.1088/1742-6596/2229/1/012006.

[74] Runlai Li and Ping Gao. Nanoporous UHMWPE Membrane Separators for Safer and High-Power-Density Rechargeable Batteries. *Global Challenges*, 1(4):1700020, July 2017. ISSN 2056-6646, 2056-6646. doi: 10.1002/gch2.201700020.

[75] D. C. Prevorsek and G. Harpell. Ballistic armor from extended chain polyethylene fibers. *Materials–Pathway to the Future*, pages 1685–1696, 1988.

[76] Martin Vlasblom. 18 - The manufacture, properties, and applications of high-strength, high-modulus polyethylene fibers. In Anthony R. Bunsell, editor, *Handbook of Properties of Textile and Technical Fibres (Second Edition)*, The Textile Institute Book Series, pages 699–755. Woodhead Publishing, January 2018. ISBN 978-0-08-101272-7. doi: 10.1016/B978-0-08-101272-7.00018-3.

[77] Paul Cavallaro. Soft Body Armor: An Overview of Materials, Manufacturing, Testing, and Ballistic Impact Dynamics. Technical report, NAVSEA, August 2011.

[78] Peter Weiss, Mohamed Makthoum, Thibaud Gobert, Yann Chouard, Nisheet Singh, Theo Chalal, Sibylle Schmied, Matthias Schweins, Thomas Stegmaier, Götz Gresser, Gernot Groemer, Nina Sejkora, Shumit Das, Riccardo Rampini, and Małgorzata Hołyńska. Advanced Materials for Future Lunar Extravehicular Activity Space Suit. *Advanced Materials Technologies*, 5:2000028, June 2020. doi: 10.1002/admt.202000028.

[79] Ji-Hun Cha, YunHo Kim, Sarath Kumar Sathish Kumar, Chunghyeon Choi, and Chun-Gon Kim. Ultra-high-molecular-weight polyethylene as a hypervelocity impact shielding material for space structures. *Acta Astronautica*, 168:182–190, March 2020. ISSN 0094-5765. doi: 10.1016/j.actaastro.2019.12.008.

[80] Dariush Firouzi, Aya Youssef, Momen Amer, Rami Srouji, Asma Amleh, Daniel A. Foucher, and Habiba Bougherara. A new technique to improve the mechanical and biological performance of ultra high molecular weight polyethylene using a nylon coating. *Journal of the Mechanical Behavior of Biomedical Materials*, 32:198–209, April 2014. ISSN 1751-6161. doi: 10.1016/j.jmbbm.2014.01.001.

[81] Steven M. Kurtz. *UHMWPE Biomaterials Handbook: Ultra High Molecular Weight Polyethylene in Total Joint Replacement and Medical Devices*. Academic Press, April 2009. ISBN 978-0-08-088444-8.

[82] Boundless. 2.25: Synthesis of Biological Macromolecules. https://bio.libretexts.org, 2024.

[83] Ying Li, Zhaowei Chu, Xiaoming Li, Xili Ding, Meng Guo, Haoran Zhao, Jie Yao, Lizhen Wang, Qiang Cai, and Yubo Fan. The effect of mechanical loads on the degradation of aliphatic biodegradable polyesters. *Regenerative Biomaterials*, 4(3):179–190, June 2017. ISSN 2056-3418. doi: 10.1093/rb/rbx009.

[84] Sebastião V. Canevarolo. *Polymer Science: A Textbook for Engineers and Technologists*. Hanser, Munich ; Cincinnati, 2020. ISBN 978-1-56990-725-2.

[85] Rodney Patterson, Andreas Kandelbauer, Uwe Müller, and Herfried Lammer. 17 - Crosslinked Thermoplastics. In Hanna Dodiuk and Sidney H. Goodman, editors, *Handbook of Thermoset Plastics (Third Edition)*, pages 697–737. William Andrew Publishing, Boston, January 2014. ISBN 978-1-4557-3107-7. doi: 10.1016/B978-1-4557-3107-7.00017-8.

[86] Huapeng Zhang, Meiwu Shi, Jianchun Zhang, and Shanyuan Wang. Effects of sunshine UV irradiation on the tensile properties and structure of ultrahigh molecular weight polyethylene fiber. *Journal of Applied Polymer Science*, 89(10):2757–2763, 2003. ISSN 00218995. doi: 10.1002/app.12448.

[87] National Institute of Justice. NIJ Standard–0101.04. *Law Enforcement and Corrections Standards and Testing Program*, page 67, 2000.

[88] R. Sinclair. Chapter 1 - understanding textile fibres and their properties: What is a textile fibre? In Rose Sinclair, editor, *Textiles and Fashion*, Woodhead Publishing Series in Textiles, pages 3–27. Woodhead Publishing, 2015. ISBN 978-1-84569-931-4. doi: 10.1016/B978-1-84569-931-4.00001-5.

[89] H. Van Der Werff and U. Heisserer. High-performance ballistic fibers: Ultra-high molecular weight polyethylene (UHMWPE). *Advanced Fibrous Composite Materials for Ballistic Protection*, pages 71–107, January 2016. doi: 10.1016/B978-1-78242-461-1.00003-0.

[90] James D. Walker and Sidney Chocron. Why Impacted Yarns Break at Lower Speed Than Classical Theory Predicts. *Journal of Applied Mechanics*, 78(051021), August 2011. ISSN 0021-8936. doi: 10.1115/1.4004328.

[91] Philip M. Cunniff. Dimensionless Parameters for Optimization of Textile Based Body Armor Systems Dimensionless Parameters for Optimization of Textile-Based Body Armor Systems, 1999.

[92] Kiho Joo and Tae Jin Kang. Numerical Analysis of Energy Absorption Mechanism in Multi-ply Fabric Impacts. *Textile Research Journal*, 78(7):561–576, July 2008. ISSN 0040-5175. doi: 10.1177/0040517507085194.

[93] L. Iannucci and D. Pope. High velocity impact and armour design. *Express Polymer Letters*, 5(3):262–272, 2011. ISSN 1788618X. doi: 10.3144/expresspolymlett.2011.26.

[94] Valerie A. Martin, Thomas W. Hannah, Steve Ellis, and Reuben H. Kraft. Using the Embedded Element Finite-Element Method to Simulate Impact of Dyneema® Plates. *Fibers and Polymers*, 25(2):619–630, February 2024. ISSN 1875-0052. doi: 10.1007/s12221-023-00417-z.

[95] B. D. Heru Utomo. *High-Speed Impact Modelling and Testing of Dyneema Composite*. PhD thesis, Technische Universiteit Delft, 2011.

[96] Jonas A. Zukas. Preface. In Jonas A. Zukas, editor, *Studies in Applied Mechanics*, volume 49 of *Introduction to Hydrocodes*, pages v–vii. Elsevier, January 2004. doi: 10.1016/S0922-5382(04)80001-1.

[97] K. Harrison, H. Wilms, F. Oosterlinck, T. Engels, and M. Theunisse. Tensile ply tests on FMT materials. Technical report, DSM, 2014.

[98] Julia Cline and Bryan Love. The effect of in-plane shear properties on the ballistic performance of polyethylene composites. *International Journal of Impact Engineering*, 143:103592, September 2020. ISSN 0734-743X. doi: 10.1016/j.ijimpeng.2020.103592.

[99] Thomas W. Hannah. *The Pennsylvania State University*. PhD thesis, Pennsylvania State University, 2023.

APPENDIX

NTS FUNGAL TESTING

National Technical Systems - Baltimore
5 North Park Drive
Hunt Valley, MD 21030

Main: 410-584-9099
Fax: 410-584-9117

Date In: March 24, 2023

Customer:
Montana State University
Mechanical and Industrial Engineering
220 Roberts Hall
Boseman, MT 59717

Purchase Order Number: MIE-RB-421

A. TEST OBJECTIVE:
Determine fungus resistance of submitted samples

B. TEST ITEM(S):
Composite Fabrics Material with Polyethylene Fibers

C. SPECIFICATIONS / METHODS / TECHNIQUES:
1. Fungus Resistance per MIL-STD-810H, Method 508.8

D. RESULTS:
Trace growth observed on Spectra 5241. Trace growth likely due to contamination was observed on Dyneema HB-212. See details starting on Page 5.

TESTING PERFORMED BY:

Katherine C. Higgs
Dept. Manager, Special Projects

David Hillis
Materials Technician II

TECHNICAL/QUALITY APPROVALS:

Daniel D. Phillips
Dept. Manager, FA/Analytical

TEST ITEM IDENTIFICATION

SAMPLE TYPE	Composite Fabrics with Polyethylene Fibers
NUMBER OF SAMPLES SUBMITTED	Four (4)
SAMPLE IDENTIFICATION	1. Dyneema HB-210 2. Dyneema HB-212 (Cloth) 3. Dyneema HB-212 4. Spectra 5241
SAMPLE DISPOSITION	Pending return to client after decontamination

The following images provide an overview of the sample submission:

Dyneema HB-210

Dyneema HB-212 (Cloth)

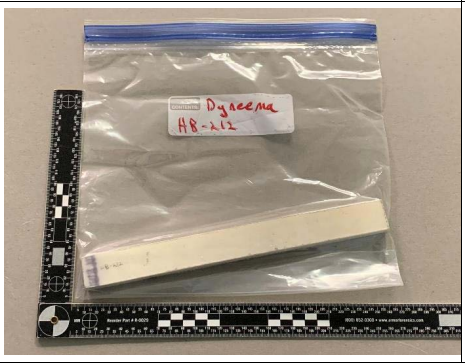

Dyneema HB-212

Spectra 5241

FUNGUS RESISTANCE

REFERENCE	MIL-STD-810H, Method 508.8
TEST SPECIMENS	Four (4) composite fabrics
REQUIREMENT	• Any fungal growth on the test item must be analyzed to determine the species. • Any fungal growth on the test item material(s), whether from the inoculums or other sources, must be evaluated by a qualified personnel for: 1) The extent of growth on susceptible components of materials, using Table 508.8-II as a guide. 2) The immediate effect that the growth has on the physical characteristics of the materiel. 3) The long-range effect that the growth could have on the material. • Evaluate human factors effects (including health risks) • Cleaning solution used if other than water
SUMMARY	**Trace growth observed on Spectra 5241. Trace growth likely due to contamination was observed on Dyneema HB-212. See following pages for details.**
SAMPLE PREPARATION DETAILS	All specimens were placed within a suitable fixture within the test chamber, which had been preconditioned at 30°C and 90-99% relative humidity for at least four (4) hours. The specimens and control were then sprayed with the prepared spore suspension.
SAMPLE PREPARATION PERFORMED BY	KH/DH
PREPARATION DATE	May 25 – June 1, 2023
CONTROL GROWTH VERIFICATION PERFORMED BY	KH/DH
CONTROL GROWTH VERIFICATION DATE	June 8, 2023
TEST MODIFICATIONS	Samples were inspected after 7 days of incubation per customer request
TEST CONDITIONS	30°C and 90-99% RH
TEST PERFORMED BY	KH/DH
TEST DATE	June 1-29, 2023
FUNGUS IDENTIFICATION PERFORMED BY	NTS-Tinton Falls 36 Gilbert St S, Tinton Falls, NJ 07724
IDENTIFICATION DATE	July 5, 2023
EQUIPMENT USED	WC051523, WC051524, WC051628, WC051668, WC051692, WC051740, WC051863, WC051901, WC051902, WC051928, WC051957, WC051961, WC051962, WC052090, WC059253, WC059338, WC059408, WC059409, WC059411, WC061951, WC051500, WC051625

FUNGAL EFFECTS:

Fungi breakdown carbon based molecules to use as a source of nutrients. This molecular degradation can lead to material deterioration which can affect the physical properties. The fungal growth can also act as an electrical bridge over insulating materials resulting in electrical failures. In addition, the fungal growth can restrict movement of small parts or introduce moisture to non-wetting surfaces.

The following table summarizes the fungus used in test and known susceptible materials:

Fungus	Materials Affected
T. virens (TV)	Adhesives, cork, automotive components, electrical insulation, packing materials, plastics, polymers
A. brasiliensis (AB)	Textiles, vinyl, conformal coatings, insulation, leather, etc.
A. flavus (AF)	Leathers, textiles, rubber. Electrical insulation, varnish, wax, packing materials, etc.
T. pinophilus (TP)	Textiles, plastics, cotton fabric, polymers, gaskets, distributors, cables, hoses, PVC, airborne equipment (breakers, solenoids, switches, etc).
C. globosum (CG)	Cellulose and any components containing paper and paper products

The fungi specified for this test are not normally considered a serious hazard for human handling. However, it is possible for an individual to be allergic to one of the species, which is why samples are decontaminated prior to relinquishment.

RESULTS:

The samples were evaluated per MIL-STD-810, which assigns a fungal growth rating based on visual observations after fungal exposure. A summary of the rating system is provided below.

Growth Amount	Rating	Observation
None	0	Substrate is devoid of microbial growth.
Trace	1	Scattered, sparse, or very restricted microbial growth.
Light	2	Intermittent infestations or loosely spread microbial colonies on substrate surface. Includes continuous filamentous growth extending over the entire surface, but underlying surfaces are still visible.
Medium	3	Substantial amount of microbial growth. Substrate may exhibit visible structural change.
Heavy	4	Massive microbial growth.

All fungal species identification is performed as a “best effort” by NTS-Tinton Falls through microscopy images obtained by NTS-Baltimore.

The following table summarizes the growth ratings for each sample after 7 days:

Sample ID	Visual Results	
	Rating	Observations
Dyneema HB-210	0	No apparent fungal growth observed under microscopy. "Minimal" debris noted.
Dyneema HB-212 (Cloth)	0	No apparent fungal growth observed under microscopy. "Moderate" debris noted.
Dyneema HB-212	0	No apparent fungal growth observed under microscopy. "Heavy" debris noted.
Spectra 5241	1	Sporadic fruiting body growth along edge and slightly inward. "Moderate" debris noted.

The following table summarizes the growth ratings for each sample after 28 days:

Sample ID	Visual Results		Species Identified (Best Effort)
	Rating	Observations	
Dyneema HB-210	0	No apparent fungal growth observed under microscopy . "Moderate" debris noted.	N/A
Dyneema HB-212 (Cloth)	0	No apparent fungal growth observed under microscopy. "Heavy" debris noted.	N/A
Dyneema HB-212	0*	*Localized active growth observed on frayed cut edges. These areas were omitted from the rating due to likely contamination. "Heavy" debris noted.	*AB, *AF
Spectra 5241	1	Sporadic fruiting body growth along edge and inward . Growth appears to have spread more from 7 day evaluation. "Moderate" debris noted.	AB, TP, TV

*This sample would be rated as a “1” if the frayed edges were included with the assessment. The species are provided for informational purposes since they are likely a result of contamination due to sample preparation prior to receipt at NTS.

Representative images post-exposure is provided on the following pages.

IMAGES:

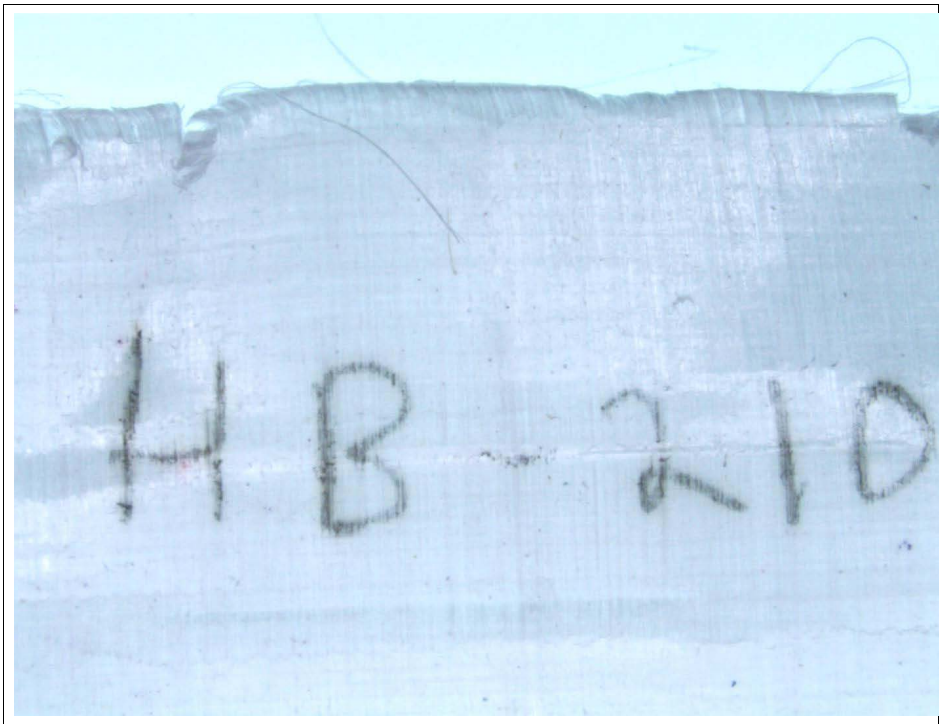

Overview of Dyneema HB-210, Post 28 Days – 7x Magnification

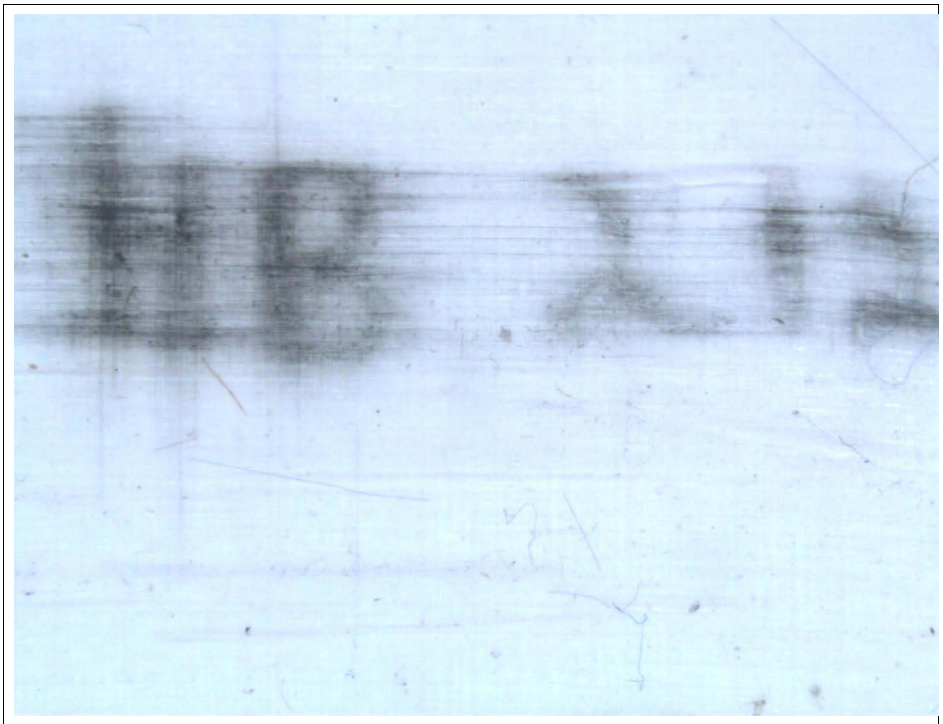

Overview of Dyneema HB-212 (Cloth), Post 28 Days – 7x Magnification

Overview of Dyneema HB-212, Post 28 Days – 8x Magnification

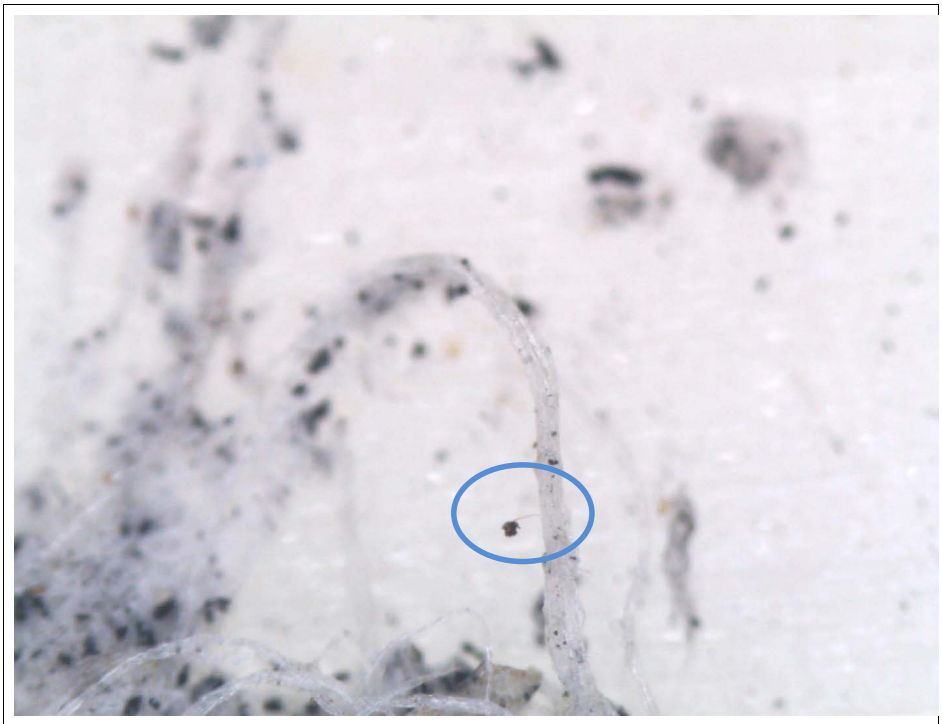

Overview of Dyneema HB-212, Post 28 Days – 50x Magnification
Fungal growth observed on frayed edge

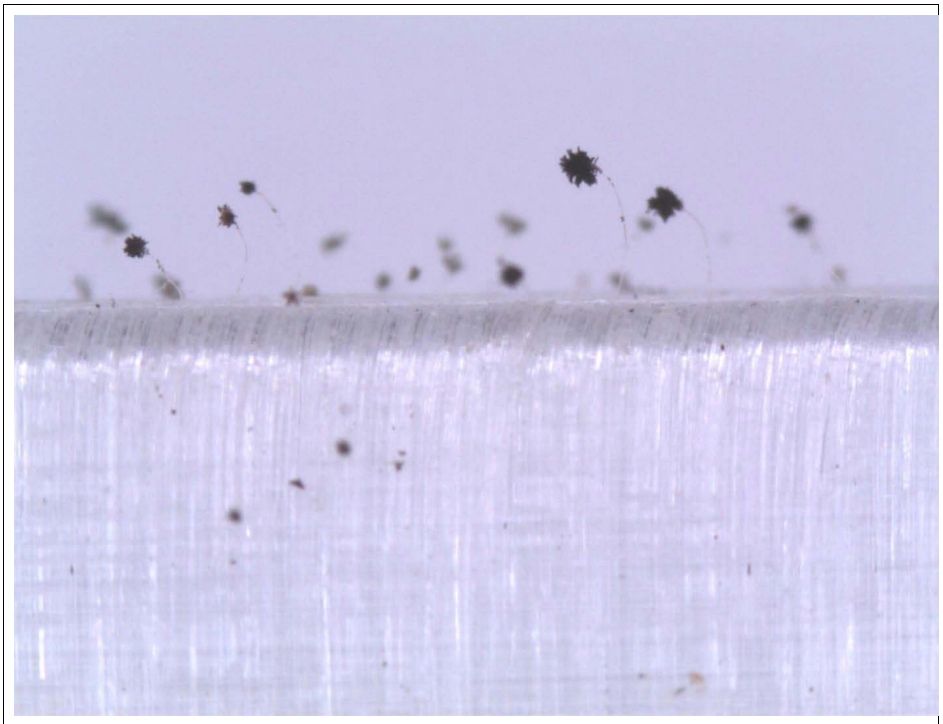

Overview of Spectra 5241, Post 7 Days – 40x Magnification

Overview of Spectra 5241, Post 28 Days – 25x Magnification

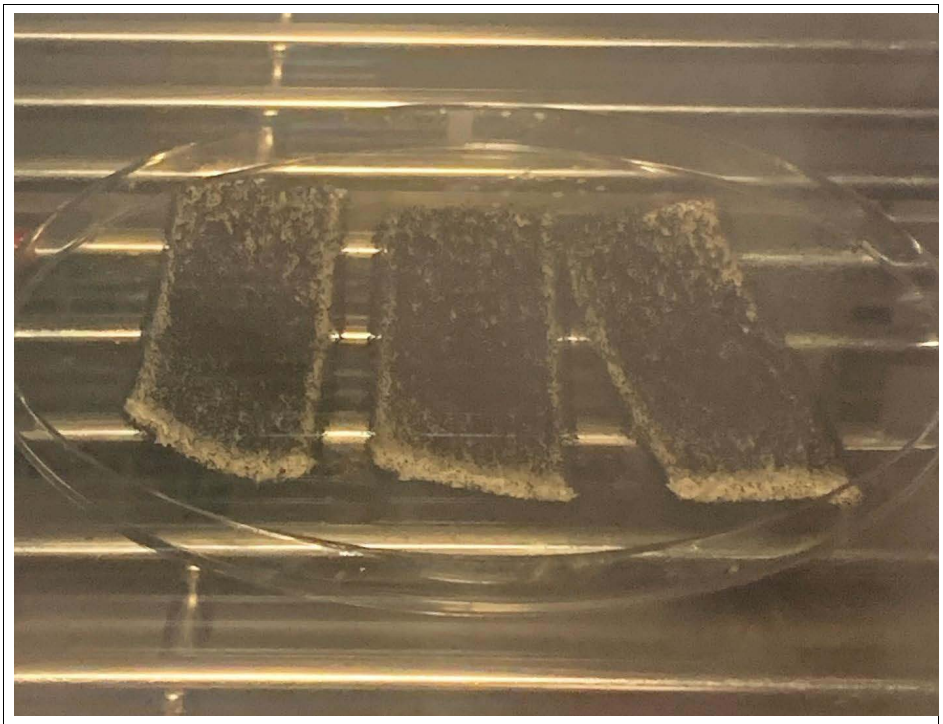

Overview of the Control Samples (Post 7 Days)
The white control cloths were inoculated with fungal spores and allowed to incubate for 7 days adjacent to the submitted samples. Growth is visible without microscopy.

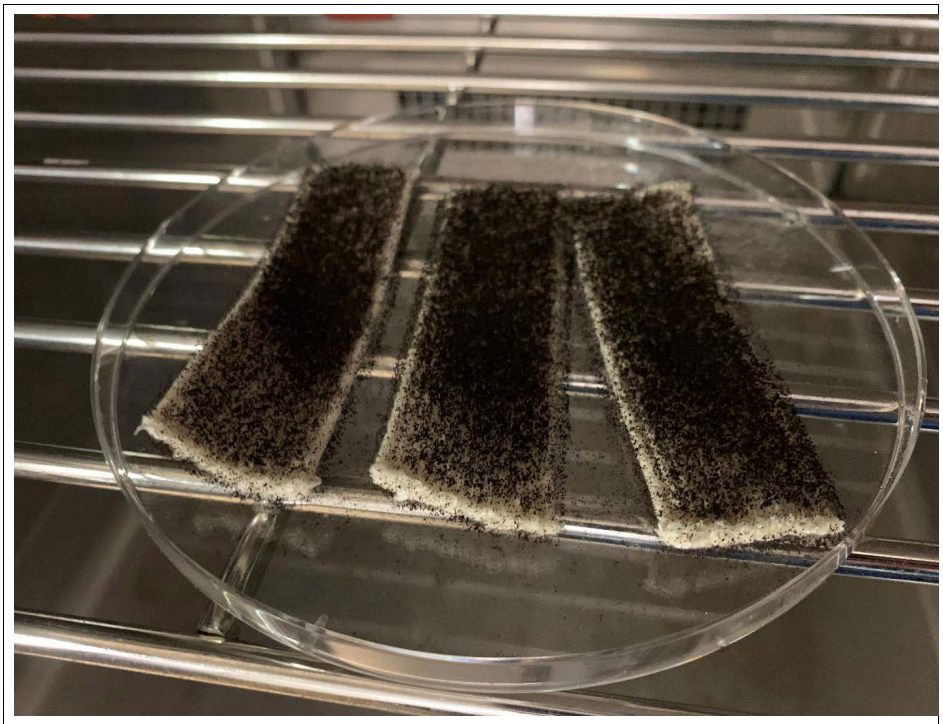

Overview of the Control Samples (Post 28 Days)
The white control cloths were inoculated with fungal spores and allowed to incubate for 28 days adjacent to the submitted samples. Growth is visible without microscopy.

EQUIPMENT LIST

Asset Number	Manufacturer	Description	M/N	S/N	Last Calibration	Cal Due
WC051500	Market Forge	Autoclave	STM-E	41333	07/05/2022	07/31/2023
WC051523	Olympus	Stereomicroscope with Pax-It2 Version 1.7.3.0 (installed 6/4/2021)	SZX16	0L40214	12/13/2021	06/30/2023
WC051524	Microstar	BINOCULAR MICROSCOPE	AO	BE318023	NCR	NCR
WC051625	Espec	ENVIRONMENTAL CHAMBER	ESX-3CA	112232	07/05/2022	07/31/2023
WC051626	Yokogawa	RECORDER	FX106-4-2	S5N308885	07/05/2022	07/31/2023
WC051668	Thermo Scientific	MULTI-PURPOSE ROTATOR (SHAKER)	2345	1666090807904	NCR	NCR
WC051692	Gallenkamp	incubator	ipr150.xx1.1/sg93 /02/304		NCR	NCR
WC051740	Tuttnauer Brinkman	AUTOCLAVE/STEAM STERILIZER	3870EA	14081496	09/13/2022	09/30/2023
WC051863	Sartorius	Digital Balance	ENTRIS5201-1S	0035807306	03/22/2023	03/31/2024
WC051901	Control Company	Traceable Digital Bottle	06-664-257	181757154	05/16/2022	02/29/2024
WC051902	Control Company	Traceable Digital Bottle	06-664-257	181721460	05/16/2022	02/29/2024
WC051928	Hausser Scientific	Counting Chamber	1492	522956	NCR	NCR
WC051957	Esco	BioHood	LA2-4A2-E	2019-141243	04/10/2023	04/30/2024
WC051961	VWR International	Refrigerator/Freezer Thermometer	EU 620-0919	D182548	05/18/2023	05/18/2024
WC051962	VWR International	Refrigerator/Freezer Thermometer	EU 620-0919	D182543	05/18/2023	05/18/2024
WC052072	DeVilbiss	Glass Atomizer w/Metal Top	163-RD		NCR	NCR
WC052090	Benchmark Scientific	Hotplate/Stirrer	H4000-HS	202104081602	NCR	NCR
WC059338	General Tools	Digital Anemometer	DCFM 8906	9962457	09/15/2022	11/30/2023
WC059408	Fisherbrand Ertco	Glass Thermometer /Incubator Bottle	I-030-1SR	18127	10/13/2021	08/31/2023
WC059409	Fisherbrand Ertco	Glass Thermometer/ Incubator Bottle	i-030-1SR	12880	10/13/2021	08/31/2023
WC059411	Fisherbrand Ertco	Glass Thermometer/ Incubator Bottle	1007-3	19721	10/13/2021	08/31/2023

TEST METHOD

FUNGUS RESISTANCE

The cultures of each microorganism were maintained separately on potato dextrose agar medium, except for the *Chaetomium globosum* which was inoculated on strips of filter paper on the surface of mineral salts agar.

A spore suspension was prepared two weeks after inoculation and incubation of the microorganisms by pouring into one subculture of each fungus, a 10-ml portion of a sterile solution containing 0.05 g per liter of a non-toxic wetting agent such as sodium dioctyl sulfosuccinate. Using a sterile inoculating loop the surface growth of each culture was gently scraped to remove it from the agar. The spore charge was poured into a sterile 125 ml glass-stopped Erlenmeyer flask containing 45 ml of sterile water and 10 - 15 solid glass beads (5 mm in diameter). The flask was vigorously shaken in order to liberate the spores from the fruiting bodies and to break up the spore clumps. The dispersed fungal spore suspension was filtered through a 6 mm layer of glass wool contained in a glass funnel, into a sterile test tube.

This process removed large mycelial fragments and clumps of agar, which could interfere with the spraying process.

The test tubes containing the filtered spore suspension were placed in a centrifuge for 20 minutes. The supernatant liquid was discarded. The residue was resuspended with sterile water and again placed in the centrifuge. The spores were washed in this manner three times. The final washed residue was resuspended with sterile mineral salts solution in such a manner that the resultant spore suspension contained 1,000,000 $\pm$ 200,000 spores per ml as determined with a counting chamber.

This operation was repeated for each organism used in the test and equal volumes of the resultant spore suspension was blended to obtain the final mixed spore suspension. The spore suspension was prepared fresh or previously held at 6° $\pm$ 4°C for not more than 14 days.

With each test specimen group, three pieces of sterilized filter paper, one inch square, were placed on hardened mineral salts agar in separate Petri dishes. They were inoculated with the spore suspension by spraying from a sterilized atomizer until initiation of droplet coalescence. In addition to the viability of inoculum control, a known susceptible substrate (a sterile cotton strip) was inoculated along with the test item to ensure that proper conditions were present in the incubation chamber to promote fungus growth. The control strip was dipped in a solution containing 10% glycerol, 0.1% potassium dihydrogen orthophosphate, 0.1% ammonium nitrate, 0.025% magnesium sulfate, and 0.05% yeast extract (pH 5.3). The excess liquid was removed prior to inoculation.

FUNGUS RESISTANCE (CONTINUED)

The test samples and controls were inoculated with a spore suspension consisting of the following organisms:

- *Aspergillus brasiliensis (formerly known as Aspergillus niger)*
- *Aspergillus flavus*
- *Trichoderma virens*
- *Chaetomium globosum*
- *Talaromyces pinophilus (formerly known as Penicillium funiculosum)*

The test specimen(s) and controls were placed in the test chamber and held at 30°C with 97% ± 2% relative humidity for four (4) hours prior to inoculation. After inoculation, the chamber was held at the same constant temperature and humidity conditions for the test duration.

The control specimens were examined after seven (7) days to insure appropriate fungal growth (90% of the surface area should be covered). The cotton strips showed satisfactory growth, and the test was continued for the appropriate duration time. After the 28-day exposure, the test specimen(s) and controls were immediately examined for fungus growth and assigned a growth rating based on the table below.

MIL-STD-810 Table 508.8-II: Evaluation Scheme for Visible Effects		
Growth Amount	**Rating**	**Observation**
None	0	Substrate is devoid of microbial growth.
Trace	1	Scattered, sparse, or very restricted microbial growth.
Light	2	Intermittent infestations or loosely spread microbial colonies on substrate surface. Includes continuous filamentous growth extending over the entire surface, but underlying surfaces are still visible.
Medium	3	Substantial amount of microbial growth. Substrate may exhibit visible structural change.
Heavy	4	Massive microbial growth.

After the visual inspection, the samples were decontaminated.

DATASHEETS

Form 36
Revision 0
Page 1 of 1

APPLICABLE TEST METHODS: Mil-STD-810H

EQUIPMENT USED: See Below

FUNGUS RESISTANCE PREPARATION

MINERAL SALTS SOLUTION PREPARATION: Date Prepared: 4/26/2023 Prepared By: DH

Compounds Used: Date Expires: 7/25/2023

Potassium dihydrogen orthophosphate ID:	13820	Sodium chloride ID:	13587
Potassium monohydrogen orthophosphate ID:	13356	Ferrous sulfate heptahydrate ID:	13838
Magnesium sulfate heptahydrate ID:	13367	Zinc sulfate heptahydrate ID:	13378
Ammonium Nitrate ID:	13353	Manganous sulfate monohydrate ID:	13357

Sterilization: Start Date / Time: 4/26/23 1:00 PM Duration (mins): 30 (20 minimum)

pH: 6.0 (6.0-6.5) Adjusted pH, if needed: N/A

Sodium hydroxide ID: N/A

MINERAL SALTS AGAR PREPARATION: Date Plated: 3/6/2023 Prepared By: DH

Compounds Used: Date Expires: 9/2/2023

Potassium dihydrogen orthophosphate ID:	13820	Sodium chloride ID:	13587
Potassium monohydrogen orthophosphate ID:	13356	Ferrous sulfate heptahydrate ID:	13838
Magnesium sulfate heptahydrate ID:	13367	Zinc sulfate heptahydrate ID:	13378
Ammonium Nitrate ID:	13353	Manganous sulfate monohydrate ID:	13357
Agar ID:	13713		

Sterilization: Start Date / Time: 3/6/2023 12:45pm Duration (mins): 30 (minimum, 20)

pH: 6.0 (6.0-6.5) Adjusted pH, if needed: N/A

Sodium hydroxide ID: N/A

INDIVIDUAL SPORE SUSPENSIONS PREPARATION: Prepared By: DH/KH

A. brasiliensis (ATCC #9642) ID:	12830	*A. pullulans* (ATCC #15233) ID:	13234	*A. versicolor* (ATCC #11730) ID:	13231
C. globosum (ATCC #6205) ID:	13227	*T. virens* (ATCC #9645) ID:	13229	*A. flavus* (ATCC #9643) ID:	13228
P. funiculosum (ATCC #11797) ID:	13233				

Wetting agent: Agent used: Lauryl Sulfate ID: 13886

Date Prepared:	Colony Count (within 1 mm^2)		Calculated Count		Date Expires:
5/26/2023	*A. brasiliensis* :	18	900,000	(1,000,000 ± 200,000)	6/9/2023
5/26/2023	*C. globosum* :	20	1,000,000	(1,000,000 ± 200,000)	6/9/2023
5/26/2023	*P. funiculosum* :	21	1,050,000	(1,000,000 ± 200,000)	6/9/2023
5/26/2023	*A. pullulans* :	N/A	#VALUE!	(1,000,000 ± 200,000)	6/9/2023
5/26/2023	*T. virens*:	24	1,200,000	(1,000,000 ± 200,000)	6/9/2023
5/26/2023	*A. veriscolor*:	18	900,000	(1,000,000 ± 200,000)	6/9/2023
5/26/2023	*A. flavus* :	19	950,000	(1,000,000 ± 200,000)	6/9/2023

*Previously known as a different species.

NOTES:

Equipment Used:
WC051523, WC051524, WC051628, WC051668, WC051692, WC051740, WC051863, WC051901, WC051902, WC051928, WC051957, WC051961, WC051962, WC052090, WC059253, WC059338, WC059408, WC059409, WC059411, WC061951, WC051500, WC051625

Form 39
Revision 0
Page 1 of 1

CUSTOMER NAME: Montana State University
PROJECT #: 170930
EQUIPMENT USED: See Form 36
REVISION:

TEST INFORMATION - Fungus Resistance, MIL-STD-810, method 508

SAMPLE IDENTIFICATION:

1. Dyneema HB-210
2. Dyneema HB-212 (Cloth)
3. Dyneema HB-212
4. Spectra 5241

MIXED SPORE SUSPENSION PREPARATION: Date Prepared: 6/1/2023 Prepared By: DH

Spores Used: Date Expires: 6/15/2023

**A. brasiliensis* ID:	12830	*A. versicolor* ID:	13231
C. globosum ID:	13227	*A. flavus* ID:	13228
**P. funiculosum* ID:	13233		

*Previously known as a different species. Please see Test Method section for former nomenclature descriptions.

PRECONDITIONING INFORMATION:

Start Date/Time: 6/1/2023 10:30am
End Date/Time: 6/1/2023 14:30pm
Duration (Hours): 4.00 (4 minimum)

Chamber Conditions:

Temperature: 30.0 (30±2°C) Humidity: 95 (90-99%)
Airflow across wet bulb sensor: 1122 (≥900 ft/min) Sample airflow: 217 (98-335 ft/min)

EXPOSURE INFORMATION:

Start Date: 6/1/2023
End Date: 6/8/2023
Duration (Days): 7 (28)

Chamber Conditions:

Temperature: 30.0 (30±2°C) Humidity: 95 (90-99%)
Airflow across wet bulb sensor: 1072 (≥900 ft/min) Sample airflow: 198 (98-335 ft/min)

CONTROL INFORMATION:

#1 - Viability of Spore Suspension: Date Prepared: 6/1/2023 Prepared By: DH
#2 - Control Strips: Date Prepared: 6/1/2023 Prepared By: DH
#3 Individual Spore Viability: Date Prepared: 5/26/2023 Prepared By: DH

Washing Solution Compound:

Glycerol ID:	13919	Magnesium sulfate ID:	13367
Potassium dihydrogen orthophosphate ID:	13820	Yeast extract ID:	13306
Ammonium nitrate ID:	13353	Sodium lauryl sulfate ID:	13886

#1 - Day 7 Evaluation Rating: 4 (0-4) Performed By: DH OK to Proceed? (Y/N): Y (satisfactory fungus growth must be visible)

#2 - Day 7 Evaluation Rating: 4 (0-4) Performed By: DH OK to Proceed? (Y/N): Y (satisfactory fungus growth must be visible)

#3 - Individual Spore Viability: ACC (ACC / REJ) (7-10 days post inoculation) Performed By: DH/KH OK to Proceed? (Y/N): Y (satisfactory fungus growth must be visible)

VISUAL EXAMINATION RESULTS: Ratings: 0 - None, 1 - Trace, 2 - Light, 3 - Medium, 4- Heavy

Sample ID	Date	Initials	Rating (0-4)	Comments / Description
Dyneema HB-210	6/8/2023	KH	0	No apparent fungal growth observed under microscopy after 7 days. "Minimal" debris noted.
Dyneema HB-212 (Cloth)	6/8/2023	KH	0	No apparent fungal growth observed under microscopy after 7 days. "Moderate" debris noted.
Dyneema HB-212	6/8/2023	KH	0	No apparent fungal growth observed under microscopy after 7 days. "Heavy" debris noted.
Spectra 5241	6/8/2023	KH	1	Sporadic fruiting body growth along edge and slightly inward after 7 days. "Moderate" debris noted.

Date/Time Out of Chamber: 6/8/23 2:45 PM Date/Time of Inspection: 6/8/23 3:01 PM
(Perform within 1 hr of "Date / Time Out of Chamber", if not, consult method)

CHAMBER DECONTAMINATION:

Before Testing: Date Performed: 5/1/2023 Performed By: KH
After Testing: Date Performed: TBD Performed By: TBD

NOTES:

The labeled portions and frayed cut edges were not assessed for fungal growth.

Form 39
Revision 0
Page 1 of 1

CUSTOMER NAME: Montana State University
PROJECT #: 170930
EQUIPMENT USED: See Form 36
REVISION:

TEST INFORMATION - Fungus Resistance, MIL-STD-810, method 508

SAMPLE IDENTIFICATION:

1. Dyneema HB-210
2. Dyneema HB-212 (Cloth)
3. Dyneema HB-212
4. Spectra 5241

MIXED SPORE SUSPENSION PREPARATION: Date Prepared: 6/1/2023 Prepared By: DH

Spores Used: Date Expires: 6/15/2023

**A. brasiliensis ID:*	12830	*A. versicolor* ID:	13231
C. globosum ID:	13227	*A. flavus* ID:	13228
**P. funiculosum* ID:	13233		

*Previously known as a different species. Please see Test Method section for former nomenclature descriptions.

PRECONDITIONING INFORMATION:

Start Date/Time: 6/1/2023 10:30am
End Date/Time: 6/1/2023 14:30pm
Duration (Hours): 4.00 (4 minimum)

Chamber Conditions:

Temperature: 30.0 (30±2°C) Humidity: 95 (90-99%)
Airflow across wet bulb sensor: 1122 (≥900 ft/min) Sample airflow: 217 (98-335 ft/min)

EXPOSURE INFORMATION:

Start Date: 6/1/2023
End Date: 6/29/2023
Duration (Days): 28 (28)

Chamber Conditions:

Temperature: 30.0 (30±2°C) Humidity: 95 (90-99%)
Airflow across wet bulb sensor: 1072 (≥900 ft/min) Sample airflow: 198 (98-335 ft/min)

CONTROL INFORMATION:

#1 - Viability of Spore Suspension: Date Prepared: 6/1/2023 Prepared By: DH
#2 - Control Strips: Date Prepared: 6/1/2023 Prepared By: DH
#3 Individual Spore Viability: Date Prepared: 5/26/2023 Prepared By: DH/KH

Washing Solution Compound:

Glycerol ID: 13919 Magnesium sulfate ID: 13367
Potassium dihydrogen orthophosphate ID: 13820 Yeast extract ID: 13306
Ammonium nitrate ID: 13353 Sodium lauryl sulfate ID: 13886

#1 - Day 7 Evaluation Rating: 4 (0-4) Performed By: DH OK to Proceed? (Y/N): Y (satisfactory fungus growth must be visible)
#2 - Day 7 Evaluation Rating: 4 (0-4) Performed By: DH OK to Proceed? (Y/N): Y (satisfactory fungus growth must be visible)
#3 - Individual Spore Viability: ACC (ACC / REJ) (7-10 days post inoculation) Performed By: DH/KH OK to Proceed? (Y/N): Y (satisfactory fungus growth must be visible)

VISUAL EXAMINATION RESULTS: Ratings: 0 - None, 1 - Trace, 2 - Light, 3 - Medium, 4- Heavy

Sample ID	Date	Initials	Rating (0-4)	Comments / Description
Dyneema HB-210	6/29/2023	KH/DH	0	No apparent fungal growth observed under microscopy after 28 days. "Moderate" debris noted.
Dyneema HB-212 (Cloth)	6/29/2023	KH/DH	0	No apparent fungal growth observed under microscopy after 28 days. "Heavy" debris noted.
Dyneema HB-212	6/29/2023	KH/DH	0*	*Localized active growth observed on frayed cut edges after 28 days. These areas were omitted from the rating due to likely contamination during cutting. "Heavy" debris noted.
Spectra 5241	6/29/2023	KH	1	Sporadic fruiting body growth along edge and inward after 28 days. Growth appears to have spread more from 7 day evaluation. "Moderate" debris noted.

Date/Time Out of Chamber: 6/29/23 1:00 PM Date/Time of Inspection: 6/29/23 1:10 PM
(Perform within 1 hr of "Date / Time Out of Chamber", if not, consult method)

CHAMBER DECONTAMINATION:

Before Testing: Date Performed: 5/1/2023 Performed By: KH
After Testing: Date Performed: TBD Performed By: TBD

NOTES:

*The labeled portions and frayed cut edges were omitted from the fungus growth rating.

REVISION HISTORY

Rev.	Revision Date	Description
0	11-Jul-2023	Initial release

END OF REPORT